distribution of the network fragments at a given extent of decomposition. The extent of decomposition is specified by the probability, p, that the possible attachments are made. For example, for 20% of broken bridges (p = 0.8), a linear chain is totally fragmented, while a "fish net" will have some holes but is almost totally connected. In describing the network, a crosslink is defined to occur at a branch point where there are more than two attachments on a ring cluster. The coordination number is thus related to the crosslink density. With no possible crosslinks, the coordination number is two. With increasing crosslink density the coordination number increases.

The second important property of the network is the fraction of possible attachments, p, which are actually present. During thermal decomposition, this fraction is determined by the rates of bridge breaking. The factors which control how many of the weak links can break are the rate constant and the amount of hydrogen that can be donated from the coal to stabilize the free radicals which form when the links break.

A competitive process with the bond breaking is the retrogressive process of crosslinking. Crosslinking reactions appear to be related to the evolution of certain gases. Specifically, for low rank coals, crosslinking at low temperature (prior to bridge breaking) seems to be related to the evolution of carbon dioxide. For coals of all rank, a higher temperature crosslinking event (following bridge breaking) seems to be related to the evolution of methane. At high temperatures, the evolution of hydrogen is also related to crosslinking.

The final concept is that the tar evolution is controlled by mass transport. Bridge breaking and crosslinking produce a set of fragments with a molecular weight distribution. The lightest fragments can leave the coal melt by evaporation into the light gas species. The heavier fragments remain, forming the metaplast which controls the coal's fluidity.

It is described fully in Solomon et al. (1988a) and is described in the abstract as follows.

## Abstract

A general model for coal devolatilization, which combines a functional group model for gas evolution and a statistical model for tar formation, has been presented. The tar formation model includes depolymerization, crosslinking, external transport, and internal transport. The crosslinking is related to the evolutions of $CO_2$ and $CH_4$, with one crosslink formed per molecule evolved. The model predictions compare favorably with a variety of data for the devolatilization of Pittsburgh Seam coal and North Dakota (Beulah) lignite, including volatile yields, extract yeilds, crosslink densities, and tar molecular weight distributions. The variations with pressure, devolatilization temperature, rank, and heating rate were accurately predicted. Comparison of the model with several sets of data employing alterative assumptions on transport suggests that assuming that the particle is well mixed (i.e., the surface concentration of tar molecules is the same as the bulk) overpredicts the transport rate. For 50 $\mu$m particles, assuming that the internal transport limitation dominates (i.e., neglecting the external transport) provides a good fit to the data. The rank dependence of tar formation, extract yields, crosslinking, and viscosity appears to be explained by the rank dependence of $CO_2$ yields and its associated crosslinking. High $CO_2$ yields in low rank coals produce rapid crosslinking at low temperatures and hence thermosetting behavior, low tar yields, low extract yields, loss of solvent swelling properties, and high viscosities. The relative importance of crosslinking compared to bond breaking is, however, sensitive to heating rate. and this effect is predicted by the model. Areas for improving the model include: 1) refinement of the internal and external transport assumptions; 2) accounting for hydroaromatic structures and bridge structures besides ethylene; and 3) including polymethylene "guest" molecules.

Recently, the model characterization methods and kinetics for the Argonne premium coal collection were published (Solomon et al. 1993). The abstract for this paper is as follows.

## Abstract

The paper considers the development of a predictive macromolecular network decomposition model for coal conversion which is based on a variety of modern analytical techniques for coal characterization. Six concepts which are the foundation of the Functional Group, Depolymerization, Vaporization, Crosslinking (FG-DVC) model are considered: 1) The decomposition of functional group sources in the coal yields the light gas species in thermal decomposition. The amount and evolution kinetics can be measured by TG-FTIR, the functional group changes by FT-IR and NMR. 2) The decomposition of a macromolecular network yields tar and metaplast. The amount and kinetics of the tar evolution can be measured by TG-FTIR and the molecular weight by FIMS. The kinetics of metaplast formation and destruction can be determined by solvent extraction, by Geissler plastometer measurements and by proton magnetic resonance thermal analysis (PMRTA). 3) The molecular weight distribution of the metaplast depends on the network coordination number (average number of attachments on aromatic ring clusters). The coordination number can be determined by solvent swelling and NMR. 4) The network decomposition is controlled by bridge breaking. The number of bridges broken is limited by the available donatable hydrogen. 5) The network solidification is controlled by crosslinking. The changing crosslink density can be measured by solvent swelling and NMR. Crosslinking appears to occur with evolution of both $CO_2$ (before bridge breaking) and $CH_4$ (after bridge breaking). Thus, low rank coals (which evolve much $CO_2$) crosslink before bridge breaking and are thus thermosetting. High volatile bituminous coals (which form little $CO_2$) undergo significant bridge breaking before crosslinking and become highly fluid. Weathering, which increases the $CO_2$ yield, causes increased crosslinking and lowers fluidity. 6) The evolution of tar is controlled by mass transport in which the tar molecules evaporate into the light gas or tar species and are carried out of the coal at rates proportional to their vapor pressure and the volume of light species. High pressures reduce the volume of light species and hence reduce the yield of heavy molecules with low vapor pressures. These changes can be studied with FIMS. The paper describes how the coal kinetic and composition parameters are obtained by TG-FTIR, solvent swelling, solvent extraction, and Geissler plastometer data. The model is compared to a variety of experimental data in which heating rate, temperature, and pressure are all varied. There is good agreement with theory for most of the data available from our laboratory and in the literature.

## Modeling of Mild Gasification

The FG-DVC coal devolatilization model was used to simulate mild gasification processes. The model was applied to data obtained from pyrolysis of Illinois #6 coal in the IGT mild gasification Process Research Unit (PRU) under essentially isothermal conditions. The PRU is a combination of a fluidized-bed and an entrained-bed reactor operated at temperatures from 1000 to 1400°F (550 to 750°C) and pressures close to atmospheric. Simulations were also done of pyrolysis data from a two-stage circulating bed reactor at Battelle obtained at temperatures from 1200 to 1650°F (650 to 900°C), ~ 1 atm pressure, also for Illinois #6 coal. In general, good agreement was obtained for the effect of temperature on the yields of char and gas. In the case of the tar, the model did not predict the fall-off in the tar yield at high temperature (> 1200°F) for the IGT data. However, the Battelle data did not show this fall-off in the tar yield and were in good agreement with the model predictions for tar, gas, and char.

**Introduction** - In recent years, there has been a growing interest in so-called "mild" gasification processes in which coal is converted using a pyrolysis process into a mixture of gaseous, liquid, and solid products. Work supported by the U.S. DoE includes projects at Battelle (Litt, et al., 1990) and IGT (Knight, et al., 1990). The Battelle project is based on a Multi-Solid Fluidized-Bed (MSFB) reactor system to produce high quality liquid and gaseous products. The MSFB reactor uses a circulating burden of fine particles to transport heat between an exothermic char combustion stage and an endothermic coal pyrolysis stage. Additional benefits of the circulation of these solid particles is the ability to use catalysts or sulfur capture agents. Preliminary tests of this concept have been done in small (2 inch diameter) circulating bed gasifier coupled to a 12 inch diameter bubbling bed combustor.

The IGT project incorporates an integration of fluidized-bed and entrained-bed reactors. The Process Research Unit (PRU) consists of an 8 inch ID x 8 foot long fluidized-bed reactor closely coupled to a 4 inch ID x 13 foot long entrained-bed reactor (Knight, et al. 1990). The feed rate of coal is approximately 100 lb/hr. This reactor is designed to be able to process caking coals of a wide range of particle sizes without oxidative pretreatment. In the full scale unit, the process heat would be provided by recycled hot char or high temperature flue gases. The heat requirements for the PRU were supplied by external electrical heaters.

**Model** - The results from these two pyrolysis reactors were modeled with the FG-DVC coal devolatilization model (Solomon, et al., 1988a). This model combines a functional group (FG) description of gas evolution (Solomon, 1981) with a depolymerization, vaporization, crosslinking (DVC) model of tar formation (Solomon, 1988b). The model is able to predict the correct trends for the variations of pyrolysis yields and tar molecular weight distributions with pressure, temperature, rank and heating rate (Solomon et al., 1988a). The model is general in that it can predict pyrolysis behavior for coals of wide range of ranks.

For the prediction of mild gasification processes, a version of the model was used which has the following features: 1) a secondary reaction model which includes the vapor phase cracking of tar to produce light gases using the same functional group approach that is used for coal; 2) a hydrocarbon cracking model which describes the gas phase pyrolysis of paraffinic and olefinic hydrocarbon species; 3) an optional equilibrium model which is used to treat reactions involving the major C, H, O containing species at high temperatures. The set of reactions used in the equilibrium model is as follows:

$$CO + H_2O = CO_2 + H_2 \qquad \text{(II.A.2-1)}$$

$$CH_4 + H_2O = CO + 3H_2 \qquad \text{(II.A.2-2)}$$

$$C + H_2O = CO + H_2 \qquad \text{(II.A.2-3)}$$

The equilibrium model is used by assuming that equilibrium of the char and the major gaseous species occurs at the highest temperature reached in a pyrolysis experiment, after which the products are "frozen". Of course, this is only an approximation which improves as the temperature and residence time increase. The coal char is assumed to have the properties of graphite and the gases are assumed to be ideal. Details of these submodels can be found in Serio et al. (1987).

An additional change to the model was the ability to have separate residence times for the gas and solid phases which is necessary to simulate fluidized-bed reactors.

**Results** - The model was applied to data obtained from pyrolysis of Illinois #6 coal in the IGT mild gasification Process Research Unit (PRU) under essentially isothermal conditions at temperatures from 1000 to 1400°F (550 to 750°C) and pressures close to atmospheric.

A comparison of the FG-DVC mild gasification model predictions and experimental data from the IGT PRU is shown in Fig. II.A.2-1. This is an adaption of a figure shown in Knight et al., 1990 which includes the plotting of data as solid circles where good material balances were obtained. The open circles are for runs where the material balances were suspect. The solid lines in Fig. II.A.2-1 are the results of a regression analysis on the "good" IGT data. Also shown in Fig. II.A.2-1 for comparison purposes are pilot-plant data from the COED (Scotti, et al., 1975) and Occidental flash pyrolysis processes (Che, et al., 1978) and laboratory data from CSIRO (Tyler, 1980) for similar coals. The FG-DVC model predictions are the dashed lines in Fig. II.A.2-1. The model does a reasonable job in predicting the variation in the yields of char, gas, and water with temperature. It does not, however, predict the maximum observed in the tar yield with pyrolysis temperature (~ 1200°F) for the IGT data.

Simulations were also done of pyrolysis data from the 2 inch circulating-bed reactor at Battelle obtained at temperatures from 1200 to 1650°F (650 to 900°C), ~ 1 atm pressure, also for Illinois #6 coal. The experimental results for the yields of tar and gas are shown in Fig. II.A.2-2 (open circles). The predictions for the standard FG-DVC mild gasification model are shown as closed circles connected by lines in Fig. II.A.2-2. The predictions of FG-DVC model with the added assumption that the gaseous pyrolysis products are in equilibrium with the char is shown in Fig. II.A.2-2 as the solid lines connected by solid squares. The equilibrium model does not include the tar species. The predictions of the standard

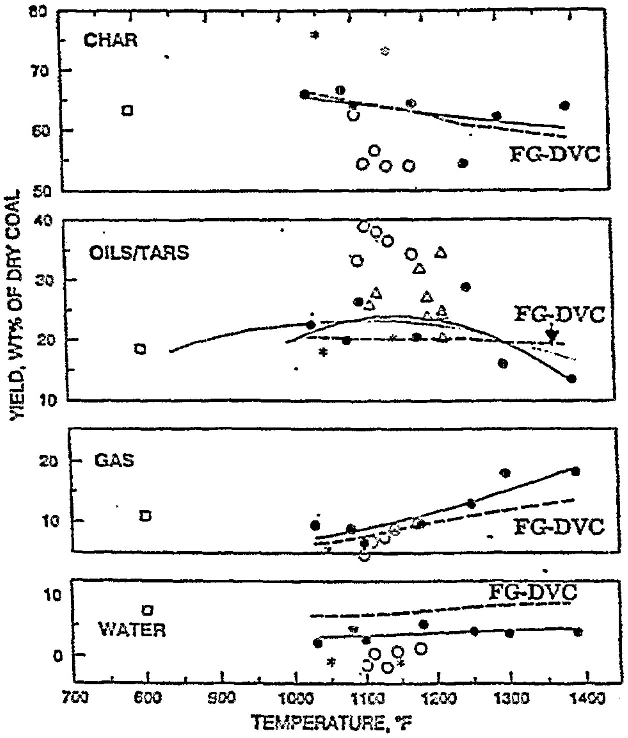

**Figure II.A.2-1.** Comparison of FG-DVC Mild Gasification Model Predictions (—) and Experimental Data from IGT for Overall Product Yields ● IGT PRU , Illinois Coal; ○ IGT PRU Data, Illinois coal (not included in regression curve); * IGT PRU Data, West Virginia Coal; △ Occidental Flash Pyrolysis; ▪ COED Second Stage; (...) CSIRO Fluidized Bed, LiddellB Coal.

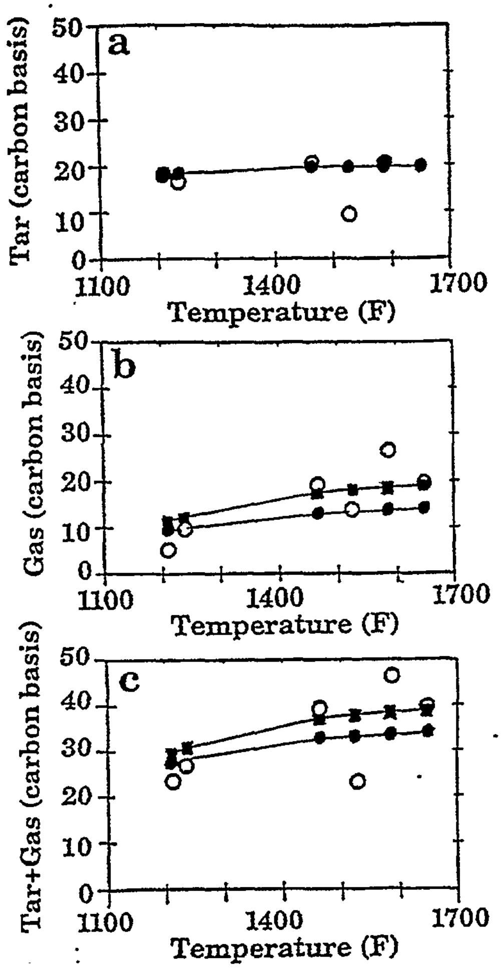

Figure II.A.2-2. Comparison of Standard ( ● - ● ) and Equilibrium (■ - ■ ) FG-DVC Mild Gasification Model Predictions and Experimental Data from Battelle ( ○ ).

model are in good agreement with the tar data, except for one data point. It is interesting that the tar yield data from the Battelle reactor do not show the maximum in tar yield despite the relatively high temperatures used. This difference is probably due to the fact that the mean gas phase residence time is relatively small for the Battelle unit (see below).

The data for the total gas yields are more scattered. It appears that the assumption of equilibrium of the volatile products gives a better prediction. However, it is unlikely that the system would be close to equilibrium under conditions where the reactor severity is so low that tar cracking does not occur.

A parameter in the model was the gas-phase residence time. A value of 2 sec was used for the IGT reactor; while a value of 0.8 sec was used for the Battelle reactor. These values were based on estimates of the gas hold up in the system provided by the respective organizations. The average solids residence time was in the range of 20 to 30 minutes for the IGT system and ~ 1 sec for the Battelle reactor.

In the case of individual gases, good agreement was obtained for $H_2$, $CH_4$, $C_2$'s and CO data from the IGT PRU (see Fig. II.A.2-3). The amount of $CO_2$ was somewhat under predicted (see Fig. II.A.2-3b). Better agreement was obtained using a partial equilibrium model for the gas phase. Data on individual gas species yields were not available from the Battelle study.

**Conclusions** - A coal devolatilization model has been adopted for simulation of mild gasification process. Good agreement has been obtained for the prediction of char and gas yields from mild gasification processes. The model does not yet predict the maximum observed in the tar yield for the IGT data. This may require an improved description of tar cracking and/or the residence time of the tar species.

## II.A.3. Coal and Char Fluidity

The FG-DVC model predicts the amount of detached molecules or liquids (tar, extracts, and liquids) produced in pyrolysis. This quantity can be directly related to the coal's fluidity or viscosity. The fluidity model is presented in Solomon, et al. 1992. The abstract for this publication is as follows.

### Abstract

We have developed a phenomenological model for coal fluidity based on a macromolecular network model for the decomposition and condensation of the network under the influence of bond breaking and crosslinking reactions. The macromolecular network model is the previously published FG-DVC model of coal pyrolysis. It employs a network consisting of aromatic ring clusters linked by bridges. The bond scissions are described by a single first order reaction with a distribution of activation energies. Crosslinking is related to $CO_2$ and $CH_4$ formation which are described in multiple first order reactions with distributions of activation energies. The fluidity is described by an empirical equation which depends on the relative amounts of the liquid (molecules detached from the network), and solid (the remaining network) and on the fluidity of the liquid component. The FG-DVC model predicts the yield of liquids. The fluidity of the liquid component is described by a second phenomonological equation which depends only on the temperature. The advantage of this model is that it is based on a previously demonstrated methodology which allows the incorporation of rank dependent kinetics, crosslinking, weathering, and extraction phenomena into the fluidity predictions. Excellent agreement has been obtained between the model predictions and low temperature fluidity measurements of Oxley and Pitt, van Krevelen, and Gieseler plastometer measurements for the Argonne premium coal samples. The trends for changes in the fluidity with weathering or extraction are predicted as well. Good agreement has been obtained at high temperatures between the model predictions and measurements of Fong for the onset of the fluidity. The loss of fluidity, however, is predicted to occur sooner than is indicated by the data and the maximum value of fluidity is over predicted. The data cover over five orders of magnitude in fluidity, and eight coals with carbon concentration between 80 and 90%. This agreement is obtained using coal independent equations for the dependence of the fluidity on the liquid fraction and the liquid fluidity. The coal dependent variables are the kinetic rates for bond breaking and crosslinking and the extent of crosslinking as determined from

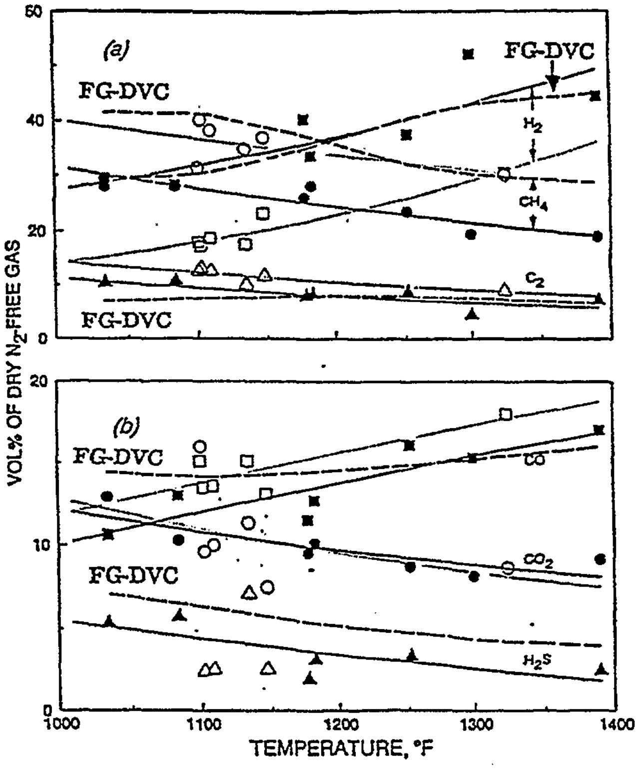

Figure II.A.2-3. Comparison of FG-DVC Mild Gasification Model Predictions (----) and Experimental Data from IGT for Individual Gas Product Yields. (......) Regression Model for Open Symbols: Steam/Coal Ratio = 0.0 to 0.5 ( — ) Regression Model for Filled Symbols: Steam/Coal Ratio = 0.7 to 1.4.

laboratory pyrolysis measurements using a TG-FTIR (Thermogravimetric analyzer with Fourier Transform Infrared analysis of evolved products). There are only two adjustable parameters of the model.

## II.A.4. Char Swelling Model

### Introduction

Under certain conditions, coals which become fluid when heated also swell, due to the internal pressure of trapped, evolved gases. Experimental observations of the swelling in the absence of oxygen are made both on single particles which have swollen in essential isolation, and on agglomerates, as in a measurement of the free-swelling index. Although the same basic phenomena are involved in both cases, only the swelling of individual particles of pulverized coal (radius $< 100\ \mu m$, say) has been modeled to date. These particles are treated as being isothermal.

When microscopic observations of swollen coal particles are made it becomes apparent that the particles do not behave in an identical fashion. At average heating rates, between $10^2$ and $10^4$ K $s^{-1}$, the swollen particles of a typical swelling coal, Pittsburgh No. 8, can be categorized into one of three types: a small fraction (~ 10%) which shows virtually no sign of fluidity, and hence no swelling; the majority (~ 80%) which experience swelling of about the same magnitude; and another small fraction (~ 10%) which exhibits behavior that can be associated with a much higher fluidity (lower viscosity) than the majority. We have associated the three behaviors with the three main maceral types of the coal; inertinite, vitrinite, and exinite, respectively. In the model the properties only of average particles are described, and this must be recognized when comparing predictions with microscopic observations. It is for average particles that the FG-DVC model is applicable.

The range of "swelling" behaviors encompassed by our model includes the swelling which is observed for moderate heating, but also the behaviors at the extremes of heating rate. At very low heating rates ($\leq 10$ K $s^{-1}$) there is virtually no swelling: gas production by pyrolysis is only marginally greater than out-diffusion of gas. At extremely high rates ($\geq 5 \times 10^4$ K $s^{-1}$), the liquid walls surrounding the gas-filled internal voids rupture, allowing the gas to escape. Minimal swelling is observed in this case.

Because the modeling is driven by observation, the various swelling behaviors will be introduced by scanning electron microphotographs, all of which were recorded in METC supported research. In Figs. II.A.4-1a and II.A.4-1b (close-up) we show single-cell cenospheres. What we term multi-cell or multi-bubble swollen particles are shown in Figs. II.A.4-2a and II.A.4-2b (close-up). Typically each particle appears to have between 10 and 20 internal cells. We believe that the rope-like structures which appears on the inside of the wall is the residue of internal walls between adjacent bubbles of the swollen particle. Popped or ruptured particles are shown in Figs. II.A.4-3a, II.A.4-3b and in II.A.4-3c, where the internal surface of a cracked particle is shown. In contrast to the cases of Figs. II.A.4-1 and II.A.4-2, these particles have not undergone significant swelling. Finally, in Figs. II.A.4-4a and II.A.4-4b, two "no-model" particles are shown. Like the single and multi-cell particles, these are thin-walled structures, but are characterized by a myriad of internal cells. These no-model particles exhibit the greatest swelling. Unlike the case for the other particles, however, we have not made sufficient observations to assert that the no-model behavior occurs for the vitrinite component of the coal. We do not quantitatively predict the swelling of the no-model particles. It is believed that the above behaviors represent the swelling types, although variants of these are observed.

### Qualitative Discussion

The different swelling (or non-swelling) behaviors can be accounted for qualitatively. To begin with a discussion based on dimensional analysis is presented.

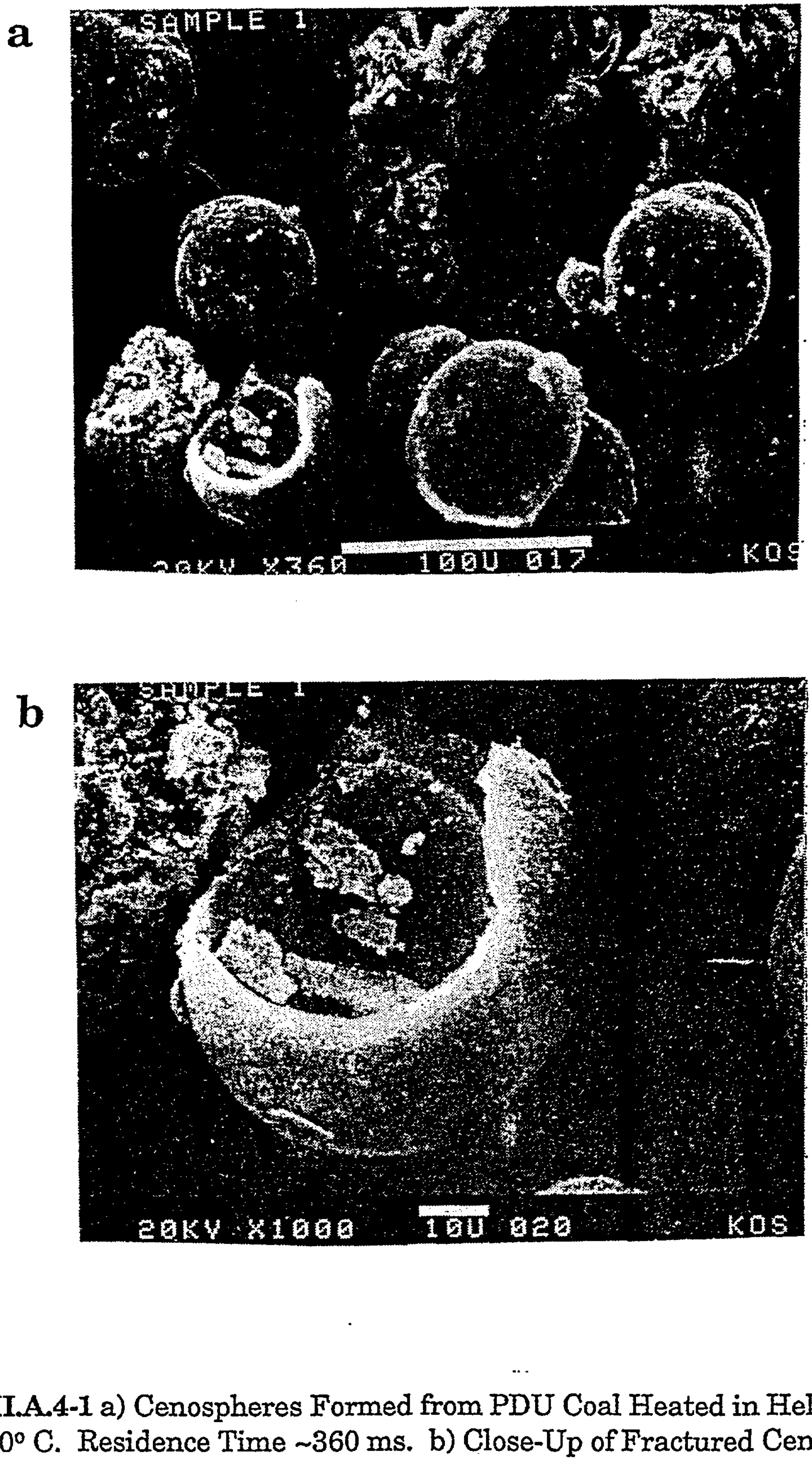

**Figure II.A.4-1** a) Cenospheres Formed from PDU Coal Heated in Helium at ~5x10$^3$ K/s to 800° C. Residence Time ~360 ms. b) Close-Up of Fractured Cenosphere.

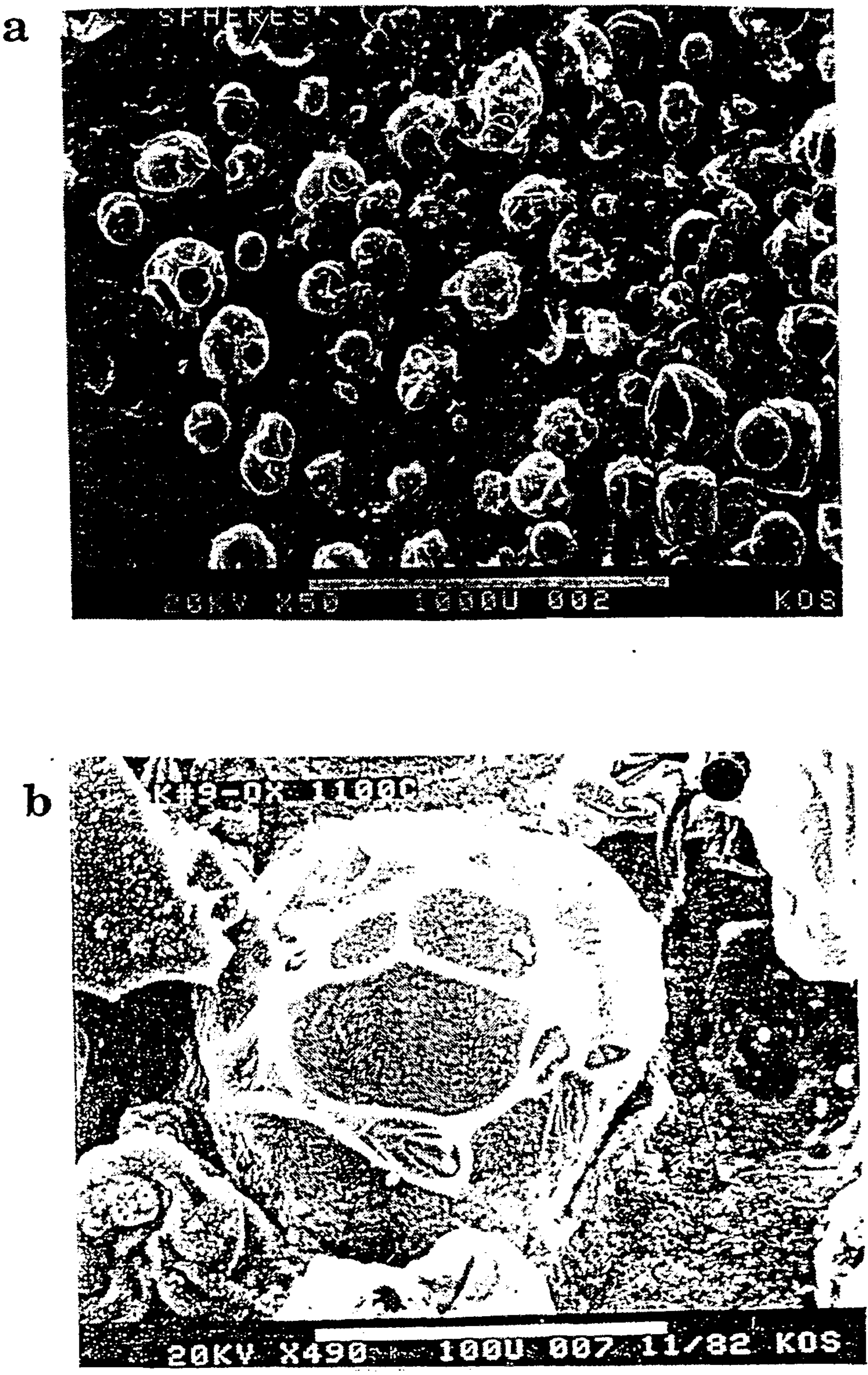

**Figure II.A..4-2** a) Multi-Cell Swollen Particles Formed When Kentucky #9 Butuminous Coal was Heated in 99% Nitrogen/1% Oxygen, at 1100° C. b) Close-Up of One of These Particles.

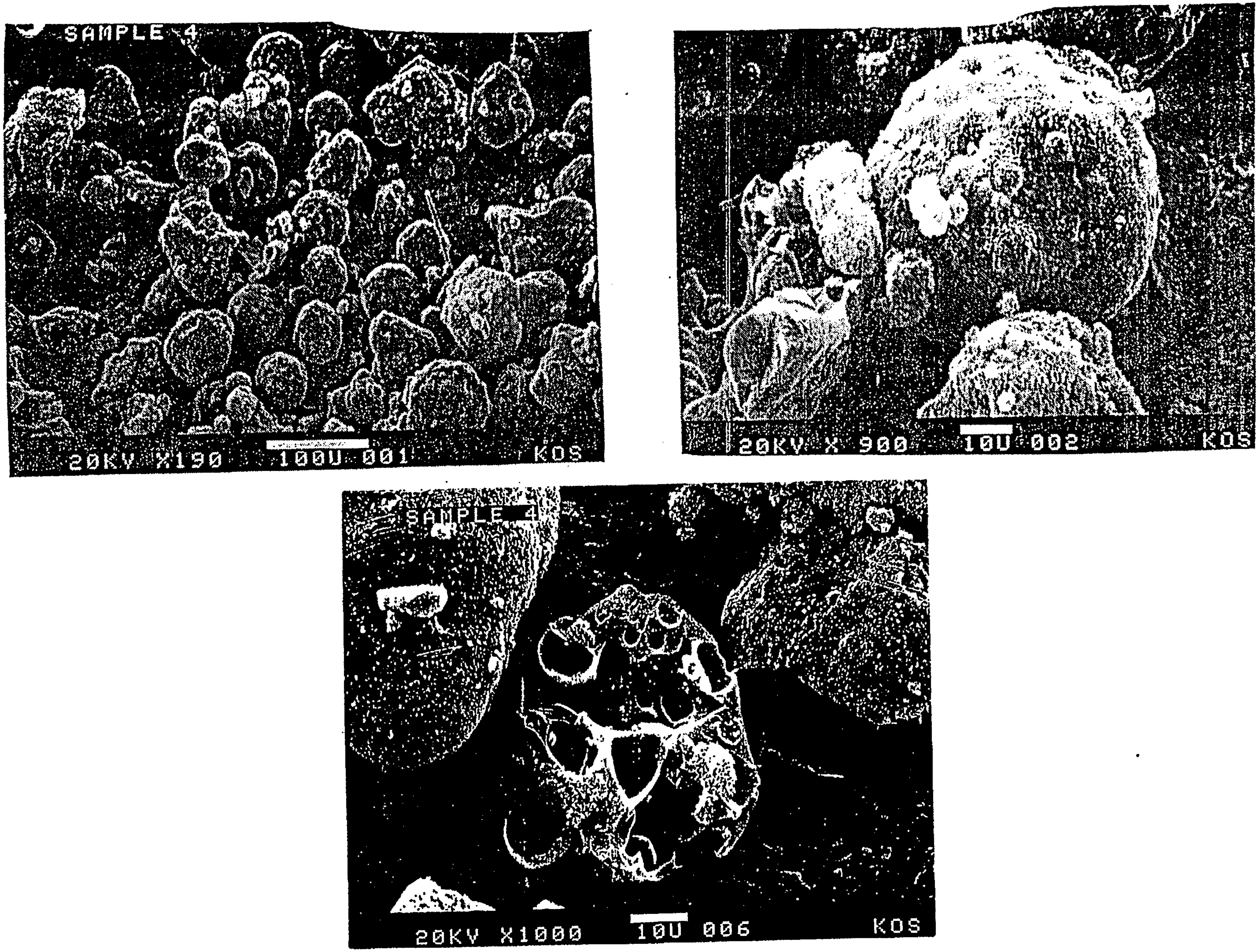

**Figure II.A.4-3** a) Field of "Popped" Particles, Formed when PDU Coal was Heated in Helium at ~3 x $10^4$ K/s to 1504° C. b) Close-Up of a Popped Particle. c) Internal Surface of a Fractured, Popped Particle.

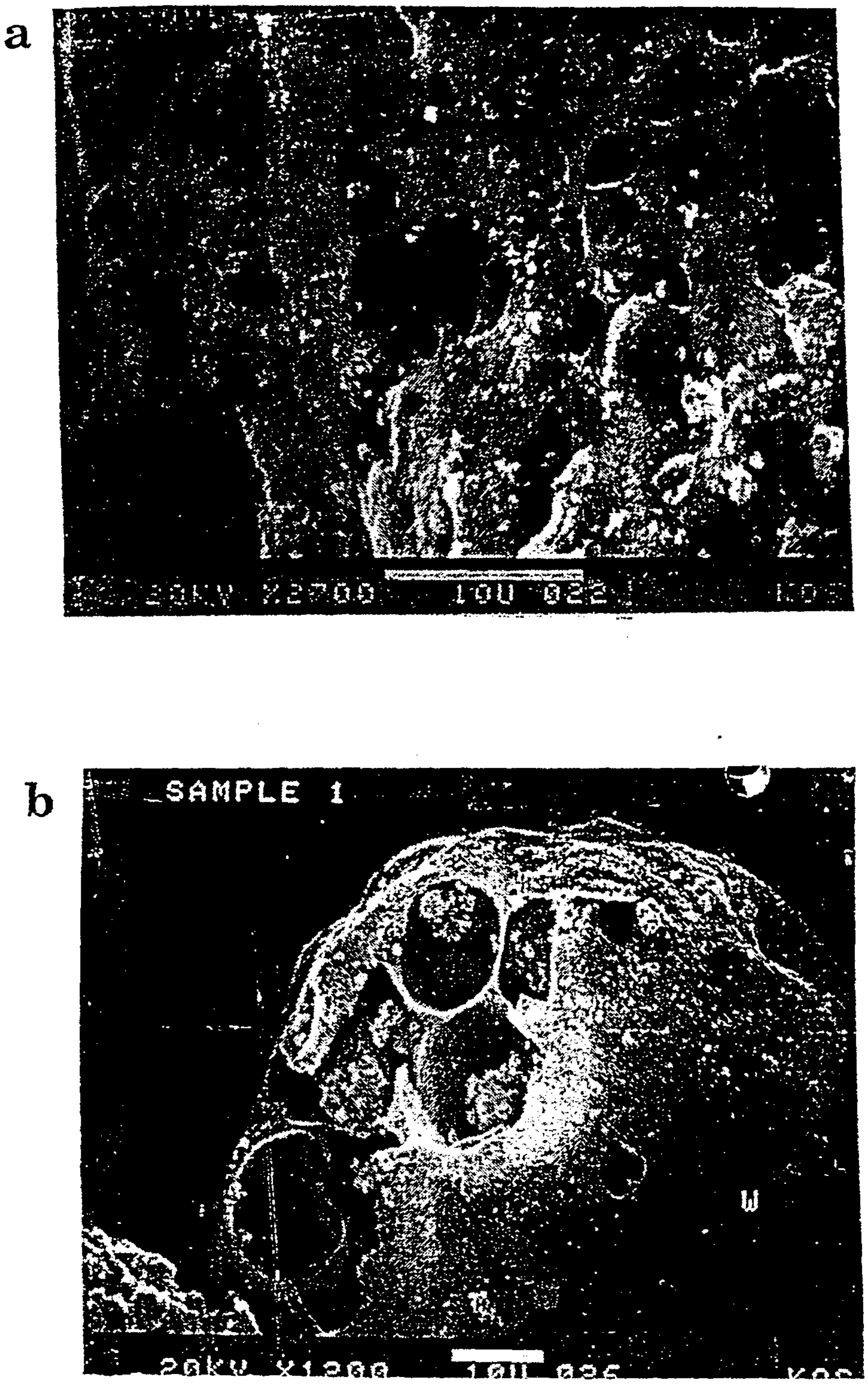

Figure II.A.4-4 a, b. "No- Model" Particles.

An internal pore of radius r will collect gas, n, at a rate proportional to its surface area:

$$\frac{dn}{dt} \propto r^2 \tag{II.A.4-1}$$

The internal pressure will be proportional to (collected gas)/volume:

$$P \propto \int \frac{r^2}{r^3} dt \propto \int \frac{1}{r} dt \tag{II.A.4-2}$$

The contracting force of surface tension also behaves as 1/r, therefore, for heating rates high enough so that there is insufficient time for appreciable inter-bubble transport, the time at which the outward gas pressure exceeds the inward surface-tension pressure, is the same for all bubbles. In that case a multitude of pores above micro-pore size will simultaneously swell: the no-model case. For longer times, the greater internal pressure in smaller bubbles (Eq. II.A.4-2), will cause the transfer of gas from small to larger bubbles. It is in this heating rate domain that the "single" and multi-bubble models apply.

In general, a slower heating rate will favor single-cell formation. Slower heating also allows more time for gas to escape by diffusion. Therefore, single-cell cenospheres will tend to be less swollen than multi-cell particles, which in turn are less swollen than no-model particles. Another factor which enhances the above trends in size is the ratio of internal to external surface area. Gas is evolved from the wall material, and the lowest internal to external surface area ratio of the single-cell particle marks it as the lowest swelling one.

In the modeling, the multi-cell particles are considered to be made up of a collection of single-cell cenospheres. The value of $r_2'$, the radius of coal material which contains only one bubble, is found to be 20$\mu$m to fit the data for most of the coals. The extrapolation of this single bubble model to large particles needs to be further investigated. The current model assumes that the number of bubbles in a particle of radius R is $(R/r_2')^3$.

The ruptured particles appear to follow a temperature history slower that that of the no-model particles. Inspection of cracked surfaces of these particles shows a number of internal bubbles not unlike that of the multi-cell particles. There is apparently time for coalescence for the smaller bubbles. Subsequent rapid gas evolution leads to cell wall rupture.

## Quantitative Model

The starting point for our quantitative model is the equation described by Chiou and Levine who considered the swelling rate of a pulverized coal particle of external radius $r_2$, with a single void of radius $r_1$, with spherical symmetry. The swelling they depict is due to the pressure, $\Delta P_t$, of trapped evolved gases, doing work against viscous forces (viscosity = $\eta$). Their equation was further modified in our work to take account of the pyrolysis weight loss.

For this single bubble model, the equation for the velocity of expansion of the outer wall is given by:

$$\frac{dr_2}{dt} = \frac{r_1^3 r_2 \, \Delta P_t}{4\eta(r_2^3 - r_1^3)} + \frac{r_2}{3(r_2^3 - r_1^3)} \frac{d(r^3)}{dt} \tag{II.A.4-3}$$

Where $r_1$ and $r_2$ are the radius of the inner and outer surfaces, respectively.

In our model, the temperature-dependent viscosity is supplied by the viscosity model. The accounting of excess internal pressure begins at t = 0, considering the gas gain from trapped, evolved gas, and loss due to out-diffusion. The number of moles of gas, $n_g$, evolved in one second, by the particle walls of volume, $\Delta v$, is obtained from the FG-DVC model, $\Delta v$ being updated to account for pyrolysis. Of the evolved gas, a fraction $r_1^2 / (r_1^2 + r_2^2)$ is captured within the void, so that the captured gas is given by:

$$dn_c = n_g r_1^2 / (r_1^2 + r_2^2) \bullet dt \qquad \text{(II.A.4-4)}$$

In this same period an amount of gas diffuses out:

$$dn_d = \frac{4\pi D_l c_1 dt}{(1/r_1 - 1/r_2)} \qquad \text{(II.A.4-5)}$$

where $D_l$ is the diffusivity of the gas in the coal liquid, $c_1 = 3 n_d / 4\pi r_1^3$, and the total gas within the cenosphere, $n_t$, is the "sum" of Eqs. 2 and 3.

$$\frac{dn_t}{dt} = \frac{dn_c}{dt} - \frac{dn_d}{dt} \qquad \text{(II.A.4-6)}$$

The excess of internal over external pressure, $\Delta P_g$, due to the trapped gas is given by:

The calculation of the amount of the trapped ambient gas $n_a$ follows a similar argument:

$$\Delta P_g = \frac{3 n_t RT}{4\pi r_1^3} \qquad \text{(II.A.4-7)}$$

$$\frac{dn_a}{dt} = \frac{4\pi D_a}{1/r_1 - 1/r_2} \left[ \frac{P_0}{RT} - \frac{n_a}{4\pi r_1^3 / 3} \right] \qquad \text{(II.A.4-8)}$$

where $P_0$ is the ambient pressure and $D_a$ the diffusivity of ambient gas. The pressure difference is then:

$$\Delta P'_t = \frac{3 (n_t + n_a) RT}{4\pi r_1^3} - P_0 \qquad \text{(II.A.4-9)}$$

where $P_0$ is the external pressure. The outward pressure is reduced by the effective negative pressure due to the surface tension, $\sigma$; so that the total outward pressure differential, $\Delta P_t$, is:

$$\Delta P_t = \frac{3\,(n_t + n_a)\,RT}{4\pi\, r_1^3} - \sigma\,(\frac{1}{r_1} + \frac{1}{r_2}) - P_0 \qquad \text{(II.A.4-10)}$$

This is the pressure difference used in Eq. II.A,4-3, to calculate swelling.

If $\Delta P'_t$ is sufficiently large, the stress in the wall will exceeded the strength of the wall $S_c$. Cell rupture is defined to occur when:

$$S_c \leq -P_0 + \frac{1.5\, r_1^3\, \Delta P'_t}{(r_2^3 - r_1^3)} \qquad \text{(II.A.4-11)}$$

The parameters of the model are: $D_l$, $D_a$, $\sigma$, and $S_c$, which are listed in Table II.A.4-1.

**Table II.A.4-1. Swelling Model Parameters**

| | |
|---|---|
| Apparent Pyrolysis Gas Diffusity, $cm^2$/sec | $7.5e-5(T/773)^{1.8}$ |
| Apparent Ambient Gas Diffusivity, $cm^2$/sec | 7.5e-4 |
| Critical Bubble Wall Stress, atm | 1.0 |
| Surface Tension | 30 dyne $cm^{-1}$ |

Another input to the model is the temperature history of the particle. For the modeling of some experiments on coal pyrolysis in the entrained flow reactor, we used particle temperature histories which were furnished by an experimentally verified model. For other situations we used a two straight-line segment temperature history representation in the model. The first segment represents the heating rate, the second segment the final particle temperature.

For monodisperse coal particles, we expect to be able to draw a "phase diagram" such as depicted in Fig. II.A.4-5. From drop tube experiments we determined the value of Tmin to be 520 °C. In conjunction with the swelling model results this observation was used to fix the diffusivity at $7.5\mathrm{x}10^{-5}$ $cm^2$ sec. We later incorporated a temperature dependence into $D_1$.

In quantitative exercising of the model, the swelling of P.S.C. particles of small and intermediate size were predicted to within ±25%, for a wide range of heating rates. The effect of external pressure on the swelling of an Illinois #6 coal was predicted to the same level of accuracy (Fig. II.A.4-6). In looking at reasons for that behavior it was seen that with increasing pressure the more volatile components of tar were held in the particles for longer times, decreasing viscosity at the critical time of gas evolution. With further increase in pressure the compressive external environment made itself felt, and swelling was reduced (Fig. II.A.4-6).

In parallel calculations it was found that for a range of (model imposed) maximum fluidities the swelling of P.S.C. #8 coal particles did not change until a value of 4.3 DDMP (Fig. II.A.4-7). These results, at first, appear to contradict the stated swelling behaviors of the Illinois #6 coal described in Fig. II.A.4-6: increased swelling with decreased viscosity. Agreement does exist, however, as the maximum fluidity of Illinois #6 coal at one atmosphere is 2.9 DDMP, which is in the region of the curve of Fig. II.A.4-7 where swelling is viscosity dependent.

# SWELLING MAP

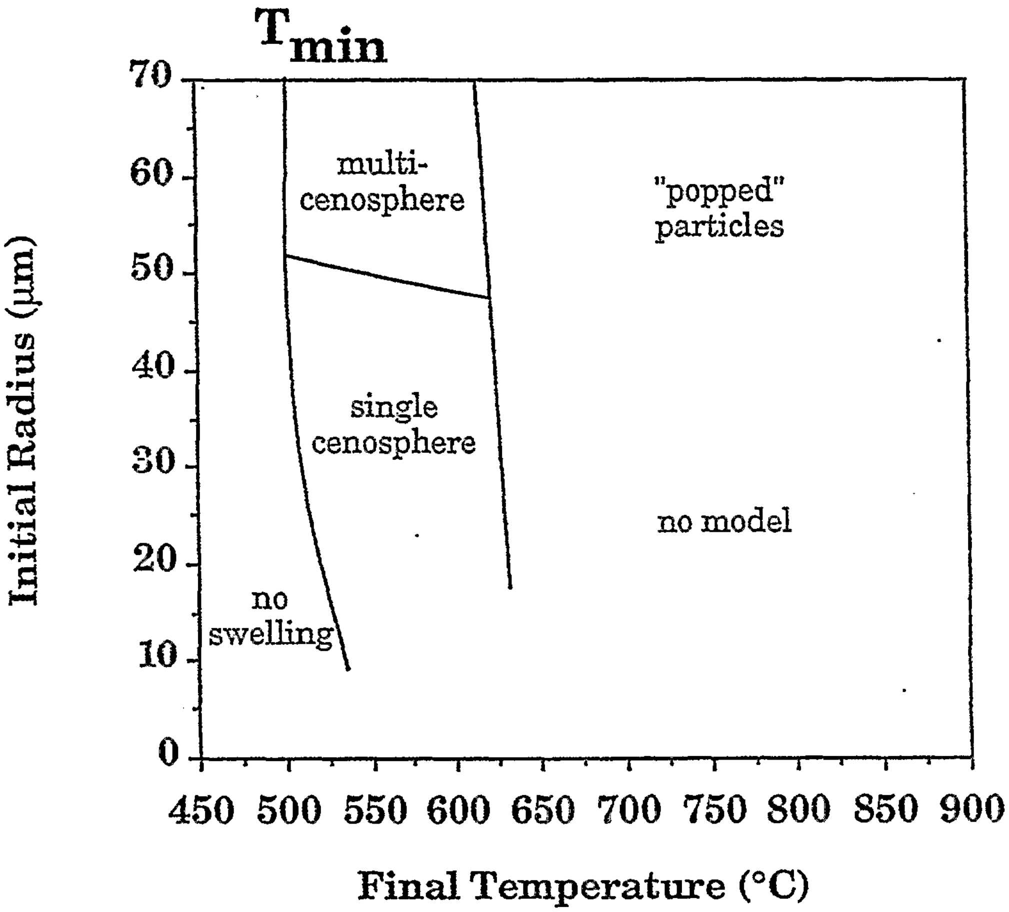

**Figure II.A.4-5.** Schematic Swelling Map Showing Dependence of Swelling Type on Initial Particle Radius and Final Temperature, High Heating Rate (~$10^4$ K/s). Heating Rates and Maceral Type are Also Important Factors in Swelling Behaviour.

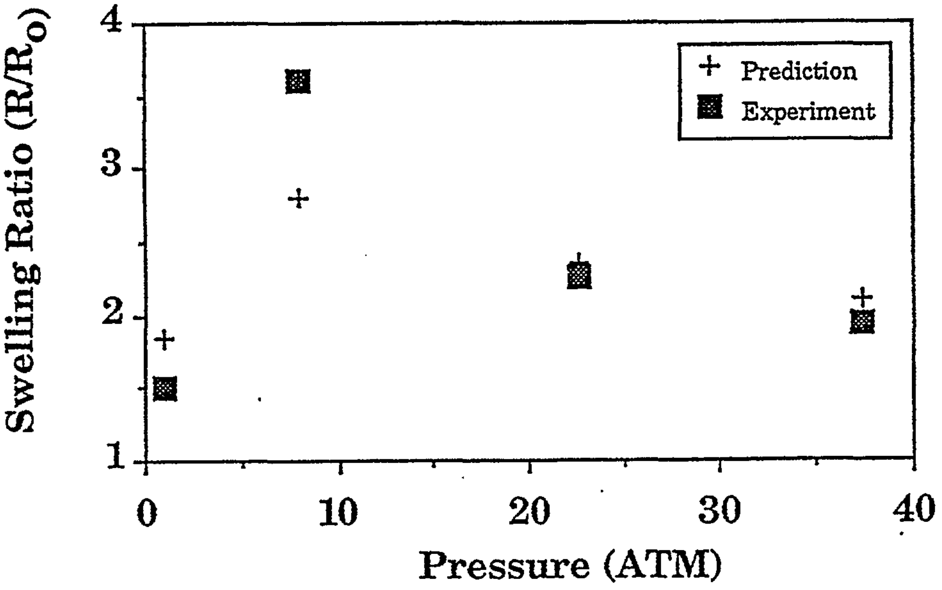

**Figure II.A.4-6.** Comparison of Model Prediction and Experiment (Lee et al.) for Swelling Ratio Versus Ambiant Pressure, for Illinois #6 (Nominal Rad = 31μm), at a Heating Rate of Between 1000 and 1150 K/s.

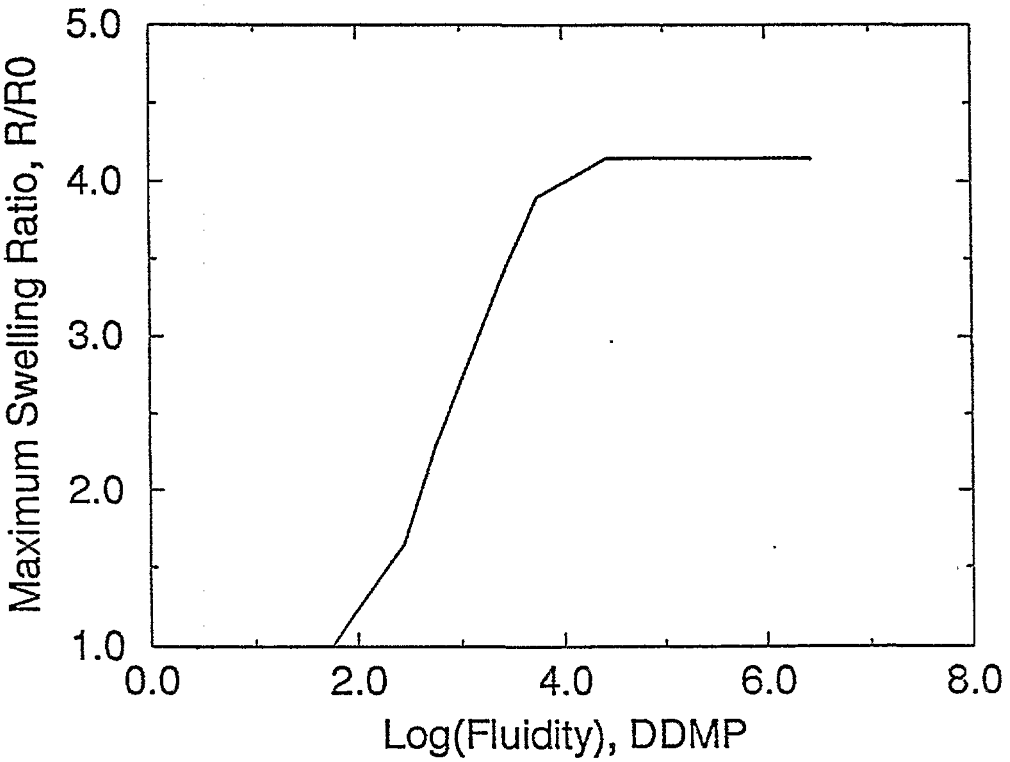

**Figure II.A.4-7.** Calculated Maximum Swelling Ratio for Model Imposed Maximum Fluidities, as Shown.

## Other Considerations

In the swelling model work, analysis other than that based on swelling calculations was made. This section deals with the question of the relationship between swelling and reactivity, via surface area. It is a chronicle of reasons why a thorough knowledge of char swelling will not lead to predictions of reactivity.

Zygourakis (1989) has examined sectioned chars microscopically, using image processing techniques to deduce porosity, swelling, and surface area. His optical technique has resolution only down to O.5 $\mu$m, and with this he deduces a maximum surface area of about 0.08 $m^2$/cc of particle. But this is two orders of magnitude less than areas measured by BET and other gas adsorption techniques (Gan, et al., 1972). Consequently, it is concluded that most of the surface area of a char is in micropores. However, the swelling model predicts no swelling for pores as small as micropores, as gas collection is low and the surface tension is high. Therefore, swelling cannot be a direct major factor in the development of pore surface area or reactivity. On the other hand, it has been shown that swelling can effect the access of gas to the reactive areas. A study of this relationship has not been made.

Also, during the course of this work, we checked Simon's pore-tree model with the swelling calculations, as follows. The model includes an empirically chosen constant, which represents the number density of cavity "nuclei" in the coal. An investigation was made to relate the predictions made by Simon's pore-tree model to our observations of swelling particles. If successful, the pore-tree model would serve as a basis for choosing the number density of cavities.

To begin with, we used Suuberg's adaption of Simon's pore-tree model for this study. Suuberg found that the excess internal pressure is inversely proportional to diameter, as in Eq. II.A.4-2. This means that as temperature, and hence, pressure increases, a point will be reached at which all internal pores begin to swell, more or less at the same time. This is the condition for the "no-model" expansion, described in the qualitative discussion, above. With this model, and input from the FG-DVC model, it was calculated that for low and moderate heating rates the internal excess pressure never exceeded 1% of the effective pressure due to surface tension, at a temperature at which heated vitrinite particles are observed to swell.

This result implies that the pore-tree model is not appropriate to use for the swelling phase of heated coal particles. The results of the calculation were checked by going back to Simon's original work, but changing the bulk density value, and $r_{min}$, in accordance with Suuberg's observations. Again, predicted pressures were always too low by about one and a half orders of magnitude when compared with the observed swelling of small particles of Pittsburgh seam coal The narrowest conclusion that we can draw here is that the pore tree model should not be used to predict the swelling of bituminous coals at low and medium heating rates.

An application of the swelling model could be in the description of the interception of flame radiation by swollen particles. Such an estimate would be more realistic if the swelling were performed in an oxidizing atmosphere, rather than the inert gas environment used for the model so far.

## Conclusions

A viable model for the swelling of pyrolyzing pulverized coal particles has been developed and refined. The model semiquantitatively predicts swelling behavior for all cases considered, to within ± 25%. In principle, the model is applicable to all of the Argonne coals, at heating rates between 1 and $5\times10^4$ °C per second, and for a variety of ambient pressures. Further refinements of the model depend on obtaining a greater array of data.

## II.A.5. Sulfur and Nitrogen Evolution

Sulfur and nitrogen evolution from the Argonne premium coals has been studied using

Thermogravimetric Analysis with measurement of evolved products by Fourier Transform Infrared spectroscopy (TG-FTIR). The method combines temperature programmed pyrolysis and combustion. $H_2S$ and tar sulfur were monitored by measuring $SO_2$ after oxidation of volatile products. The $SO_2$ evolution curves produced with volatile oxidation exhibit two main evolution peaks and one smaller high temperature evolution peak. For each peak, the temperature of the maximum evolution rate ($T_{max}$) increases with increasing rank. The individual evolution curves of the organic and pyritic sulfur were identified, and their evolution kinetics were derived. The overall $SO_2$ evolution curves were modeled by using the FG-DVC coal pyrolysis model. The evolution curves for both $NH_3$ and HCN show an increase in $T_{max}$ with increasing rank. $NH_3$ is the dominant product at low heating rate. Results from previous high heating rate experiments show that HCN is the dominant product. Experiments show that tar cracking at high temperatures is not a major contributor to HCN formation. The heating rate dependence of the conversion of coal nitrogen to HCN and $NH_3$ is believed to be due to the secondary reaction of HCN and coal hydrogen in the char pores to produce $NH_3$. This reaction can be completed with enough gas residence time within the char pores. At high temperature, the residence time is reduced and HCN conversion does not occur. Such a reaction sequence was added to the FG-DVC model and the kinetics were derived.

## Introduction

Although sulfur and nitrogen are small contributors to the mass of coal, their oxides are significant contributors to environmental pollution. Understanding the mechanism of the transition from coal sulfur and nitrogen to the pollutant gas species is crucial for more efficient and cleaner coal utilization. The objective of this work was to study the evolution of sulfur and nitrogen from the Argonne Premium coals during pyrolysis and to employ the data to develop a model for sulfur and nitrogen evolution during pyrolysis.

To develop the model, sulfur and nitrogen reactions are being added to the FG-DVC model of coal pyrolysis which describes the evolution of tar and carbon, hydrogen, and oxygen gas species. The FG-DVC model combines a functional group (FG) model for gas evolution and a statistical depolymerization, vaporization and crosslinking (DVC) model for tar formation (Solomon, et al., 1988a; 1990a). The FG model describes the evolution of gases from sources in the coal, char and tar. The DVC model describes the decomposition and condensation of a macromolecular network representation of coal under the influence of bond breaking and crosslinking to predict the molecular weight distribution of the network fragments. The network is composed of fused aromatic rings connected by aliphatic bridges. Previous work (Solomon, et al., 1993) with the FG-DVC model has derived the functional group compositions and evolution kinetics for C, H and O volatile species in the Argonne Premium coals.

The pyrolysis instrument employed in this study couples thermogravimetric (TG) analysis with quantitative fourier transform infrared (FT-IR) analysis (TG-FTIR). In a previous study using this TG-FTIR programmed temperature pyrolysis and combustion technique, the major volatile products evolving from the Argonne Premium coals were investigated (Solomon, et al., 1990b).

The forms of sulfur in coal have been studied by a number of investigators (Kelemen, et al., 1991; Huffman, et al., 1991; LaCount, et al., 1992; Boudou, et al., 1987; and Calkins, 1987). Sulfur exists in coal in three forms: organic sulfur, pyritic sulfur and sulfates. Organic sulfur exists in the coal structure, either in aromatic rings or in aliphatic functional groups. Pyrite exists in coal as dispersed particles, but interactions with the coal structure during pyrolysis are expected. Sulfate is only a very small part of the total sulfur in most coals, especially in the Argonne Premium coals (Vorres, 1989). The recent application of XPS and XANES (Kelemen, et al., 1991) and XAFS (Huffman, et al., 1991) to the study of organic sulfur forms has identified the amounts of aliphatic and aromatic sulfur in the Argonne Premium coals.

During coal devolatilization, the various forms of sulfur decompose into gas species including $H_2S$, COS, $SO_2$, and $CS_2$. A large amount of sulfur remains in the char and some of the sulfur is evolved with the tar. Among all the volatile sulfur containing species, $H_2S$ and tar sulfur are the most abundant during coal pyrolysis. Since $H_2S$ is a very weak IR absorber and tar sulfur is difficult to quantify, a post oxidation technique (Solomon, et al., 1990b) has been employed to oxidize $H_2S$ and the other sulfur containing gas species to $SO_2$ which is easily detected by FTIR.

Most of the coal nitrogen is in pyrrole and pyridine structures, which are aromatic. There is very little evidence of amine groups in coal (Burchill, 1987; Wallace, et al., 1989). The most significant evolution gases are HCN and $NH_3$. Both HCN and $NH_3$ are strong IR absorbers, and can be easily observed in pyrolysis. There is evidence (Wallace, et al., 1989) showing that the relative abundance of HCN and $NH_3$ depends on the pyrolysis temperature. Some workers (Baumann and Moller, 1991; Usman and Wendt, 1990; and Bose, et al., 1988) believe that HCN precedes the $NH_3$ formation during combustion and that secondary conversion of HCN to $NH_3$ is possible. Since amounts of HCN and $NH_3$ are the main factors in $NO_x$ formation (Bose, et al., 1988), their evolution kinetics need to be investigated.

In this paper the experimental section presents a description of the TG-FTIR apparatus and the techniques for determining kinetics and pyrolysis mechanisms. Next, sulfur results are presented followed by sulfur modeling. The paper then presents nitrogen results and modeling.

## Experimental

The TG-FTIR system employed in this study was the TG/plus from Bomem, Inc., and its details have been presented elsewhere (Solomon, et al., 1990b; Carangleo, et al., 1987; and Whelan, et al., 1988). Its components are as follows: a DuPont 951 TGA, a hardware interface, an Infrared Analysis 16 pass gas cell with transfer optics, and a Bomem Michelson 110 FT-IR (resolution, 4 $cm^{-1}$; detector, MCT). A helium sweep gas (250 $cm^3$/min) is employed to bring evolved products from the TGA directly into the gas cell. The system is operated at atmospheric pressure.

The programmed temperature pyrolysis and combustion profile is as follows: A 20 mg sample loaded in the platinum sample pan of the DuPont 951 is taken on a 30°C/min temperature excursion in helium first to 150°C to dry for 4 minutes and then to 900°C at 30°C/min for pyrolysis. Upon reaching 900°C and holding the temperature for 3 minutes, the sample is cooled to 250°C over a 20 minute period. After cooling, a small flow of $O_2$ (20 $cm^3$/min) is added to the helium sweep gas and the temperature is ramped to 900°C in order to combust the remaining char. Infrared spectra are obtained once every 41 seconds.

A post oxidation method was employed to collectively study sulfur evolution. In this procedure, heat (approximately 900°C) and oxygen (10 $cm^3$/min) is added to the volatile product stream after the furnace but before the gas analysis cell. This added step allows detection of $H_2S$, a very weak infrared absorber; elemental sulfur; and tar sulfur by monitoring $SO_2$ evolution rate. Details of this post oxidation method appear elsewhere (Solomon, et al., 1990b).

The samples studied in this work were the Argonne Premium Coal samples. The effects of pyrite were examined through the analysis of depyritized Argonne Premium Illinois #6 and Pittsburgh #8 coals as well as a pure pyrite sample from Custer, South Dakota.

Figure II.A.5-1 presents the DAF weight percent sulfur values determined by the TG-FTIR in comparison with those values provided by Argonne National Laboratory (Vorres, 1989). With the exception of Zap lignite and Wyodak coal, the TG-FTIR results are within 16 % of Argonne's data. For Zap lignite and Wyodak coal, the TG-FTIR data is 36 % and 45 % respectively lower than the Argonne data. Possible explanations for this large discrepancy are that sulfur is being incorporated in the ash or evolving as gaseous $SO_3$. Examination of the TG-FTIR absorbance spectra, however, show no $SO_3$ evolving during combustion.

## Sulfur Results and Discussion

The Argonne premium coals were subjected to regular pyrolysis and pyrolysis with the post oxidizer. Presented in Figure II.A.5-2 are the COS and $SO_2$ evolution curves from regular pyrolysis of Zap lignite and Wyodak, Illinois #6, and Utah Blind Canyon coals. The COS is formed by reaction of pyrite or

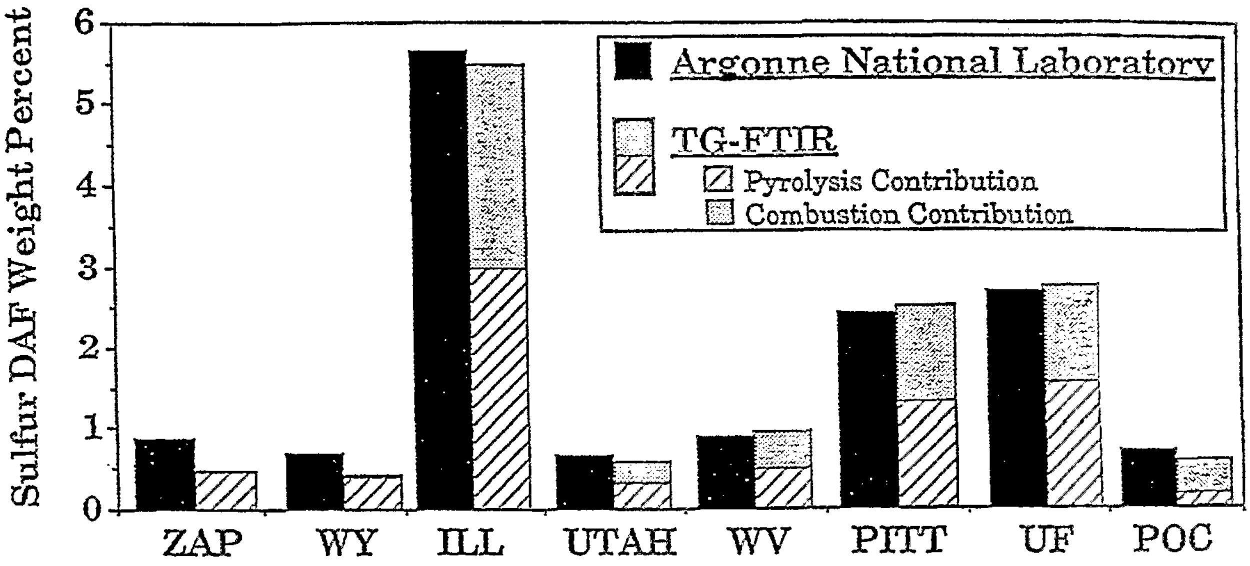

Figure II.A.5-1. DAF Sulfur Weight Percent Values Determined by TG-FTIR Compared with those Provided by Argonne National Laboratory (Vorres, 1989)

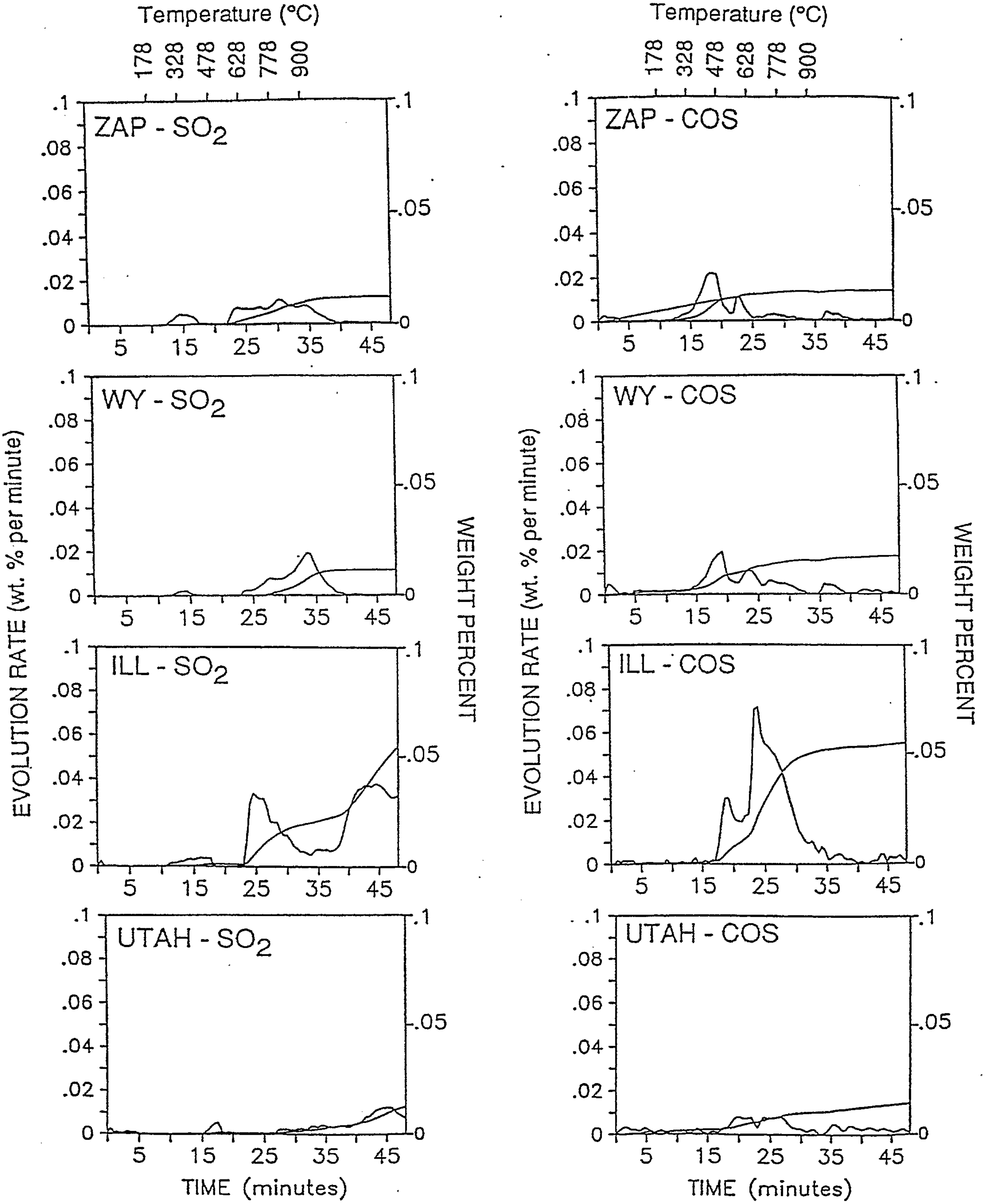

Figure II.A.5-2. COS and $SO_2$ Evolution Curves from Regular Pyrolysis of Zap Lignite and Wyodak, Illinois #6 and Utah Blind Canyon Coals.

sulfur formed during pyrite decomposition with CO (Calkins, 1987). The $SO_2$ is formed from sulfates which can be present in small amounts in some coals, particularly weathered ones (Calkins, 1987). Presented in Figure II.A.5-3 are the $SO_2$ evolution and weight curves from pyrolysis of all eight of the Argonne Premium coals with post oxidation of volatile products. Compared with the post oxidized $SO_2$ evolution curves, the contributions of COS and pyrolysis $SO_2$ to the total sulfur evolution are minute. It is obvious that $H_2S$ is the major sulfur containing gas specie evolving during coal pyrolysis and consequently, only $H_2S$ gas evolution has been included in modeling. Furthermore, subsequent discussion of pyrolysis $SO_2$ evolution will refer to the collective $SO_2$ evolution formed from post oxidation of pyrolysis products.

The $SO_2$ evolution curves presented in Figure II.A.5-3 exhibit two main evolution peaks and one smaller high temperature evolution peak, although each peak is more precisely a collection of smaller peaks. For each main evolution peak, the temperature of the maximum evolution rate ($T_{max}$) increases with increasing rank. Similar rank dependance has been reported by Kelemen et al., 1991 and Oh et al., 1988. Furthermore, the low temperature $SO_2$ evolution peak coincides with the coal's tar evolution peak.

With the post oxidation apparatus installed on the TG-FTIR instrument, small amounts of oxygen were able to diffuse from the post oxidation chamber to the remaining char sample resulting in mild oxidation at high temperatures. In Figure II.A.5-3, the $SO_2$ evolution seen beyond 37 minutes is believed to be from decomposition of the pyrrhotite (FeS).

**Fraction of Volailte Sulfur** - The $SO_2$ weight curves in Figure II.A.5-3 offer the quantitative amounts of sulfur volatilized during pyrolysis. By dividing the volatile sulfur values by the amount of total sulfur in the parent coals, the volatile sulfur fractions for each coal were generated and are presented in Fig. II.A.5-4 on a DAF basis. For all the coals except Pocahontas #3, the volatile sulfur fractions are from 0.5 to 0.6. For Pocahontas #3, only 34% of total coal sulfur is volatile. This may be attributed to its high aromaticity, low tar yields, and low aliphatic sulfur content. More discussion of the rank dependence of sulfur evolution is to be presented below.

**Aliphatic Sulfur Contribution** - Figure II.A.5-5 presents data concerning the origin of the low temperature $SO_2$ evolution peak. In this figure, the fraction of total organic sulfur evolved during the first $SO_2$ peak is plotted as a function of the oxygen content in the parent coal (Vorres, 1989) using oxygen as a simplified measurement of rank. A very interesting rank correlation can be seen where, with the exception of Zap lignite, the low rank coals release a much larger fraction of their organic sulfur during the low temperature peak than the high rank coals. Since low rank coals are more aliphatic by nature, the plot suggests that the main contributor to the low temperature $SO_2$ peak is aliphatic sulfur. This idea is supported by the work of Mehldi Taghiei et al. (1991) which indicates that the aliphatic sulfur is much less stable than the aromatic sulfur, consistent with its evolution under the low temperature evolution peak.

**Pyritic Sulfur Contribution** - As mentioned in the introduction, pyrite exists in coal as dispersed particles. The mechanism for thermal decomposition should be similar to that for pure pyrite, although some coal/pyrite interactions are expected.

To understand the pyritic sulfur contribution to the $SO_2$ evolution curves, Illinois #6 and Pittsburgh #8 coals were subjected to ASTM D-2492 (ASTM, 1985) under a nitrogen atmosphere. In this method, sulfate sulfur is extracted from the coal with dilute hydrochloric acid and pyrites ($FeS_2$) are removed using dilute nitric acid. Results from temperature programmed pyrolysis and combustion of raw and ASTM D-2492 modified Illinois #6 coal are presented in Figures II.A.5-6 and II.A.5-7 respectively. Figures II.A.5-6a and II.A.5-7a are the balance and thermocouple curves and Figures II.A.5-6b and II.A.5-7b are the $SO_2$ evolution and weight curves. The tar evolution curve for the raw Illinois #6 coal (obtained without the post oxidizer) is included in Figure II.A.5-6a to demonstrate how the tar peak overlays the low temperature $SO_2$ peak. The ASTM D-2492 procedure removed the second $SO_2$ pyrolysis peak as well as the "sharp" portion of the combustion cycle $SO_2$ peak. The pyrite ($FeS_2$) is believed to decompose during pyrolysis to form pyrrhotite (FeS) and sulfur. The pyrrhotite then remains relatively stable until $O_2$ is added to the helium sweep gas and the char is heated to 900°C for combustion of the remaining char. During the harsh

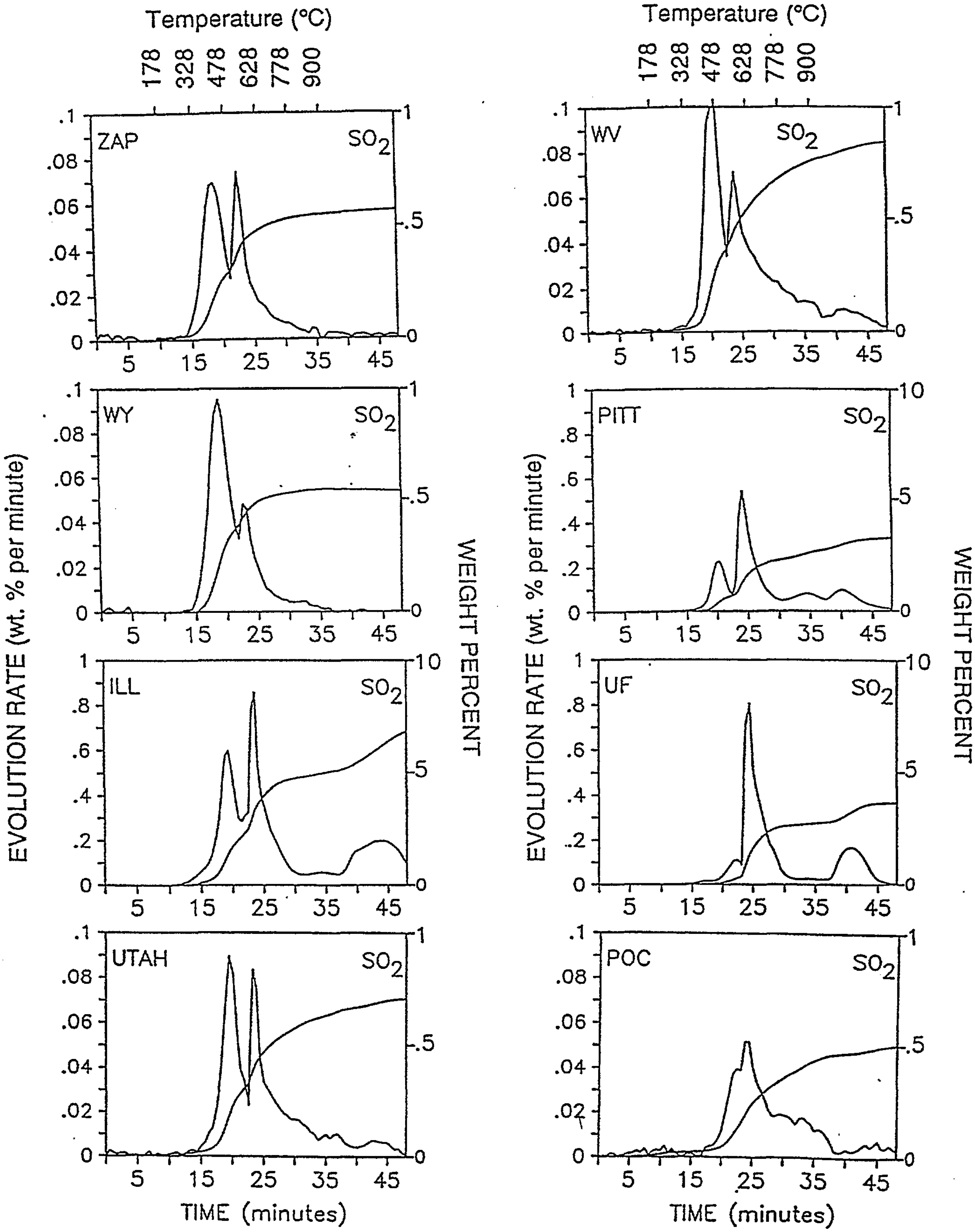

Figure II.A.5-3. $SO_2$ Evolution and Weight Curves from Post Oxidized Pyrolysis of the Argonne Coals.

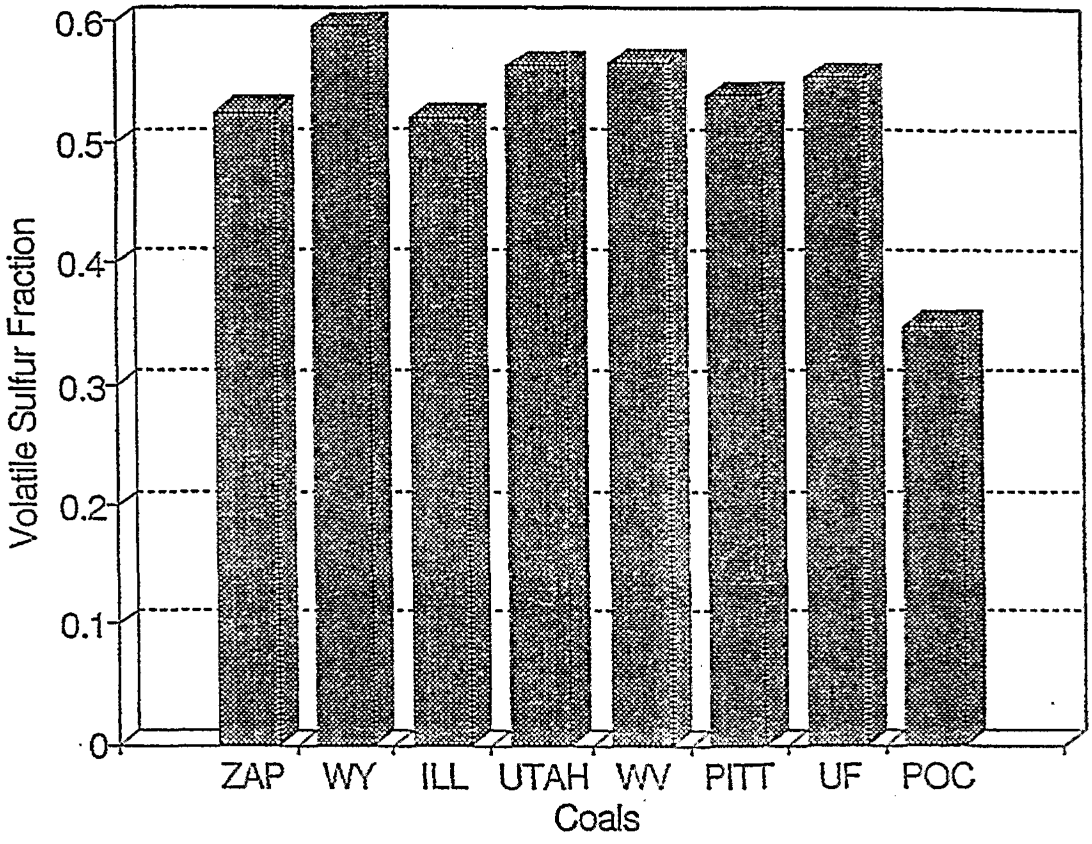

Figure II.A.5-4. Fraction of Volatile Sulfur in the Argonne Coals Determined by Post Oxidized Pyrolysis in the TG-FTIR.

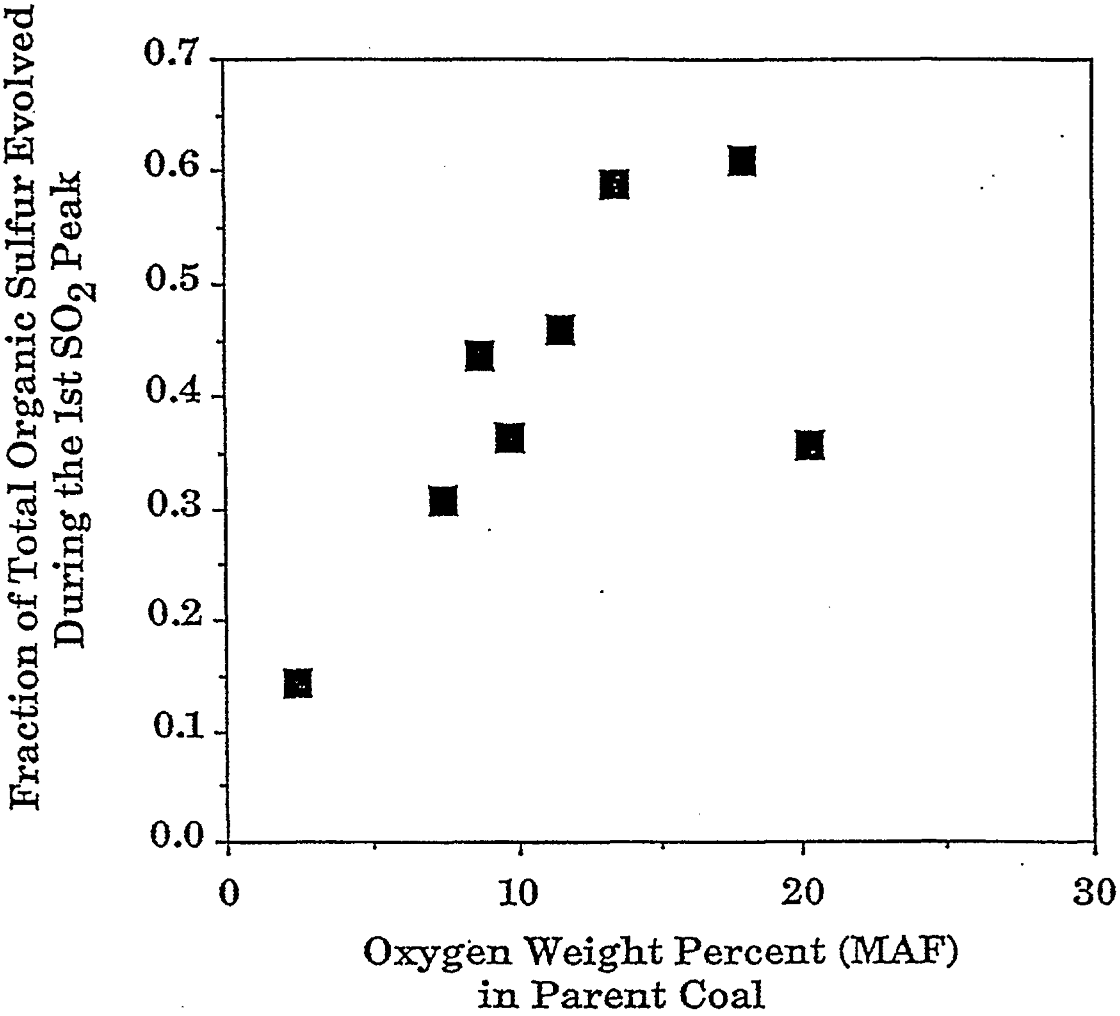

Figure II.A.5-5. Fraction of Organic Sulfur Evolved from the Argonne Coals During the First $SO_2$ Evolution Peak (Post Oxidized Pyrolysis) Plotted as a Function of Oxygen in the Parent Coal.

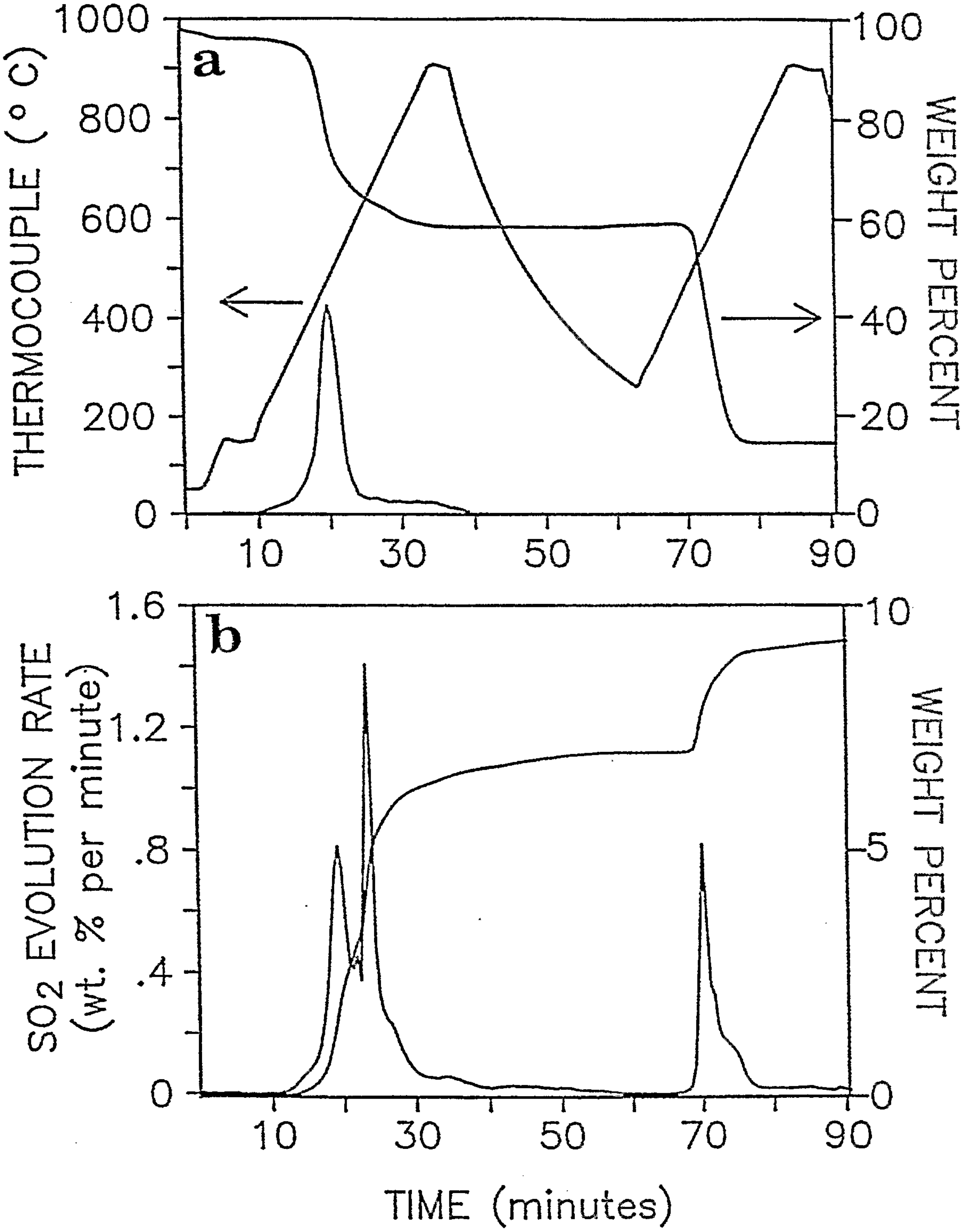

Figure II.A.5-6. Results from Post Oxidized Pyrolysis of Illinois #6 Coal. a) Balance, Thermocouple and Tar Evolution Curves and b) $SO_2$ Evolution and Weight Curves.

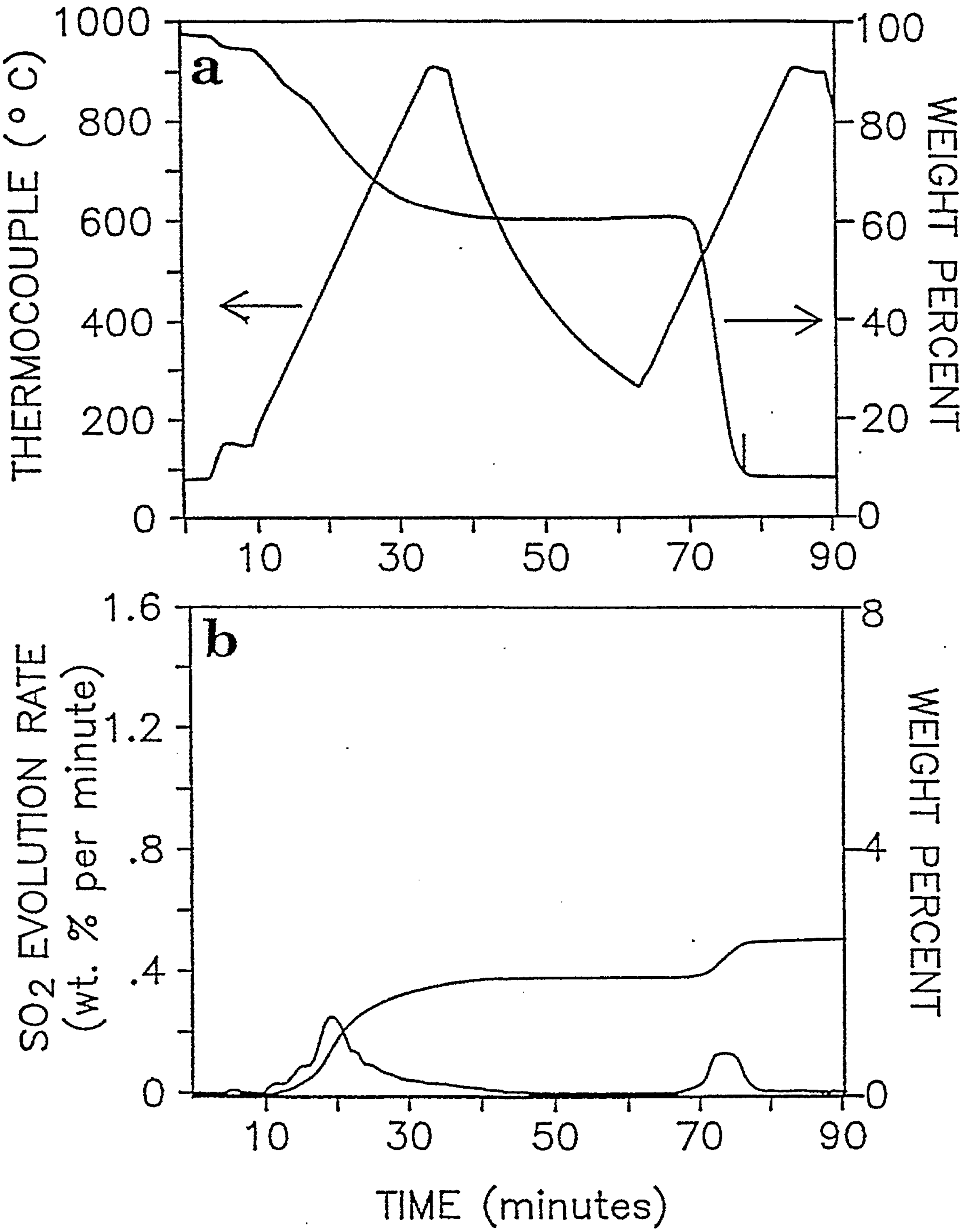

Figure II.A.5-7. Results from Post Oxidized Pyrolysis of ASTM D-2492 Modified Illinois #6 Coal. a) Balance and Thermocouple Curves and b) $SO_2$ Evolution and Weight Curves.

conditions of combustion, the pyrrhotite decomposes to form $Fe_2O_3$ and $SO_2$. To compare the behavior of coal pyrite with pure pyrite, a pure pyrite sample from Custer, South Dakota was subjected to temperature programmed pyrolysis and combustion. The pyrite evolution curve (not shown) has a single $SO_2$ $T_{max}$ at 610°C which is slightly higher than that of Upper Freeport coal (603°C). The study by Mehldi Taghiei et al., (1991) shows that after pyrolysis, the decomposition of coal pyrite is complete and that FeS sulfur represents half of the retained sulfur in an Illinois #6 coal. Since Illinois #6 has about 50% of the total coal sulfur in pyrite and it lost about 50% of the total sulfur in pyrolysis (Figure II.A.5-4), it can be deduced that the retention of FeS is almost 100% and that it is stable throughout the pyrolysis. Consequently, 50% of the pyritic sulfur evolves and the other half remains in coals as FeS.

In addition to removing the peaks indicative of pyrite, the ASTM D-2492 procedure also removed a substantial portion of the low temperature $SO_2$ pyrolysis peak. In recent work, Gorbaty et. al. (1992) found that the aliphatic sulfur in coals subjected to 125°C in air for 5 days was selectively transformed to oxidized organic sulfur forms and that most of these oxidized sulfur forms were retained in the char after 400°C pyrolysis as either sulfur oxides or aromatic sulfur. Since nitric acid is a strong oxidizing agent, the majority of the decrease in the low temperature $SO_2$ evolution peak is probably due to the oxidation of the coal's aliphatic sulfur. It is possible however that a small amount of $FeS_2$ in coal does decompose during the low temperature $SO_2$ evolution peak, as low and high temperature $FeS_2$ decomposition has been reported by others (Oh, et al., 1988; Khan, 1989). Temperature programmed pyrolysis and combustion of raw and ASTM D-2492 modified Pittsburgh #8 coal showed trends similar to the Illinois #6 coal.

As noted from Figure II.A.5-3, the $SO_2$ $T_{max}$ which is a result of pyrite decomposition demonstrates rank dependence. The $SO_2$ $T_{max}$ increases from 555°C in the case of Zap lignite, to 603°C in the case of Upper Freeport coal. It is unclear as to why pyrite in coal is rank dependent. Pyrolysis experiments were done with pyrite/coal mixtures and with pure pyrite with small flows of $CO_2$, CO, $H_2O$, $H_2$, and $C_2H_6$ added to the helium sweep gas with no success in lowering the pyrite decomposition temperature. In all the experiments, the pyrite decomposition temperatures showed little variation. Pyrite decomposition in coal occurs at a time when there is an abundance of free radical formation. Consequently, the pyrite dispersion throughout the coal matrix and the coal/pyrite interaction is probably the key factor which causes earlier decomposition of pyrite during coal pyrolysis.

## Sulfur Modeling

Modeling of coal sulfur evolution was performed by employing our FG-DVC coal pyrolysis model (Solomon, et al., 1988a; 1990a; and 1993). FG-DVC terminology divides the total coal sulfur into a number of precursor pools that would evolve during the pyrolysis with different kinetics. The evolution of each pool is modeled using a distributed activation energy approach (Solomon et al., 1988a) to represent the diversity of the chemical structure of coals. The pool composition and kinetics were determined by fitting the model to the data collected in this work. The procedure was based on the physics and understanding of coal sulfur established previously by the work of Gorbaty and the coworkers (1992), Calkins and the coworkers (1987), Huffman and coworkers (1991), and LaCount and the coworkers, (1992). It needs to be noted that our model, as all engineering models, represents a simplified picture of the complicated processes involved in the coal sulfur evolution. However, efforts were made to maintain the basic physics for the pool assignment so that the model contains the minimum set of processes that are needed for it to be physically significant.

Figure II.A.5-3 has shown that sulfur pyrolysis evolution spans continuously over a wide temperature range of 400°C to 800°C at 30°C/min. We classify the evolution sequence into three groups of peaks, i.e., low temperature, intermediate temperature and high temperature groups. The low temperature group consists of peaks that evolve at temperature lower than that of the sharp pyrite peak. The intermediate temperature group has only one member which is the sharp pyrite peak. The high temperature group is located at temperatures higher than the pyrite decomposition temperature and is a broad shoulder. Each group of peaks have contributions from the evolving organic and pyritic sulfur. Sulfatic sulfur contributes an insignificant amount of the total sulfur and was not modeled here. Besides the gaseous sulfur species, another contributor is the tar sulfur that is chemically part of the tar when it evolves. This type of mechanism is contained in the FG-DVC tar evolution algorithm (Solomon, et al., 1988a), and does not need to be addressed here. As indicated above (Figure II.A.5-6), the tar evolution peak coincides with the low temperature group of peaks. The sulfur evolution was modeled as $H_2S$ evolution, since it is known that $H_2S$ is the major component in the sulfur gases evolved in the pyrolysis. Although the model also has COS and $SO_2$ pools, they are treated as background to the $H_2S$ peaks and are only of trace amount.

As identified by the direct measurements of sulfur forms in coal (Kelemen, et al., 1991; Huffman, et al., 1991), organic coal sulfur can be aromatic and aliphatic. It is understood that the aliphatic sulfur is less stable than the aromatic sulfur during pyrolysis and that aliphatic sulfur evolves at lower temperature (Mehldi Taghiei, et al., 1991). The aromatic sulfur which is in the coal aromatic ring structure is more stable to thermal exposure. This leads to classifying the organic sulfur into two precursor pools, i.e., the aliphatic sulfur (loose) and the volatile aromatic sulfur (tight) pools, and one char sulfur pool. The aliphatic pool contains all the aliphatic sulfur and is the major contributor of the low temperature group. The volatile aromatic pool has the volatile portion of the aromatic sulfur which evolves at high temperature. The char pool has the rest of the organic sulfur that does not evolve during pyrolysis.

According to the work by Khan (1989), the pyritic sulfur decomposes mainly through the reaction $FeS_2 \rightarrow FeS + S$. The FeS remains stable during pyrolysis. This suggests that 50% of the pyritic sulfur is volatile and will evolve as $H_2S$ mainly under the sharp spike shown in Figure II.A.5-3. Although there is no direct evidence showing that coal pyrite evolves at temperature other than its intrinsic temperature, we tentatively use three pyrite pools, i.e., low temperature (loose), intrinsic (tight), and high temperature (extra tight) pools to enable us to model the alternative routes of pyrite decomposition. The tight pool corresponds to the pyrite spike and should contain most of the volatile pyritic sulfur. The model sketched above is schematically shown in Figure II.A.5-8. The overall sulfur evolution is now modeled with one tar sulfur peak, two $H_2S$ peaks from organic sulfur, three $H_2S$ peaks from pyritic sulfur. Finally COS and $SO_2$ peaks (organic and inorganic) are treated as background of $H_2S$ peaks and no effort was made to fit their evolutions.

Assuming that all of the aliphatic sulfur evolves at low temperature during the pyrolysis, the amount of the first organic sulfur peak was obtained from the direct measurements of coal aliphatic sulfur (Kelemen, et al., 1991; Huffman, et al., 1991). To verify this assumption, Figure II.A.5-9 compares the gaseous sulfur amount evolved under the first $SO_2$ peak group with the direct measurement of the sulfur forms in coal (Kelemen, et al., 1991; Huffman, et al., 1991). This gaseous sulfur amount was determined by the difference between the total sulfur evolved in the first peak group measured in this work and the tar sulfur as calculated with FG-DVC. For the 6 high rank coals, the amount of aliphatic sulfur matches well the gaseous sulfur amount in the first peak group in the range of experimental uncertainty. The difference for the Wyodak and Illinois #6 coals indicates contributions from other sulfur sources to the first peak group. Since the aromatic sulfur is quite stable, it is more likely that part of the pyritic sulfur decomposes at this temperature range for these two low rank coals. This low temperature pyrite decomposition was supported by a reaction pathway proposed by Khan where the pyrite reacts with hydrogen gas a temperatures as low as 230°C. The lack of this decomposition in high rank coals however is still not explained. Also unexplainable is the Zap lignite coal, for which the gaseous sulfur evolved in the first peak group is much less than the aliphatic sulfur amount.

As discussed previously, the second peak group corresponds to the pyritic sulfur decomposition. After the amount of sulfur in this peak group was determined from Figure II.A.5-3, it was found that the amount is lower than that of volatile pyritic sulfur which is 50% of the total pyritic sulfur, indicating that part of the pyritic sulfur decomposed is retained by the coal matrix. The retained pyritic sulfur is believed to evolve at higher temperature in the third peak group. Finally, the volatile aromatic sulfur is assumed to evolve in the third peak group and the amount was determined by matching the total amount of the volatile sulfur.

Although derivation of kinetic data needs at least three different heating rate experiments, this requirement is relaxed by the fact that the pre-exponential factors of the gas pools are all in the range of

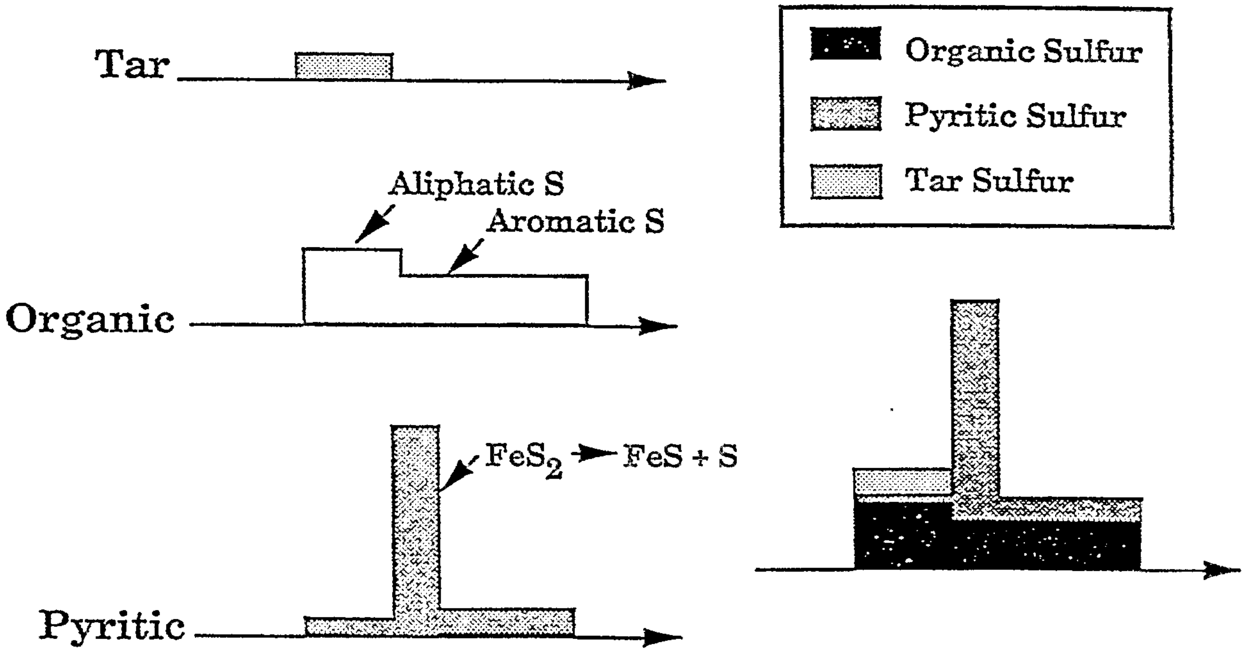

Figure II.A.5-8. Schematic Representation of the Proposed Component Peaks for Sulfur Evolution.

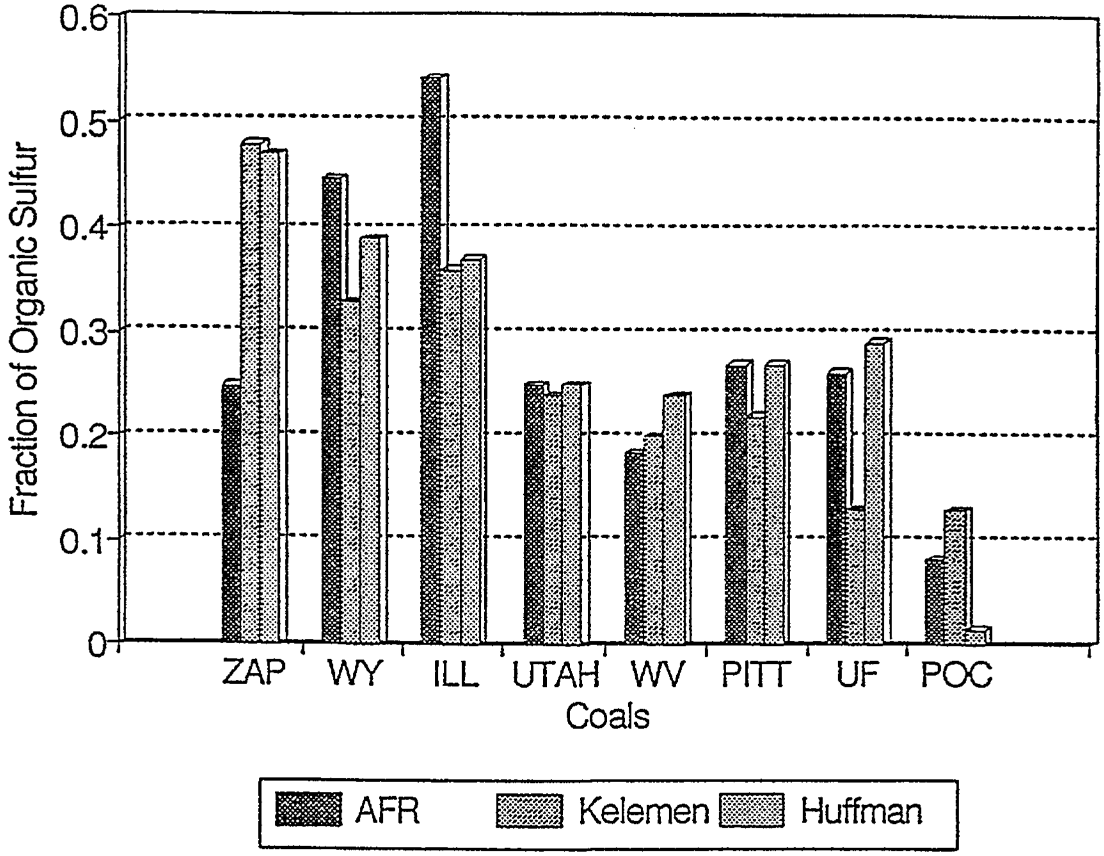

Figure II.A.5-9. Comparison of the Amount of the Sulfur Evolved under the First $SO_2$ Peak During Post Oxidized Pyrolysis and the Direct Measurements of the Aliphatic Sulfur. (Kleeman et. al., 1991 and Huffman et al., 1991)

$10^{12}$ to $10^{14}$ (Solomon, et al., 1993). Moreover, the distributed activation energy adopted in the FG-DVC model has the advantage that kinetic data derived at one heating rate can be used more reliably at other heating rates (Solomon, et al., 1993). Therefore, the same pre-exponential factor of $5\times10^{12}$ was used for all sulfur gas pools, and the activation energy and the $\sigma$ are the fitting kinetic parameters. The activation energy was chosen to match the peak evolution temperature, and the $\sigma$ was chosen to fit the shape of the evolution curve. More detail on FG-DVC gas kinetics can be found in Solomon, et al., (1988a and 1993).

A typical fit obtained by the procedure described above is given in Figure II.A.5-10 for Illinois #6 coal. The symbols are the TG-FTIR data points. The curves are the overall fit and the resolved component curves. For simplicity, the component curves plotted are the tar sulfur, organic sulfur and pyritic sulfur curves. Further division of these curves into individual species peaks would be too visually complicated. It is still quite clear in Fig. II.A.5-10 that the tar sulfur, the aliphatic sulfur and the pyritic sulfur decomposing at low temperatures constitute the first $SO_2$ peak group, while the pyritic sulfur is responsible primarily for the second peak group, and the aromatic sulfur and the rest of the volatile pyritic sulfur comprise the third peak group.

Figure II.A.5-11 displays the fractions of three types of organic sulfur for eight Argonne coals and Figure II.A.5-12 plots the fractions of four types of pyritic sulfur. As stated before, the organic sulfur is classified into three pools, among which the aliphatic is the least stable and evolves at low temperature while the nonvolatile aromatic sulfur is the most stable and dose not decompose in pyrolysis. There are three volatile and one non-volatile pyritic sulfur pools. The volatile pyritic sulfur results from the $FeS_2$ to FeS + S decomposition. The fate of the decomposed S from this reaction splits it into three volatile sulfur types. Most of the decomposed S evolves immediately in gaseous form and they constitute the intrinsic volatile pyrite peak. Part of the S from the $FeS_2$ decomposition would be retained in the coal matrix and is released at higher temperature. This results in the high temperature type of volatile pyritic sulfur. The low temperature pyritic sulfur would be due to the interaction between the coal matrix and pyrite which would de-stabilize the pyrite. Although Figures II.A.5-11 and II.A.5-12 show some information on the rank dependence of coal sulfur stability, it would be too speculative to draw further conclusions from the plots at this stage.

The sulfur pyrolysis evolution of eight Argonne coals are fitted with the FG-DVC and the sulfur model explained above, and the fits are plotted in Figure II.A.5-13. The pyrolysis evolution kinetic data for sulfur evolution from the Argonne coals are presented in Table II.A.5-1.

## Nitrogen Results and Discussion

The $NH_3$ and HCN evolutions from pyrolysis of the Argonne Premium coals are presented in Figures II.A.5-14 and II.A.5-15 respectively. The $NH_3$ evolution curves exhibit two main evolution peaks. For each peak, the $T_{max}$ increases with increasing rank, although the majority of the shift in $T_{max}$ for the high temperature $NH_3$ peak occurs between Wyodak and Illinois #6 coals. The HCN evolution curves exhibit only one main evolution peak. With the exception of Zap lignite and Wyodak coal, the HCN evolution curves overlay the high temperature $NH_3$ evolution peak suggesting that a common source is responsible for their formation. In the cases of Zap lignite and Wyodak coal, HCN evolves at a lower temperature than the high temperature $NH_3$ peak.

**Fraction of Volatile Nitrogen** - The fraction of nitrogen released from the Argonne Coals during pyrolysis displays rank dependance. In Figure II.A.5-16, the fraction of nitrogen evolved as HCN and $NH_3$ during pyrolysis is plotted as a function of oxygen content in the parent coal. There is a trend where the lower rank coals release a larger fraction of their nitrogen during pyrolysis as HCN and $NH_3$ than the higher rank coals.

**Heating Rate Dependence** - Table II.A.5-2 compares the TG-FTIR measured weight percents for $NH_3$ and HCN to previously obtained values generated during rapid heating rate pyrolysis in an entrained flow reactor (EFR) (Solomon, et al., 1982). Also included in this table are some data concerning the

Table II.A.5-1. Pyrolysis Evolution Kinetics of Sulfur Gases. The Frequency Factors Are $5.0\times10^{12}$ (1/seconds) for All the Pools. AE-- Activation Energy in Kelven. Sigma is in Kelven.

| | ZAP | WY | ILL | UTAH | WV | PITT | UF | POC |
|---|---|---|---|---|---|---|---|---|
| H2S-L | | | | | | | | |
| AE | 23500 | 23700 | 24300 | 24500 | 25300 | 25500 | 28000 | 27500 |
| Sigma | 1500 | 1000 | 1000 | 700 | 800 | 800 | 1000 | 1000 |
| $H_2S$-T | | | | | | | | |
| AE | 29000 | 28000 | 29500 | 31000 | 31000 | 30000 | 32000 | 34000 |
| Sigma | 3000 | 3000 | 2500 | 4000 | 4000 | 3000 | 2000 | 4000 |
| $SO_2$ | | | | | | | | |
| AE | 24000 | 24000 | 24000 | 24500 | 25000 | 25500 | 26000 | 26000 |
| Sigma | 1000 | 1000 | 1000 | 1000 | 1000 | 1000 | 1000 | 1000 |
| COS | | | | | | | | |
| AE | 24000 | 24000 | 24000 | 24500 | 25000 | 25500 | 26000 | 26000 |
| Sigma | 1000 | 1000 | 1000 | 1000 | 1000 | 1000 | 1000 | 1000 |
| $FeS_2$. low temp. decomp. | | | | | | | | |
| AE | - | 24000 | 23500 | - | - | - | - | - |
| Sigma | - | 4000 | 4000 | - | - | - | - | - |
| $FeS_2$, the intrinsic peak | | | | | | | | |
| AE | 27700 | 27700 | 28500 | 28500 | 28500 | 29300 | 29500 | 29500 |
| Sigma | 100 | 100 | 100 | 100 | 100 | 100 | 100 | 100 |

Table II.A.5-2. $NH_3$ and HCN Weight Percents from Pyrolysis in TG-FTIR and Entrained Flow Reactor

| | TG-FTIR | | | EFR 1100°C, 24" | | |
|---|---|---|---|---|---|---|
| | (DAF wt.%) | | Total Volatile Nitrogen Fraction | (DAF wt.%) | | Total Volatile Nitrogen Fraction |
| | HCN | $NH_3$ | | HCN | $NH_3$ | |
| Pocahontas | 0.036 | 0.07 | --- | 0.28 | 0 | 0.11 |
| Upper Freeport | 0.032 | 0.13 | --- | 0.78 | 0 | 0.26 |
| Pittsburgh | 0.043 | 0.16 | 0.31 | 0.84 | 0 | 0.27 |
| Stockton | 0.065 | 0.15 | --- | 0.55 | 0 | 0.18 |
| Utah Blind Canyon | 0.110 | 0.16 | --- | 1.21 | 0 | 0.40 |
| Illinois | 0.083 | 0.15 | 0.43 | --- | --- | --- |
| Wyodak | 0.049 | 0.11 | --- | 0.60 | 0 | 0.27 |
| Zap | 0.110 | 0.14 | --- | --- | --- | --- |

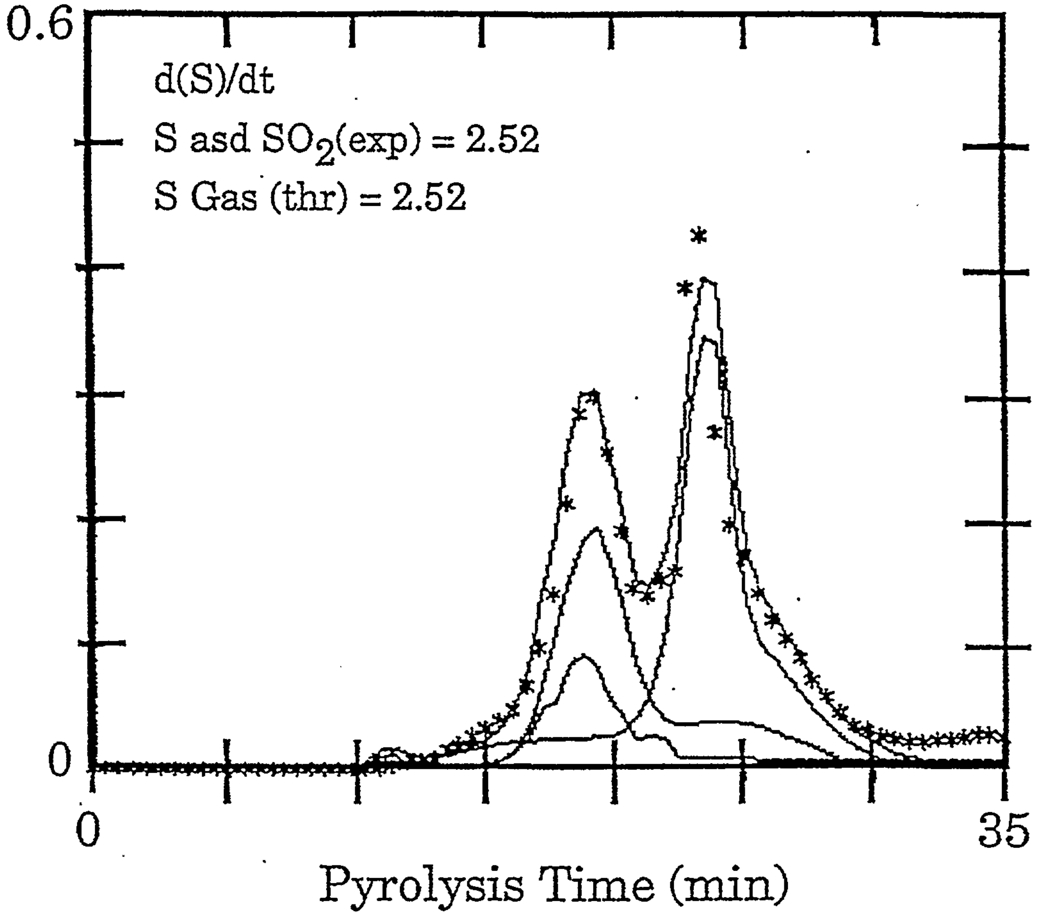

Figure II.A.5-10. Peak Resolutions of Sulfur Evolution for Illinois #6 Coal.

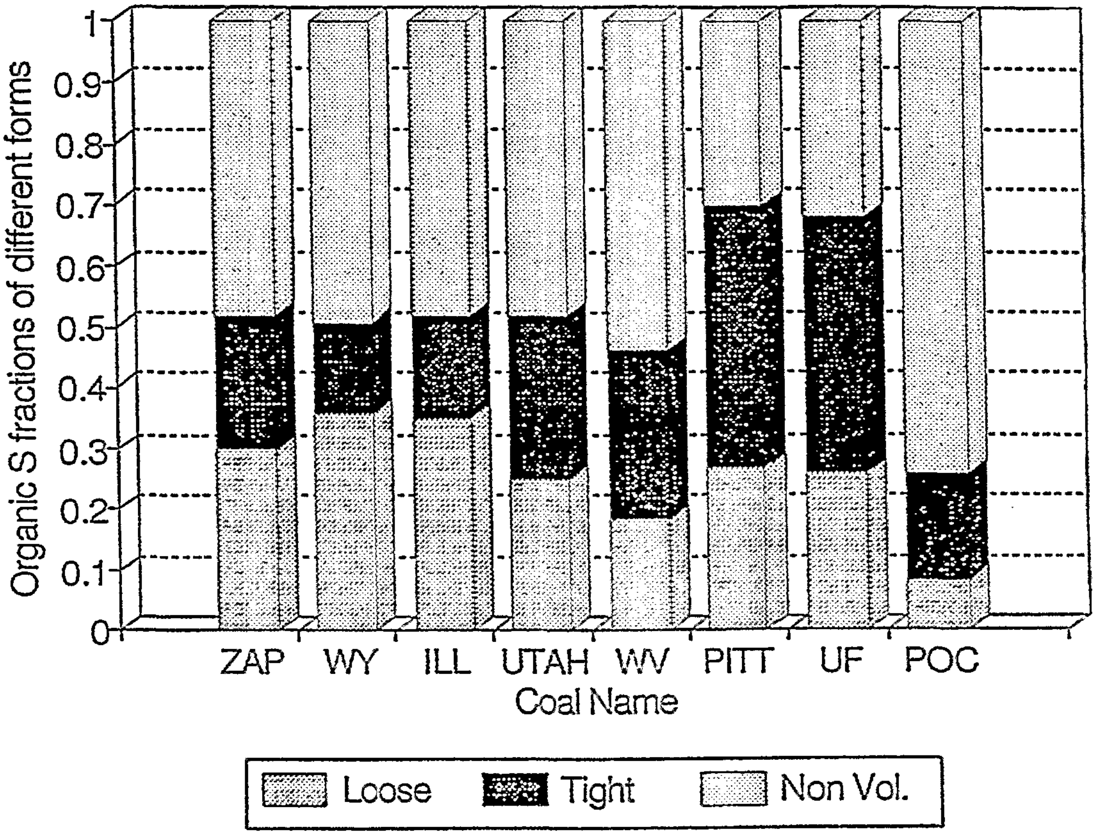

Figure II.A.5-11. Organic Sulfur Fractions of Different Forms for the Argonne Coals, Determined in this Work.

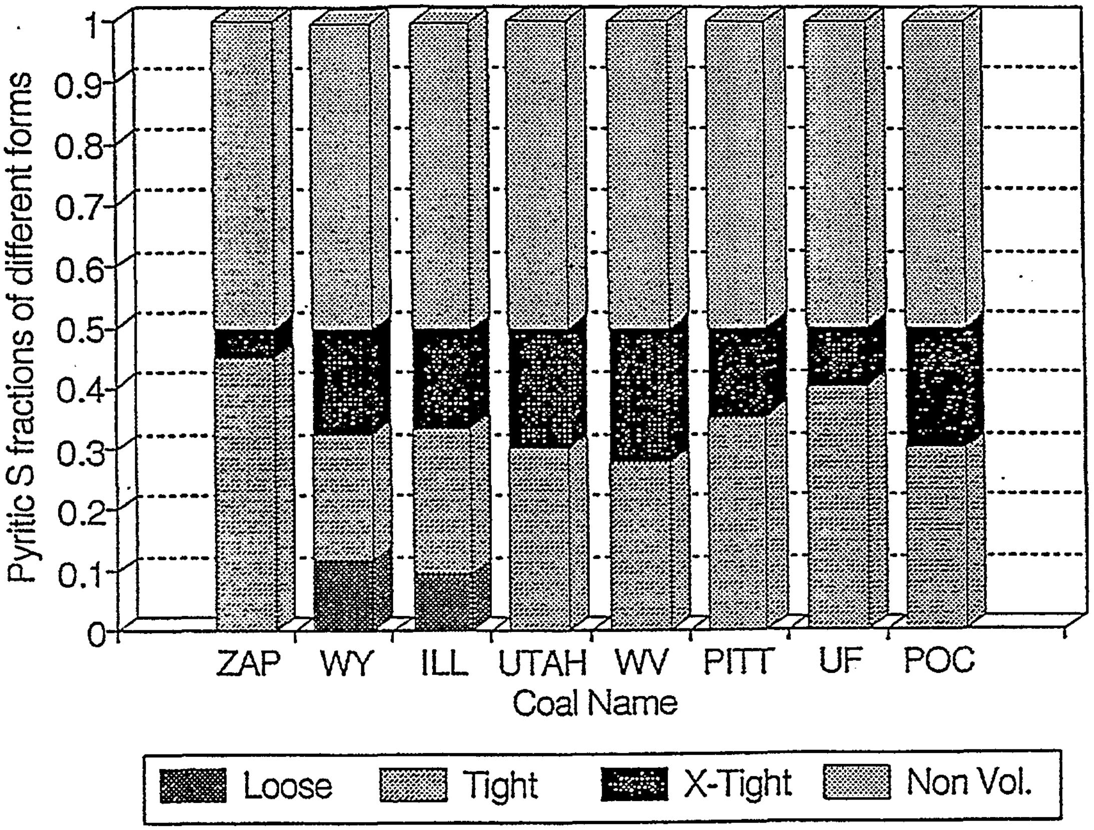

Figure II.A.5-12. Pyritic Sulfur Fractions of Different Forms for the Argonne Coals, Determined in this Work.

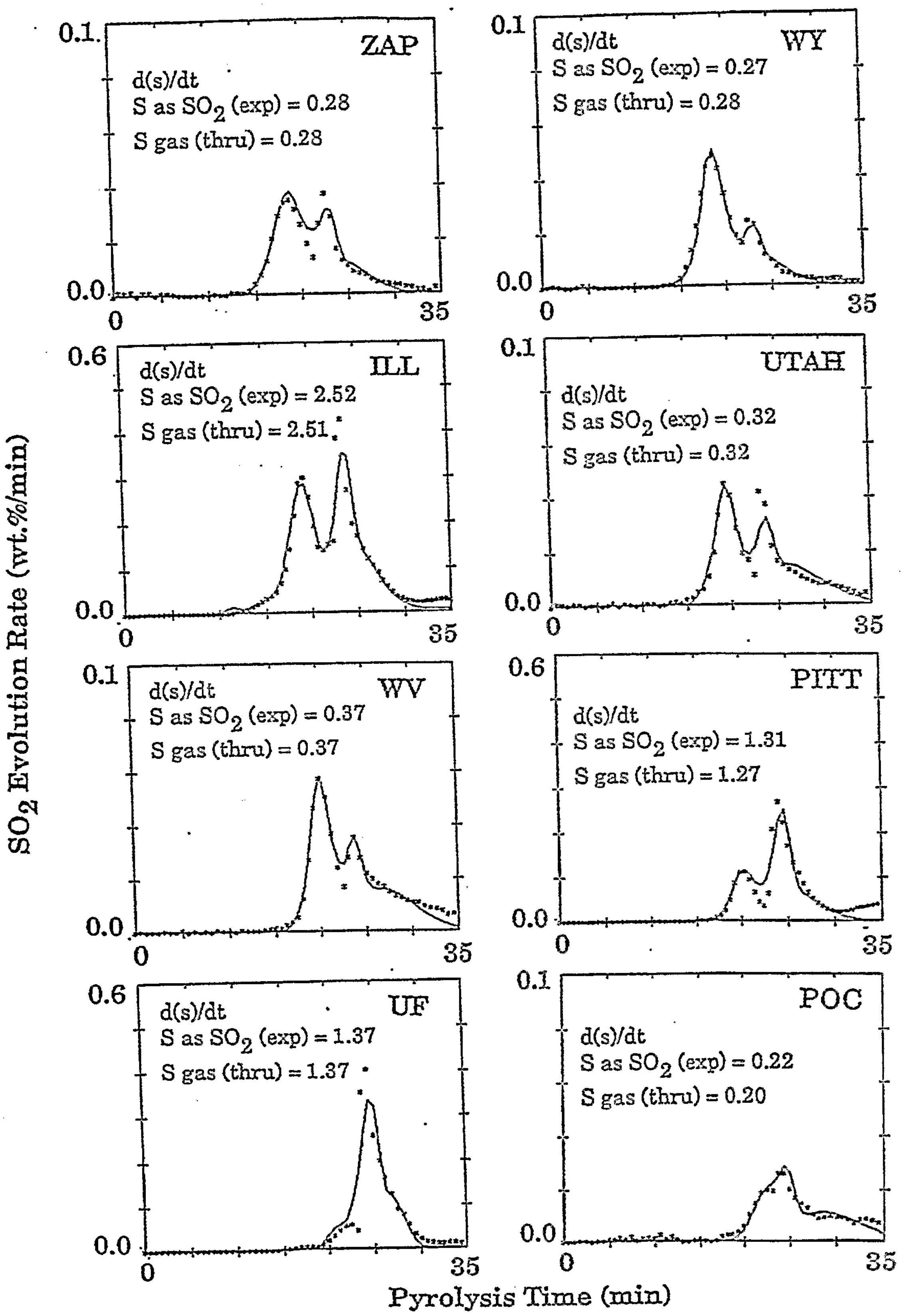

Figure II.A.5-13. $SO_2$ Evolution Curves Measured in Post Oxidized Pyrolysis (symbols), and the Fitted Curves by FG-DVC Model with Sulfur Evolution Kinetics Developed in this Work. Heating Rate is 30°C/sec.

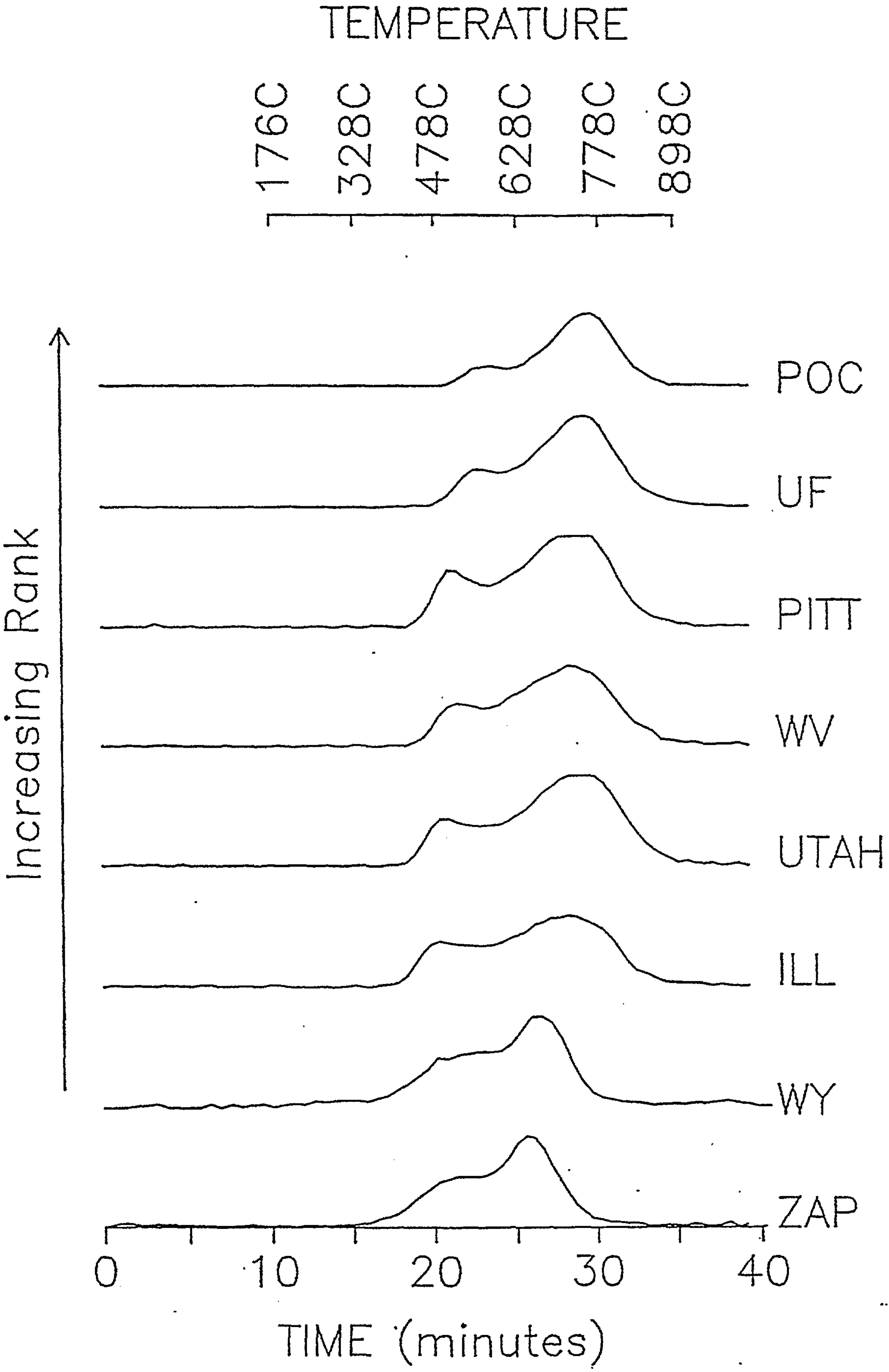

Figure II.A.5-14. $NH_3$ Evolution Curves from Pyrolysis of the Argonne Coals.

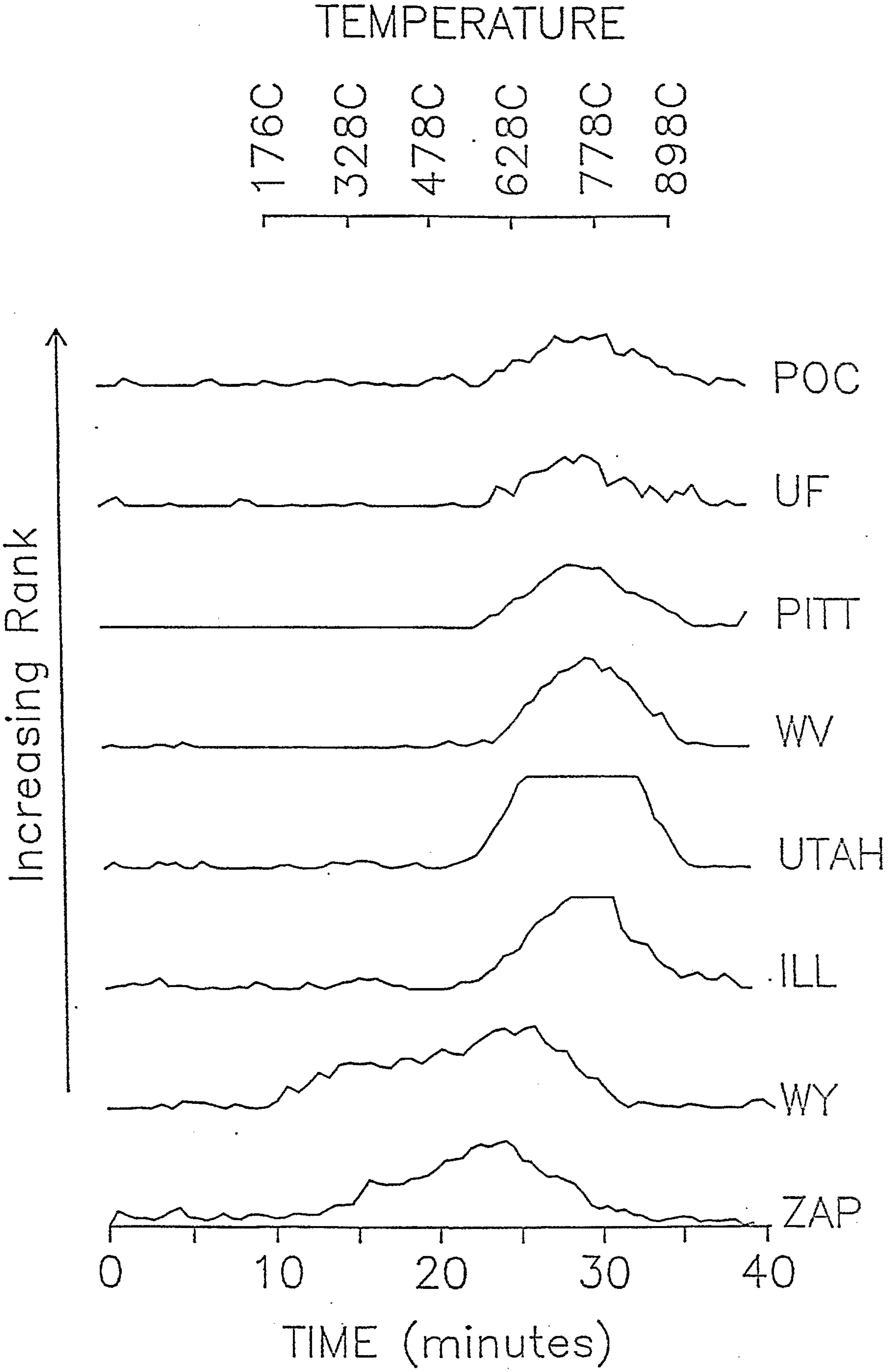

Figure II.A.5-15. HCN Evolution Curves from Pyrolysis of the Argonne Coals.

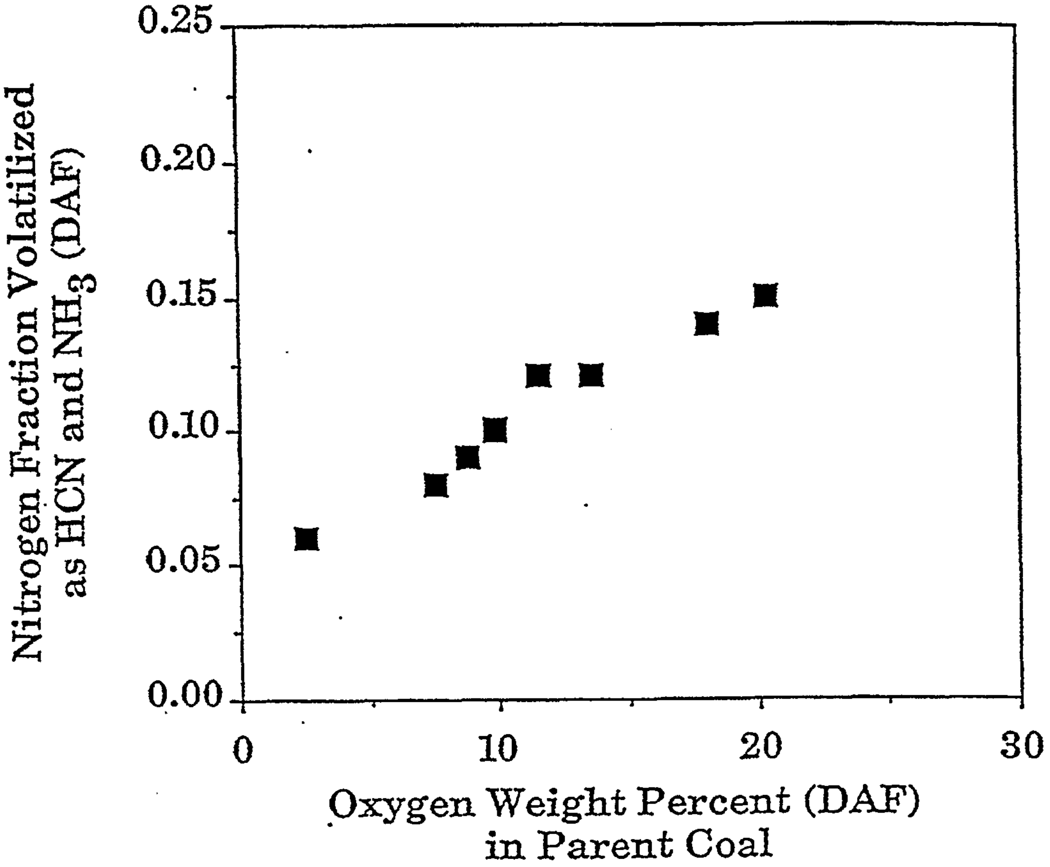

Figure II.A.5-16. Fraction of Nitrogen Evolved as $NH_3$ and HCN from the Argonne Coals During Pyrolysis in the TG-FTIR Plotted as a Function of Oxygen in the Parent Coal.

volatile nitrogen fractions inclusive of tar nitrogen for the two systems. The volatile nitrogen fraction data for the TG-FTIR is incomplete as only the Illinois #6 and Pittsburgh #6 coal tars were collected and subjected to nitrogen determination. Furthermore the tar nitrogen contribution in the TG-FTIR is overpredicted as the TG-FTIR apparatus includes paraffins and olefins in the tar amount. For the Pittsburgh #8 coal, the total amount of nitrogen evolved during pyrolysis in both experiments is similar. The ratio of HCN to $NH_3$, however, differs significantly. The dominant product during slow heating rate pyrolysis in the TG-FTIR is $NH_3$ while the only product during rapid pyrolysis in the EFR is HCN. Possible explanations for these results are as follows: 1) A secondary reaction process leads to the formation of $NH_3$ at the expense of HCN at low pyrolysis heating rates; 2) In the entrained flow reactor, secondary pyrolysis reactions, especially tar cracking, lead to the formation of HCN and the destruction of $NH_3$; 3) $NH_3$ is removed in the collection system of the entrained flow reactor (e.g., dissolution into water which condenses on the walls of the gas collection apparatus). Explanation #3 does not account for the order of magnitude difference in HCN weight percent in the two systems.

To test hypothesis #2, an experiment was preformed to increase the tar cracking in a slow heating rate pyrolysis run. Utah Blind Canyon coal was pyrolyzed in the TG-FTIR and the pyrolysis products were passed through a hot quartz tube heated to approximately 900°C just prior the gas analysis cell. This post pyrolysis method utilizes the same apparatus as the post oxidization method; however, helium is added to the sample stream rather than oxygen. The post pyrolysis results are presented in Figure II.A.5-17. Figure II.A.5-17a displays the HCN evolution curves while Figure II.A.5-17b shows the $NH_3$ evolution curves. In the post pyrolysis experiment, the HCN evolution peak at the 20 minute mark indicates an increase in tar cracking which resulted in a 0.04 weight percent increase in HCN. Although this is consistent with hypothesis #2, the 0.04 weight percent increase in HCN is not enough to account for the order of magnitude difference in the two systems. Furthermore post-pyrolysis did not show significant reductions in $NH_3$ evolution. These results suggest that hypothesis #1 is the most likely explanation.

## Nitrogen Modeling

What makes the nitrogen evolution difficult to model is the heating rate dependency discussed above. In the literature, most of the investigations of the coal nitrogen conversion to nitrogenous gases were conducted in the combustion conditions, which normally feature high heating rates, short coal particle residence time, and high temperature. Although the presence of oxygen produces NO and could alter the conversion pathways, a brief look at these results is worthwhile. In general, coal devolatilization produces more HCN than $NH_3$ for bituminous coals, while more $NH_3$ evolves in subbituminous coals and lignites (Chen, et al., 1982). In the cases where the time evolution profile were provided (Baumann, and Moller, 1991 and Usman Ghani and Wendt, 1990), it is observed that for coals of all ranks HCN evolves before the $NH_3$ gas evolution. Based on this observation, several investigators (Baumann, and Moller, 1991; Usman Ghani and Wendt, 1990; and Bose et al., 1988) suggested that $NH_3$ is produced in a secondary reaction involving the HCN gas, but it is not clear whether this reaction is in the gas or solid phase. Also, the source of the needed hydrogen atoms is unknown.

Baumann and Moller (1991) studied the coal nitrogen evolution during pyrolysis under fluidized bed combustor conditions for coals of a wide range of ranks. They discovered that HCN starts to evolve at lower temperature than does $NH_3$ for all the coals. With addition of small amount of oxygen, the $NH_3$ amount is reduced, because, as they explained, the hydrogen that was available for hydrogenation of HCN to form $NH_3$ is consumed by the formation of $H_2O$.

The importance of hydrogen in the conversion of the coal nitrogen to nitrogen gases was demonstrated by the studies of Mackie et. al., (1990 and 1991) which shows that the decomposition products of aromatic compounds containing nitrogen in heterocyclic structures do not include $NH_3$ at all. The model compounds differ from the coals in that they are pure aromatic and do not contain any aliphatic structure which has a large potential to donate hydrogen. The absence of $NH_3$ from the pyrolysis products of these compounds could thus be explained by the lack of donatable hydrogen atoms.

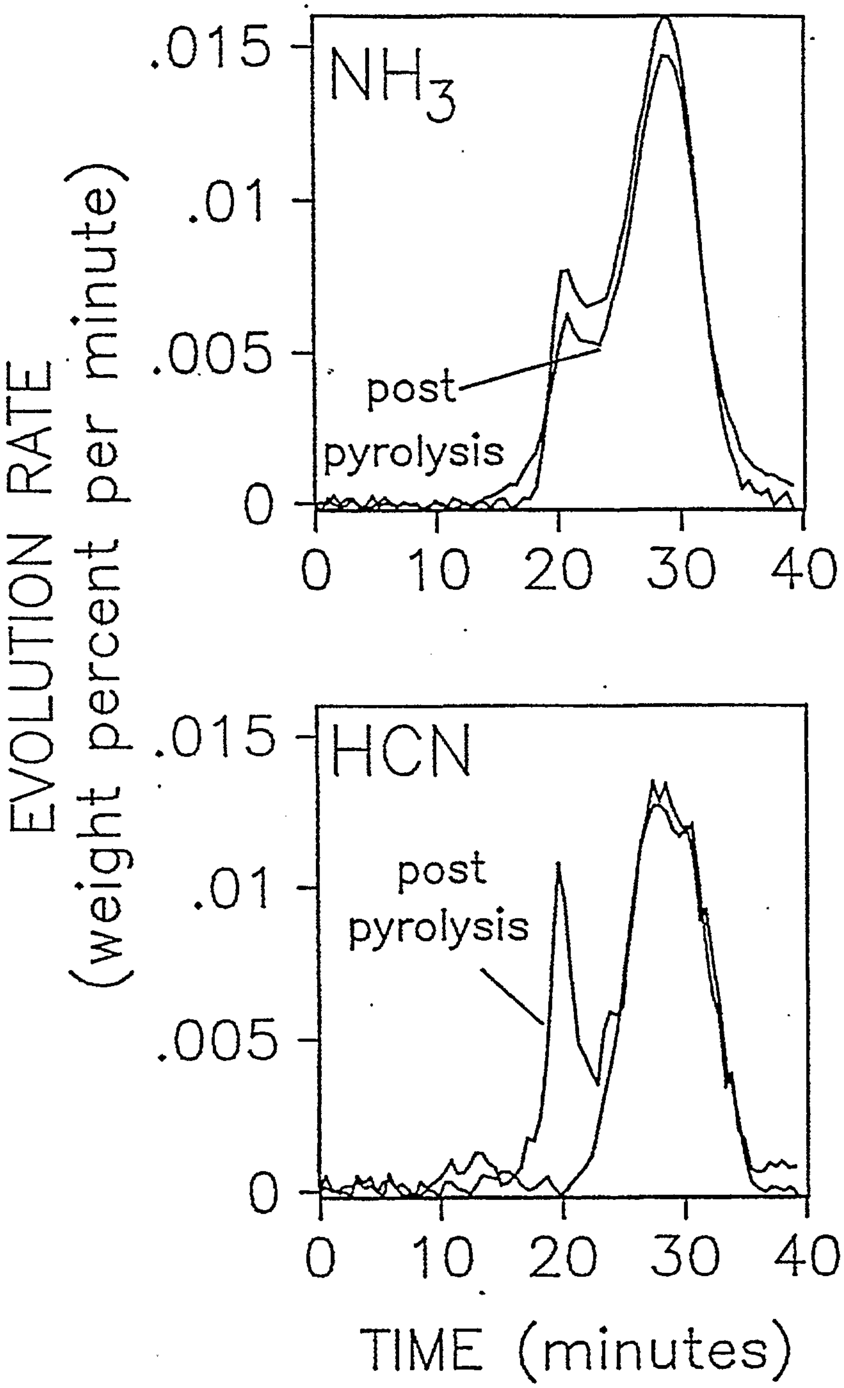

Figure II.A.5-17. $NH_3$ and HCN Evolution Curves from Pyrolysis and Post Pyrolysis of Utah Blind Canyon.

Although the existence of the secondary reaction that produces $NH_3$ from HCN seems apparent, the details of the reaction path have not been identified. In principle, this reaction could occur either in the gas or solid phase. If the HCN reacts with $H_2$ in the gas phase, the reaction kinetics ought to be coal rank independent and the gas phase reaction will only proceed with high enough rate when the reactants are sufficiently concentrated. In a study of modeling the nitrogenous gas productions during the fuel-rich combustion, Bose, et. al., (1988) found that the homogeneous gas reaction mechanism failed because the reaction kinetics seems to be coal rank dependent. Considering these arguments, the reaction of HCN with coal hydrogen is more probable.

One of the reasons for the heating rate dependence of the coal nitrogen evolution exhibited in our experimental results could be that the HCN to $NH_3$ conversion is depended on the length of the contact time between the evolving HCN gas and the coal or char solid. The pyrolysis gas leaves the coal particle more slowly at low heating rate than at high heating rate, allowing enough time for the HCN and coal or char hydrogen to react. The other limiting factor is the availability of the donatable coal hydrogen since hydrogen is needed to convert HCN to $NH_3$. As the tar cracking at high temperatures consumes more hydrogen, the completeness of this conversion could be reduced due to the deficit of hydrogen at this condition. FG-DVC needs to be further refined in the direction of hydrogen evolution and tar cracking before we can describe the effect of the hydrogen availability on the nitrogen evolution.

Three possible mechanisms for HCN and $NH_3$ formation are plotted in Figure II.A.5-18. Based on the above discussion we have chosen mechanism b. HCN evolves directly from its pool precursors. $NH_3$ gas comes from two sources: the direct evolution from coal nitrogen (pools) and the secondary conversion from evolved gaseous HCN to $NH_3$. The former contributes only a small amount, while the later is the major reaction pathway. The conversion is assumed via the reaction of the gaseous HCN with the coal hydrogen in the pore structure of coals. The completeness of this reaction is obviously dependant upon the HCN to $NH_3$ conversion rate, the gas residence time in the pore structure, the coal reaction residence time in reactors, and the coal devolatilization rate. For a constant conversion rate, the longer the gas residence time in the pore, the higher the conversion fraction. This residence time is highly dependent on the pyrolysis or combustion conditions. A high coal devolatilization rate sweeps the gas out of the coal particle very quickly, leading to a very short gas residence time in coal. In general, a longer gas-coal contact time could be expected in fluidized-bed and fixed-bed conditions than in a drop tube or an entrained flow reactor, since in a fluidized-bed the gas continuously maintains contact with other coal particles after it leaves its parent coal particles. In other words, more conversion could occur in the former conditions than in the later.

Since nitrogen evolves at higher temperatures than other gases, the gas residence time depends on the char structure instead of the coal structure. The precise determination of the gas residence time is difficult as the char structure is a complicated function of the pyrolysis process. It can be more complicated if bed conditions can affect the gas conversion reactions.

This model uses a simplified single cell structure to estimate the gas residence time. Consider a spherical coal particle with an original radius $r_0$. The radius changes to $r_2$ in the pyrolysis due to the weight loss and swelling. The particle has a single inner bubble of radius $r_1$. During pyrolysis, the evolution gas flux in this particle is always positively outward. At a point inside this particle of distance r from the origin of the sphere, the residence time, $\Delta t_n$, of the evolution gas before leaving the particle is

$$\Delta t_n(r) = \Delta t_{n0} \ln \frac{r_2}{r} \qquad \text{(II.A.5-1)}$$

and

$$\Delta t_{n0} = \frac{3P^* \phi_v}{\rho n_{tc} RT} \qquad \text{(II.A.5-2)}$$

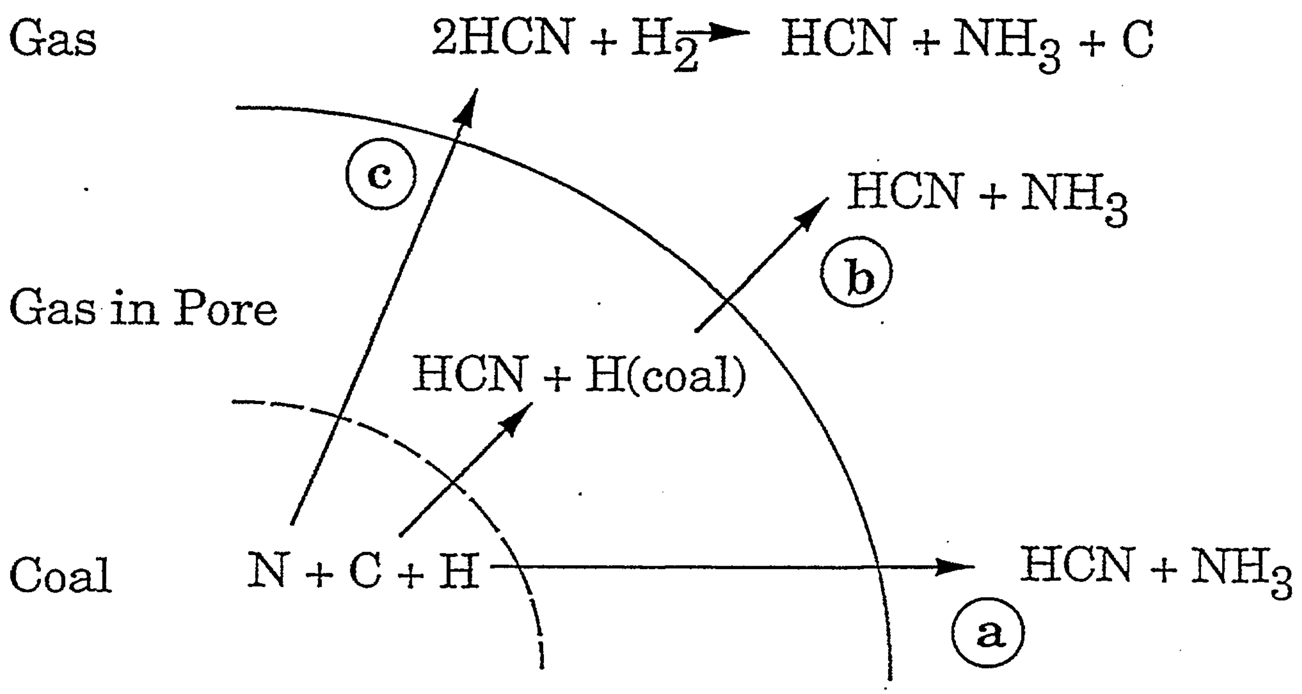

Figure II.A.5-18. Three Possible Mechanisms of HCN and $NH_3$ Evolution.

where $P^*$ is the gas pressure in the coal pores, $n_{tot}$ is the total gas evolution rate per unit weight coal, R is the gas constant, T is the temperature, $\rho$ is the coal solid density, and $\phi_v$ is the volume swelling ratio that can be calculated by a swelling model (Users Guide, 1992). The HCN gas that is generated within the shell $4\pi r^2 dr$ has a time period of $\Delta t_n$ to react to $NH_3$. The modified HCN evolution rate is then

$$\frac{dW^*_{HCN}(gas)}{dt}\Big|_r=\frac{dW_{HCN}(gas)}{dt}e^{(-k_n\Delta t_{n0}\ln(\frac{r_2}{r}))} \qquad \text{(II.A.5-3)}$$

where $k_n$ is the reaction constant of HCN to $NH_3$ conversion, and $dW_{HCN}(gas)/dt$ is the HCN evolution rate given by FG-DVC gas evolution equation

$$\frac{dW_{HCN}(gas)}{dt}=k_{HCN}W_{HCN}(char) \qquad \text{(II.A.5-4)}$$

Averaging over the whole particle leads to

$$\frac{dW^*_{HCN}(gas)}{dt}=f_n\frac{dW_{HCN}(gas)}{dt} \qquad \text{(II.A.5-5)}$$

where

$$f_n=(1-f_{n0})\frac{1-e^{(-k_n\Delta t_{n0}\ln(\frac{r_2}{r_1}))}(r_1/r_2)^3}{(1-(r_1/r_2)^3)(1+k_n\Delta t_{n0}/3)}+f_{n0} \qquad \text{(II.A.5-6)}$$

where $f_{n0}$ is a non-zero residue fraction of HCN rate. $(1-f_n)$ is the HCN to $NH_3$ conversion factor. And

$$\frac{dW^*_{NH_3}(gas)}{dt}=\frac{M_{NH_3}}{M_{HCN}}(1-f_n)\frac{dW_{HCN}(gas)}{dt} \qquad \text{(II.A.5-7)}$$

where $M_{HCN}$ and $M_{NH_3}$ are the molecular weights of HCN and $NH_3$, respectively.

To extend this single cell structure model to the generally heterogeneous coal/char structure, the residue HCN rate fraction, $f_{n0}$, the coal volume swelling ratio, $\phi_v$, and coal particle-bubble radius ratio, $r_1/r_2$, are the model parameters.

A non zero $f_{n0}$ is employed to retain a small fraction of HCN after the most of it has been converted to $NH_3$, even at very low heating rate. $f_{n0}$ is affected by the char particle size and the char structure, which in turn are affected by the heating rate. $f_{n0}$ is also a function of reaction bed conditions that could alter $\Delta t_n$ evaluated above by affecting the length of the evolution gas/particle contact time. The model suggested $f_{n0}$ value is 0.1. It is only important for low heating rate, while for very high heating rate cases in which the conversion has no time to complete, $f_{n0}$ is not important.

Although the char volume swelling ratio, $\phi_v$, and the ratio of the inner bubble size to the char particle size, $r_1/r_2$, can be calculated directly from the swelling model, (Users Guide, 1992) we would rather treat them as model parameters, because the single cell swelling model (Users Guide, 1992) is too primitive to describe the heterogeneity of the char structure. For most of the combustion cases, swelling is not significant due to the very high heating rate and the presence of oxygen. Therefore, $\phi_v$ is set to 4 and $r_1/r_2$ to 0.8.

By fitting our experimental data of the pyrolysis nitrogen gas evolutions, the coal nitrogen gas evolution kinetics were obtained in the same way as for the C, H and O volatile species (Solomon, et al., 1988a; 1990a; and 1993), and are listed in Table II.A.5-3. Figure II.A.5-19 shows the experimental evolutions and model predictions of HCN and $NH_3$ for Stockton Seam coal: (a and b) at 30°C/min and (c and d) during high heating rate pyrolysis in an entrained flow reactor of furnace temperature 1100°C. As shown, our model maintains reasonable agreement consistently with nitrogen evolution data at both low and high heating rates. The time evolution curves of HCN and $NH_3$ in the entrained flow reactor are not available due to the extremely high heating rate. The comparison is then made on the ultimate yields of these two gases in this case. As mention above in the Results Section, the experimental $NH_3$ value in the EFR may be too low because $NH_3$ is being removed from the system prior to the gas analysis.

Recently Nelson, et al. (1992) published their experimental results on the splitting of coal nitrogen into HCN and NH3 in a fluidized bed condition. The yields of these two nitrogen gases have very interesting temperature dependence. Our model was used to model the nitrogen evolution under the conditions given by Nelson, et al. The model prediction compares reasonably well with the data (Nelson et al., 1992), as displayed in Figure II.A.5-20. The basic trends of the gas yields are correctly predicted and, most importantly, the predicted transition temperature at which the yield of $NH_3$ starts to decline is in good agreement of the data (Nelson, et al., 1992).

## Summary and Conclusions

The total $SO_2$ evolution from the Argonne Premium Coals during pyrolysis measured by post oxidation of volatile products demonstrated two main peaks and one small high temperature peak. These overall evolution peaks are composed of several component peaks that are formed by the different forms of sulfur existing in coals. By applying the FG-DVC model and literatures data and suggested mechanisms, these peaks were resolved and the evolution sequences of coal sulfur of all forms were identified. The experimental data coupled with the FG-DVC model offered the following conclusions: the first $SO_2$ peak was from aliphatic sulfur and possibly pyrite in Wyodak and Illinois #6 coals. The second peak was primarily pyrite and the third peak was aromatic sulfur and small amounts of pyrite. The evolution kinetics of coal sulfur of all forms were obtained and incorporated in FG-DVC.

$NH_3$ evolutions exhibited two main evolution peaks whose $T_{max}$'s showed rank dependence. HCN evolution curves coincided with the high temperature $NH_3$ evolution curves except in the cases of Wyodak coal and Zap lignite. At low heating rates, $NH_3$ is the dominant product while during rapid heating rate pyrolysis HCN was the only product. The main pathway to $NH_3$ formation is believed to be from the secondary reaction of gaseous HCN with coal hydrogen in the pores of coal. A model was developed that describes the direct evolution of HCN and the secondary reaction to form $NH_3$. The effects of heating rate and the char structure on the relative abundance of pyrolysis HCN and $NH_3$ gases were considered. This model provides consistent agreement between the prediction and experiment data on the HCN and $NH_3$ evolutions at both low and high heating rates.

## II.A.6. Optical Properties of Char

### Emissivities

In gasification, the determination of spectral emittance is important for two reasons. First, knowledge of the spectral emittance is necessary for the measurement of particle temperatures. Second, the spectral emittance or the emissivity (the average emittance over wavelength) must be known to

Table II.A.5-3. Pyrolysis Evolution Kinetics of Nitrogen Gases. The Frequency Factors Are $5.0 \times 10^{12}$ (1/seconds) for All the Pools. AE-- Activation Energy in Kelven. Sigma is in Kelven.

| | ZAP | WY | ILL | UTAH | WV | PITT | UF | POC |
|---|---|---|---|---|---|---|---|---|
| HCN-L | | | | | | | | |
| AE | 24000 | 25000 | 26000 | 26000 | 26000 | 26000 | 26000 | 26000 |
| Sigma | 3000 | 3000 | 3000 | 3000 | 3000 | 3000 | 3000 | 3000 |
| HCN-T | | | | | | | | |
| AE | 31000 | 32000 | 34000 | 36000 | 34000 | 34000 | 35000 | 35000 |
| Sigma | 2500 | 2000 | 3000 | 3000 | 2500 | 2500 | 2500 | 2200 |
| $NH_3$-L | | | | | | | | |
| AE | 25000 | 26000 | 26000 | 26500 | 26500 | 27000 | 27300 | 27700 |
| Sigma | 1500 | 1500 | 1500 | 1500 | 1500 | 1200 | 1500 | 1500 |
| HCN to $NH_3$ conv. | | | | | | | | |
| AE | 15000 | 15000 | 15000 | 15000 | 15000 | 15000 | 15000 | 15000 |
| Sigma | 3000 | 3000 | 3000 | 3000 | 3000 | 3000 | 3000 | 3000 |

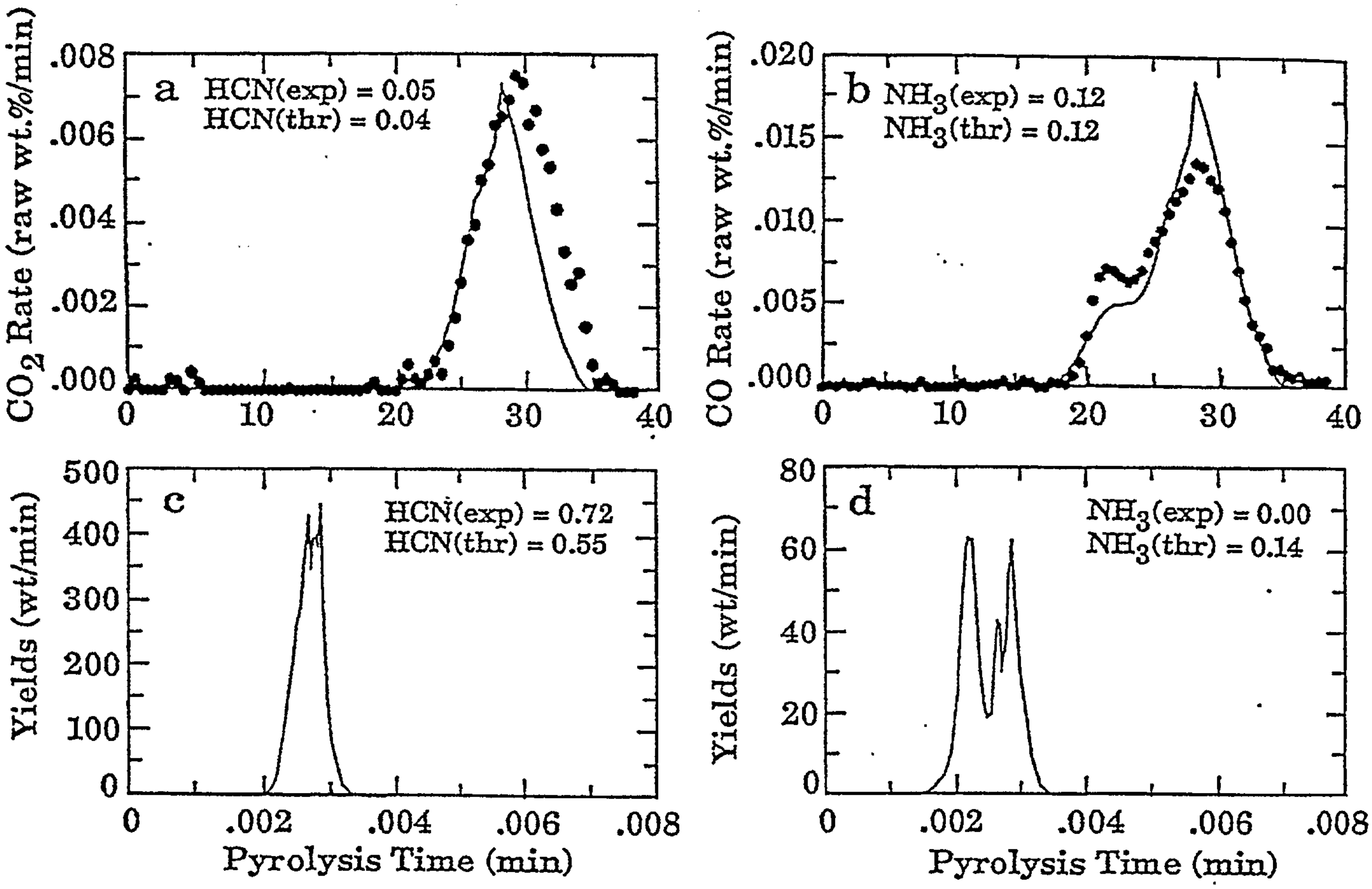

Figure II.A.5-19. a) and b) HCN and $NH_3$ Evolution Curves at 30°C/min, the Experimental Data (symbols) and the Fitted curves by FG-DVC. c) and d) Comparison of the 1100°C Entrained Flow Reactor Experimental Data and the FG-DVC Model Predictions.

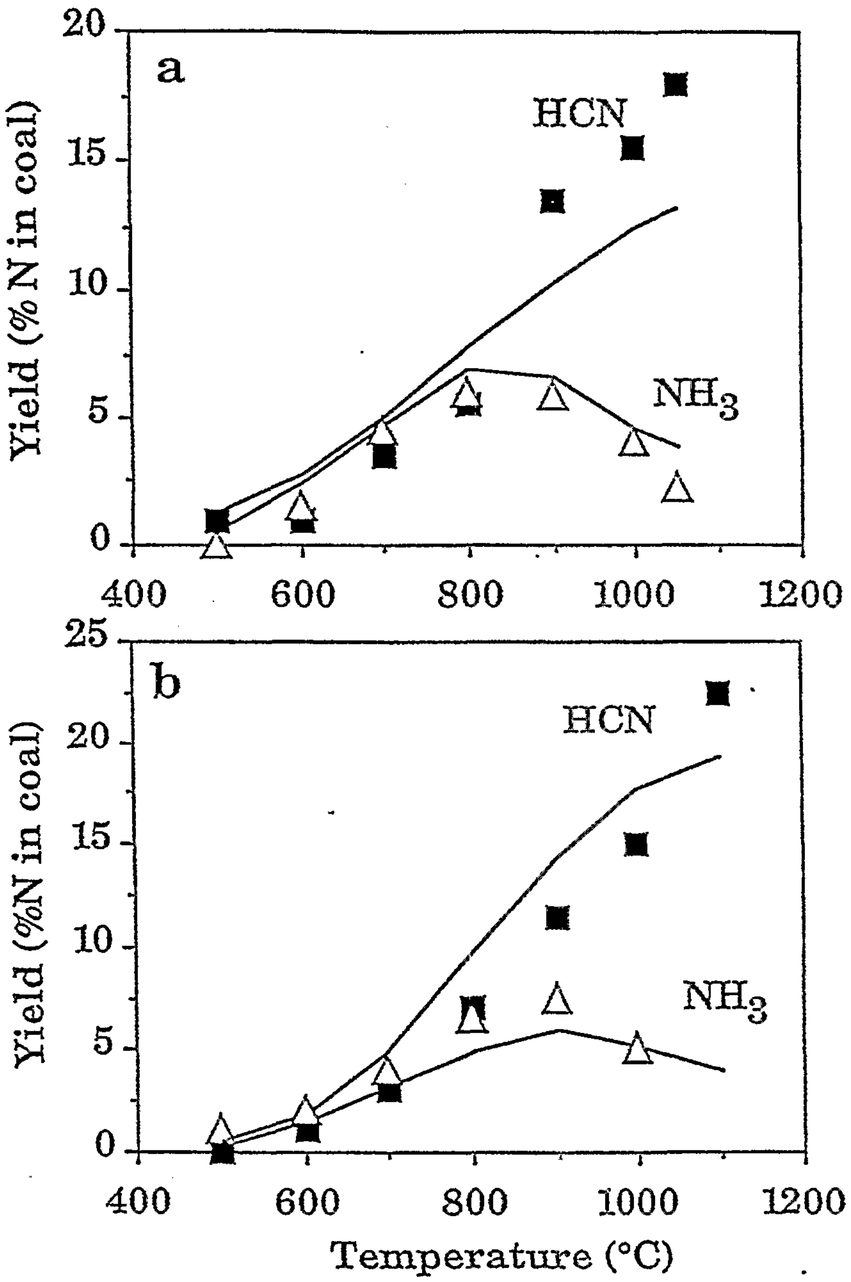

Figure II.A.5-20. Comparison of Model Predictions and Experimental Data (Nelson et al., 1992) for two Australian Coals: a) Yalloum and b) Blair. Lines-Prediction; Symbols-Data.

calculate the rate of particle heat up, and the power radiated by the particle during combustion.

We have recently developed a new method for on-line, in-situ monitoring of particle streams to determine their spectral emittance, chemical composition, size, and temperature (Best, et al., 1986; Solomon, et al., 1985a; Best, et al., 1984; Solomon, et al., 1986a; 1986b; 1986c; and 1987a). The technique uses a Fourier Transform Infrared (FT-IR) spectrometer to perform both emission and transmission (E/T) spectroscopy for a stream of gas suspended particles.

The technique has been applied to measure spectral emittance of coal. Measurements on a variety of samples show that coal of pulverized particle size is not gray, having values of emittance near 0.9 for some regions of the spectrum, but values substantially less than 0.9 in many regions. The spectral emittance is dependent on rank, particle size, and the extent of pyrolysis, approaching a gray-body for chars, anthracite, and large particles. Recent measurements (Solomon, et al., 1987a) show that pulverized coal particles of the size used in entrained gasification undergo a transition from highly non-gray coal to highly gray char ($\epsilon \approx 0.9$), and finally to moderately gray char ($\epsilon = 0.7$ to 0.8). An example of the non-gray to gary transition is illustrated in Fig. II.A.6-1 which shows the radiance per unit surface area from char particles. Here a gray-body with $\epsilon = 0.9$ would emit at the theoretical lines marked BB (883), etc. The char is least gray at low temperatures, but increase in grayness as the temperatures (and exposure time) increases.

To provide understanding of this process and to develop a predictive theory for the emissivity as a function of particle size, rank and extent of pyrolysis, a theoretical analysis has been performed of emissivity during the coal to char transformation. Emissivities were calculated using the frequency dependent complex index of refraction, $m_\nu = n_\nu - ik_\nu$, from the standard equations of electromagnetic theory. For spherical particles these calculations can be performed using Mie theory (Bohren and Huffman, 1983).

The property of coal which determines its non-gray behavior and its variations with rank is primarily the imaginary part of the index of refraction, $k_\nu$. As discussed in (Solomon, et al., 1986b; 1986d; and Solomon, 1987a), $n_\nu$ and $k_\nu$ can be determined from the infrared spectra of coal and chars prepared in both KBr and CsI pellets. In Fig. II.A.6-2 are KBr pellet spectra recorded for chars of a Zap North Dakota lignite in differing states of pyrolysis, formed in the heated tube reactor (Best, et al., 1986) at an asymptotic tube temperature of 800°C. The 1200 to 1600 $cm^{-1}$ region is one in which scattering is small in the pellet spectra, so the absorption coefficient can be accurately determined from these data. At higher frequencies (wavenumbers) the determination is less accurate when only KBr pellet spectra are employed, and in this case only provide rough estimates of k.

In Fig. II.A.6-3 we have plotted (open circles) an average value of k in the 1200 to 1600 $cm^{-1}$ region measured from the char spectra (Fig. II.A.6-2), as a function of distance, D, traveled in the tube reactor. Here, the extent of pyrolysis increases monotonically with increase in D. Also plotted is the value for k at 2000 wavenumbers (closed circle in Fig. II.A.6-3a) and k at the absorbance minimum near 1500 $cm^{-1}$ (squares).

Taking a constant value of 1.6 for the real part of the index of refraction, n, we have used the Mie theory program (Bohren and Huffman, 1983) to calculate the emittance of particles of different size, and different k values (Fig. II.A.6-3b).

Using Figs. II.A.6-3a and II.A.6-3b it can be seen that for all states of pyrolysis, the value of k determined for the chars in the region between 1200 and 1600 $cm^{-1}$ are such that the value of the emittance, $\epsilon_\nu$, is constant and is within 10% of 1.05 for particle diameter, d, greater than 20 $\mu$m. The actual value depends slightly on particle size, but is practically independent of pyrolysis state. This is the region which has been used for temperature measurements.

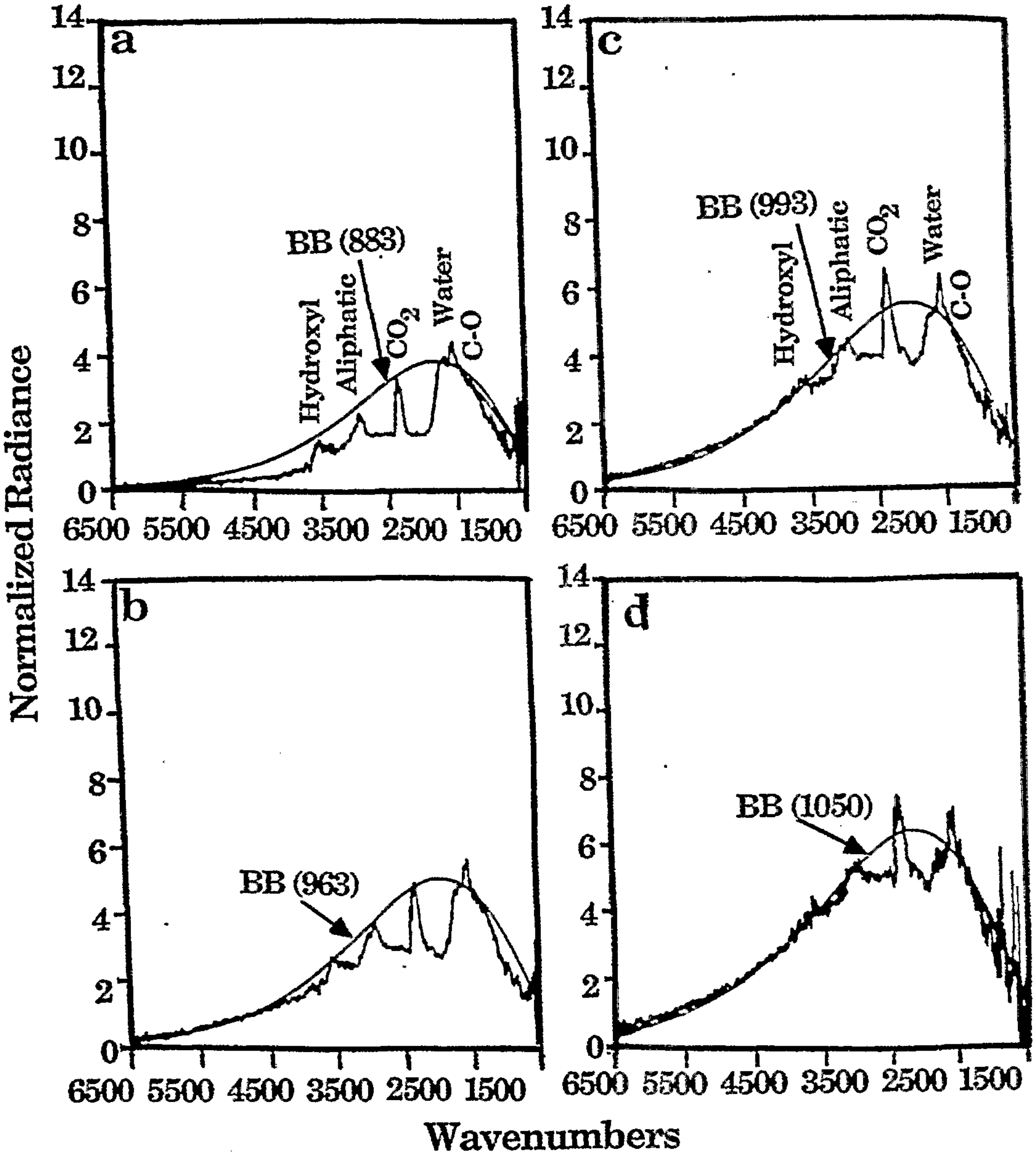

**Figure II.A.6-1.** Comparison of Normalized Radiance with Theoretical Grey-body Curves ( $\varepsilon = 0.9$) for Chars at Increasing Extents of Pyrolysis (200x325 mesh).

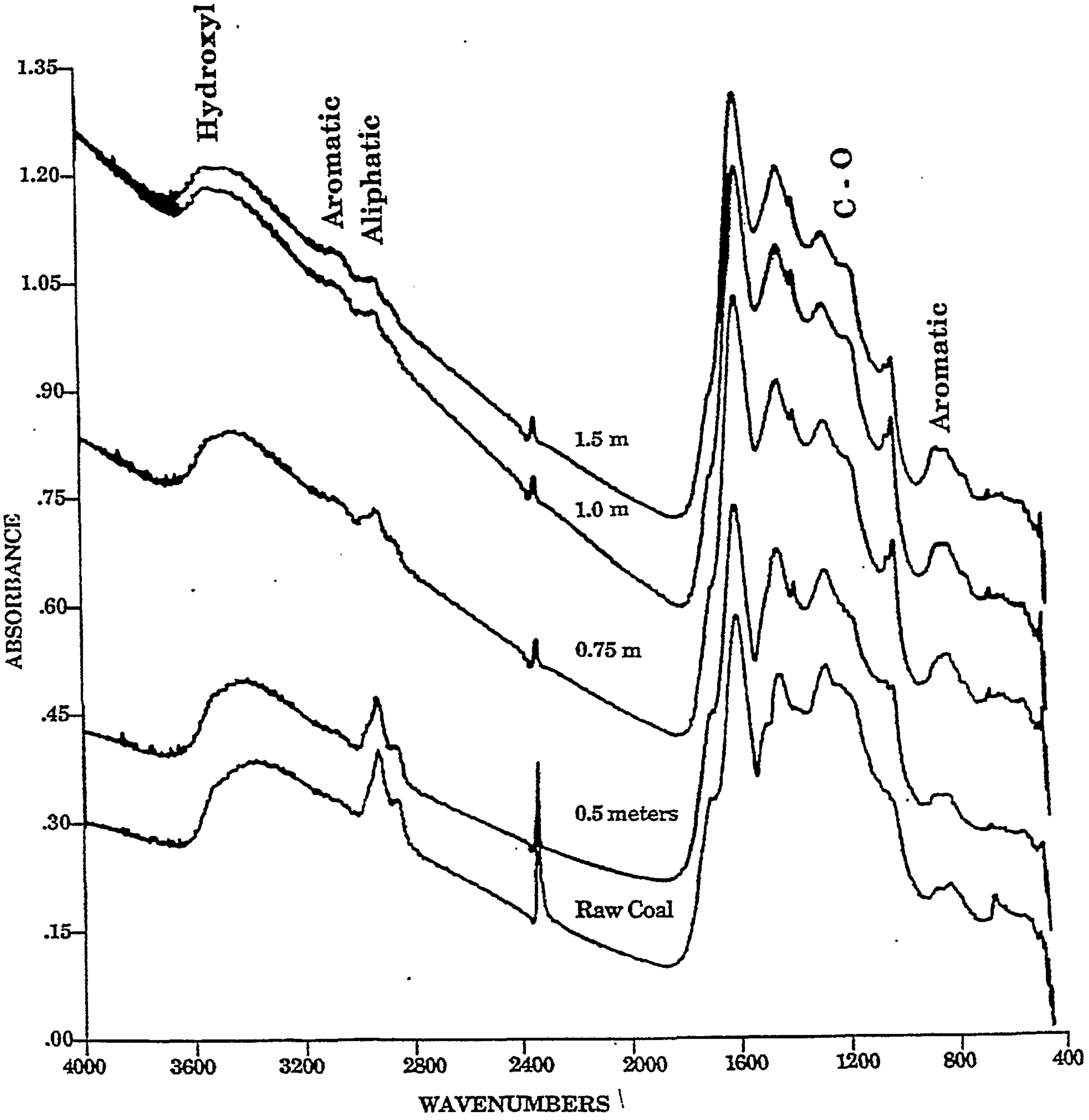

**Figure II.A.6-2.** Absorbance Spectra of Coal and Char in KBr-Pellets, as a Function of Distance in the Furnace at 800°C.

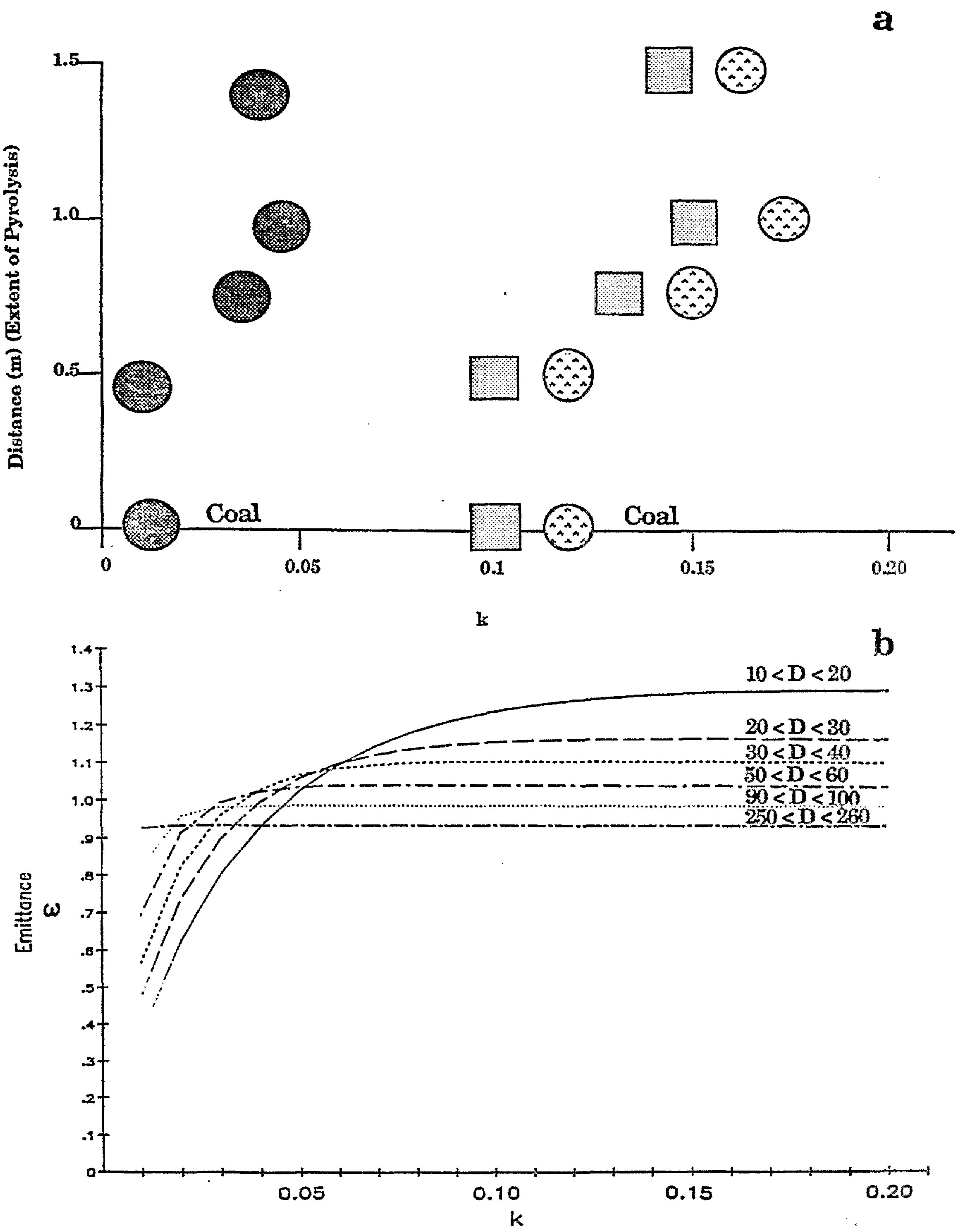

**Figure II.A.6-3.** a) Average Value of k in the 1200 to 1600 $cm^{-1}$ Region Measured from the Char Spectra of Figure II.A.6-2, as a Function of Distanced Traveled in the Tube Reactor (open circles): Value of k at the Absorbance Minimum Between 1200 and 1600 $cm^{-1}$ (squares): k for the Raw Lignite at 2000 $cm^{-1}$ (closed circles): b) Calculated Emittance as a Function of k, for Spheres of Various Diameters, with n = 1.6.

At 2000 $cm^{-1}$ the values of $\epsilon_v$ for coals are particle size dependent and significantly less than unity for small particle sizes. As can be seen in Fig. II.A.6-3b, an increase in k with extent of pyrolysis will affect $\epsilon_v$ at 2000 $cm^{-1}$. The estimated values of k at 2000 $cm^{-1}$ for the chars of Fig. II.A.6-2 suggest that $\epsilon_v$ for a 50 micron particle increases from 0.6 to 0.7 to a value of 1.0 during pyrolysis. This is in reasonable agreement with the observed emittance in Fig. II.A.6-1 which are for comparable conditions to those for which the chars were obtained.

There is a stage in pyrolysis beyond which $\epsilon_v$ in the 1200 to 1600 $cm^{-1}$ regions starts to vary. This occurs when the coal starts to graphitize and both the real and imaginary parts of the complex index of refraction ($m_v = n_v + ik_v$) start to increase. In Fig. II.A.6-4 we display contour plots of emittance in the n-k plane for 55 $\mu$m diameter spheres. That part of the figure which contains the n and k values appropriate to coals in the infrared region of the spectrum is cross-hatched, on the left hand side of the figure. The region for graphite is cross-hatched on the upper right hand side of the figure. During pyrolysis, the emittance in the 1200 to 1600 $cm^{-1}$ region (where $k \approx 0.1$) drops from a value greater than 1, towards the value for graphite. In other regions of the spectrum where k = 0.01, $\epsilon_v$ first increases and then decreases as k increase i. Our experimental observations suggest that for residence time on the order of 1 sec, n and k increase significantly only above 1000°C, and it is above this temperature that $\epsilon_v$ is observed to decrease. For a highly graphitized char $\epsilon_v$ can be as low as 0.7.

Besides the calculation of the emissivity, the Mie theory program can be used to calculate the total extinction cross section $F^t_v$. $F^t_v$ determines the shape of the transmittance, $\tau_v$ where N, A, and L are the particle number density, particle area, and path length through the particle stream, respectively.

$$\tau_v = \exp(-NA\,F_v^t L) \qquad \text{(II.A.6-1)}$$

Some calculations of $F^t_v$ are presented in Fig. II.A.6-5. In Fig. II.A.6-5a we show calculations of $F^t_v$ for a Nicolet 7199 FT-IR, using the optical constants we have derived for a Montana subbituminous coal (Solomon, et al., 1986d). The Nicolet 7199 FT-IR spectrometer, with a 4" diameter, 9.5" focal length collection mirror, has a semi-cone acceptance angle of 12° which was used for the calculations in Fig. II.A.6-5a. It can be seen that $F^t_v$ is a smooth function of wavenumber, even though k changes substantially across the spectrum. For swelling coals, $F^t_v$ must be measured at each temperature because it varies with particle size. Indeed, the shape of the $F^t_v$ spectrum has been made the basis for the method of particle size determination (Solomon, et al., 1987a). The shape of $F^t_v$ can, however, be determined from measurement with the use of the above equation. For particles above 40 $\mu$m diameter, $F^t_v$ at 6500 $cm^{-1}$ is relatively insensitive to size, being equal to 1.1 ± 0.10. The temperature measurement can therefore be made on swelling coals as well. The sensitivity of the spectral shape of $F^t_v$ to particle size distribution makes the measured $F^t_v$ spectral useful monitors of the size distribution. Particle break-up, or swelling can be easily detected.

## Variations of Emittance with Coal Reactivity and Particle Size

Recent measurements (Solomon, et al., 1987a; 1987b) show that pulverized coal particles of the size used in entrained gasification are on-gray with emissivities which depend on size and rank. Also coal undergoes a transition from highly non-gray moderately pyrolyzed coal to highly gray char. Here we present measurements on non-pyrolyzing, warm coal particles of different rank and particle sizes.

The coal particles were entrained in He through the HTR for a distance of 90 cm at a nominal tube temperature of 350°C. A radial temperature profile of the gas stream taken with a 0.005" thermocouple where it passes through the FT-IR beam focus is shown in Fig. II.A.6-6. The average of this profile across the distance of the stream diameter is 568 K.

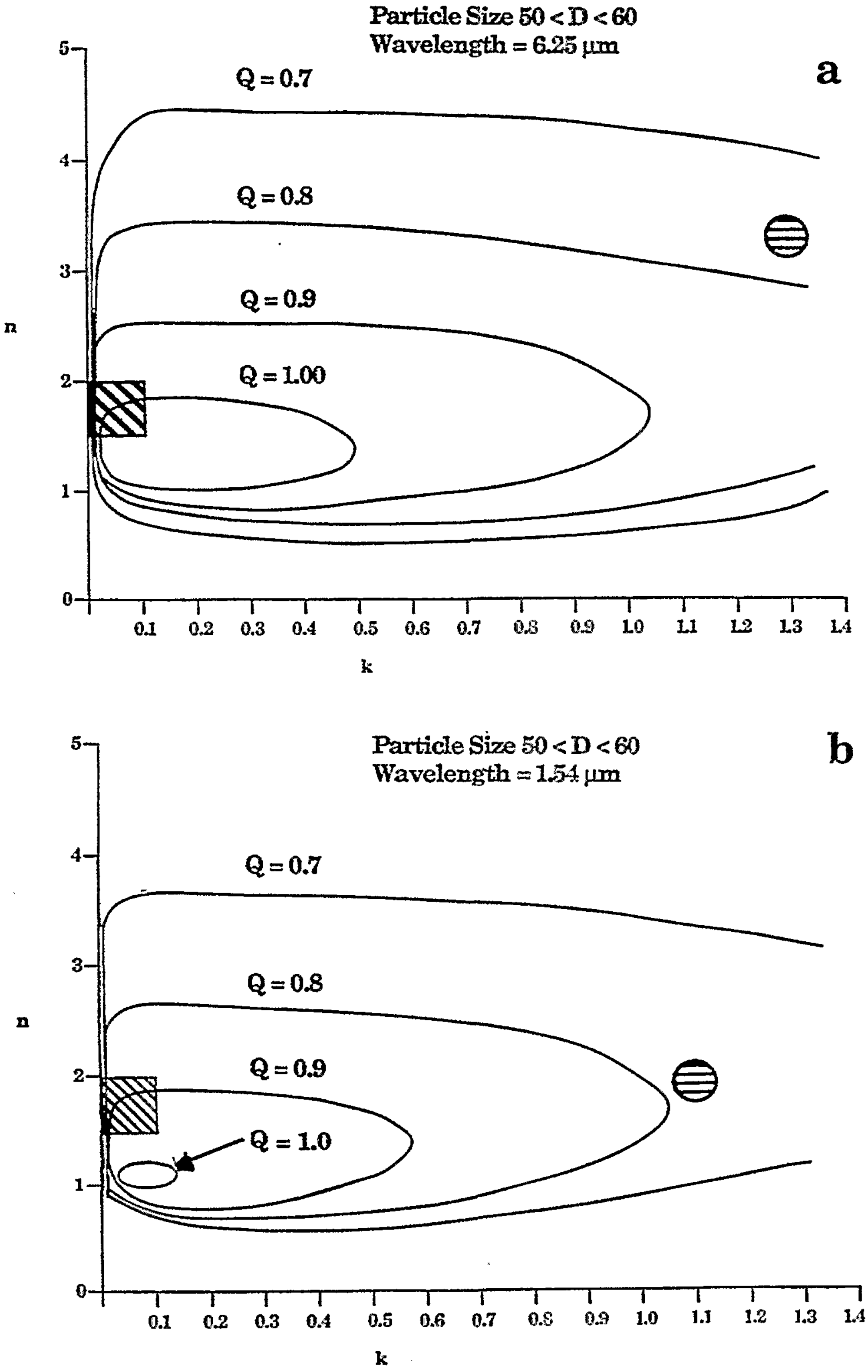

**Figure II.A.6-4.** Contour Plots of Constant Emittance, Q, Calculated by Mie Theory for Spheres of Various Values of n and k, for 55 µm Diameter Particles. The Combinations of n and k found for Coal in the Infrared are Shown Shaded on the Left Hand Side of the Diagram: Those for Graphite are Shaded on the Right (the values for graphite are taken from Foster and Howarth, 1968 ). The Calculations are for Radiation of two Wavelengths, as Shown.

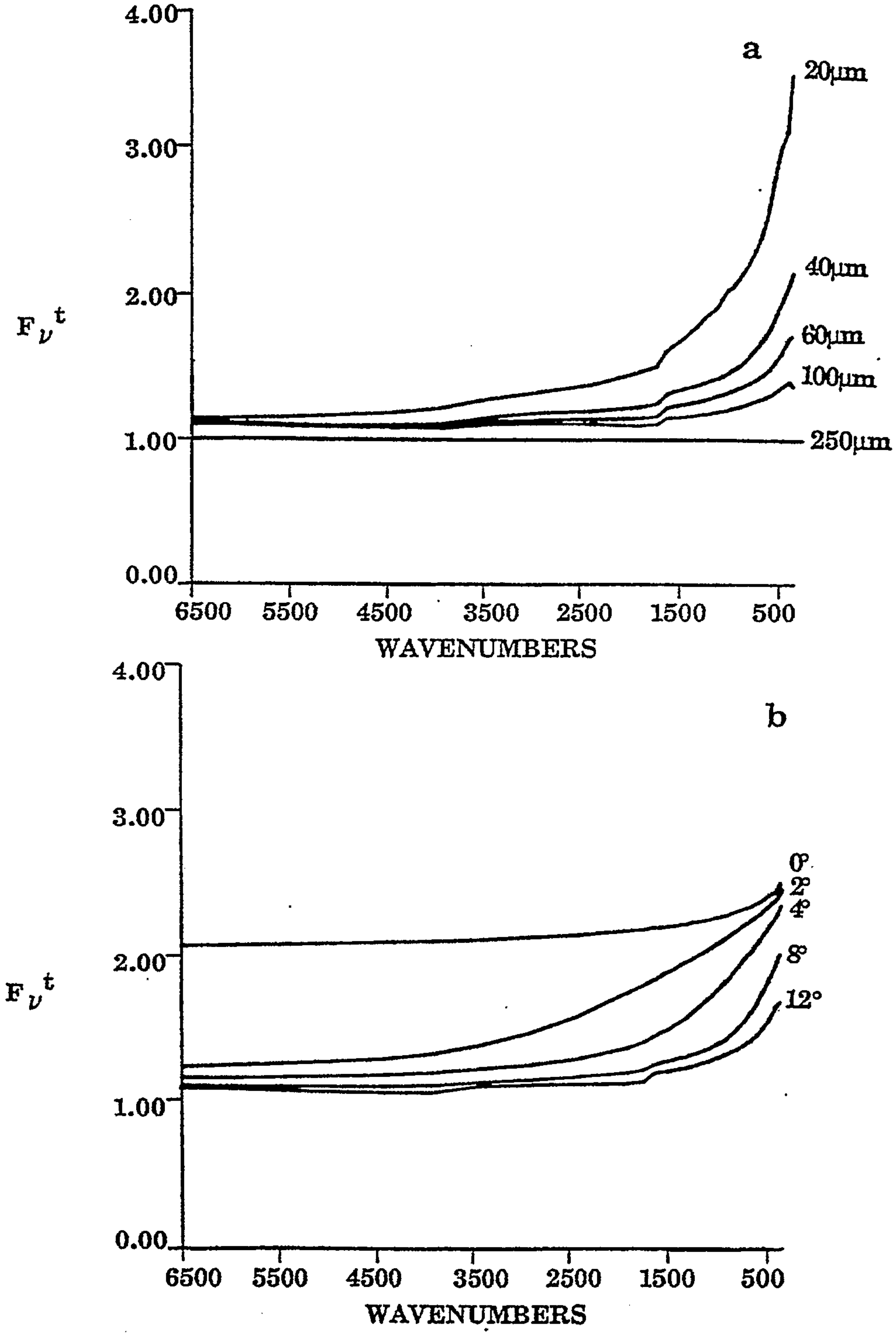

**Figure II.A.6-5.** a) Calculations of $F_\nu^t$ Spectra for our Instrument, for Particles of Various Diameters, and Having the Wavelength Dependent Optical Properties of a Montana Rosebud Subbituminous Coal (2). The Calculation for the 250 µm Diameter Particle was done with Raleigh Large Particle Theory. b) Calculations of $F_\nu^t$ Spectra for Instruments of Differing Half-Acceptance Angles, for Particles of Mean Diameter 60 µm.

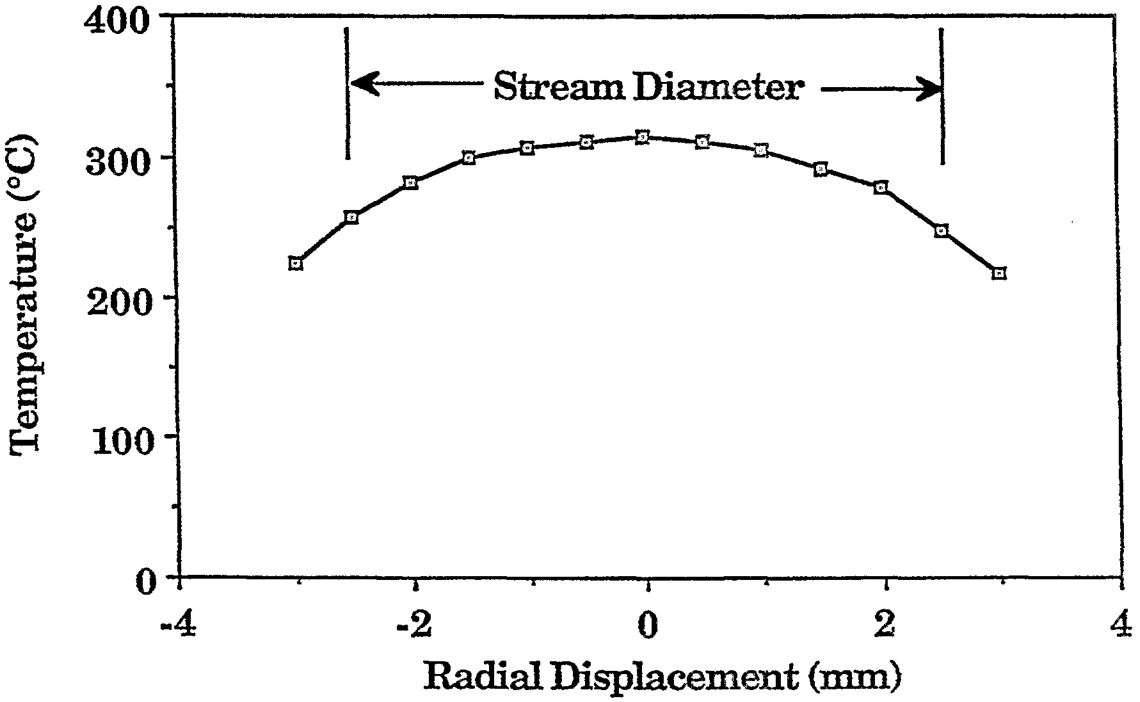

**Figure II.A.6-6.** Radial Thermocouple Temperature of Gas Stream Exiting the HTR at FT-IR Focus (.005" bead). Nominal HTR Temperature = 350°C. Radial Average = 295°C (568K).

To determine the spectral emittance for coal at a known temperature, measurements are made of the transmittance, $\tau_v$, and the radiance, $R_v$, from which the normalized radiance $R^n_v = R_v / (1-\tau_v)$ is calculated.

For the geometry of the HTR, the sample consists of hot or warm particles surrounded by cold walls. The spectral emittance is then given by (Best, et al., 1986)

$$\epsilon_v = F_v^t R_v^n / R_v^b (T_p) \qquad \text{(II.A.6-2)}$$

where $R^b_v(T_p)$ is the theoretical blackbody radiance at the particle temperature, $T_p$, and $F^t_v$ is the total extinction efficiency for the particles to scatter radiation our of the angular acceptance aperture of our instrument plus absorption. If $T_p$ and $F^t_v$ are known, then $\epsilon_v$ can be determined. Conversely, if $\epsilon_v$ and $F^t_v$ are known, $T_p$ can be determined.

Prior to each coal particle experiment presented here, a gas temperature determination was performed on a trace amount of $CO_2$ added to the particle stream to track fluctuations in the HTR nominal temperatures. The accuracy of this measurement is illustrated in Fig. II.A.6-7 which presents $R_v$, $1 - \tau_v$, and the normalized radiance for a mixture of carbon dioxide, butane, and acetylene passed through the HTR. For this non-scattering, gaseous sample, excellent agreement is observed between the thermocouple average temperature (568 K) and FT-IR line-of-sight determined average temperature 565 K). Figure II.A.6-8 indicates the sensitivity of this method to small shifts in temperature.

The coal samples used in this study (Table II.A.6-1) were obtained from the AFR/BYU sample bank (bulk samples) or from the Pittsburgh Energy Technology Center (PETC) of the Department of Energy. All samples having more then 3% moisture were dried before measurements were taken.

The transmittance spectra used to calculate the normalized radiance for the samples used in this study are presented in Figs. II.A.6-9 to II.A.6-12. The spectra are presented as $1 - \tau_v$ so that increased amplitude is proportional to increased attenuation.

The characteristics of large particles are that they scatter or absorb essentially all of the light incident on them. Any radiation hitting the particle which is not absorbed will be scattered. Consequently, the attenuation is proportional to the area of the particle and no absorption effects can be seen.

Figure II.A.6-9 to II.A.6-12 illustrate the effect of particle size on the shape of $1 - \tau_v$. As the particle size distribution is decreased, there is an increase in attenuation (sloping of the spectra) from short (6500 $cm^{-1}$) to long (500 $cm^{-1}$) wavelengths of incident radiation. This particle dependent change in the scattering (diffraction) component of $F^t_v$ indicates that the longer wavelengths of light have a higher efficiency of scattering out of the angular acceptance aperture of our instrument than the shorter wavelengths of light. As the particles get smaller, the higher efficiency to scatter extends further towards the short wavelength end of the spectrum.

Below a particle size of 20 $\mu$m, a drop in attenuation is observed at the long wavelength end of the spectrum. This effect is caused by the particles being smaller than the wavelength of incident radiation (1000 to 500 $cm^{-1}$ = 10 to 20 $\mu$m) and will allow this radiation to pass through without any scattering or absorption effects.

To see trends in emissivity with varying particle size and composition, $(1 - \tau_v)$ 6500 $cm^{-1}$ was used for the percent attenuation in the following analysis. Figures II.A.6-13 to II.A.6-15 are the normalized radiance, $R^n_v(T) = R_v / (1- \tau_v)$ 6500 $cm^{-1}$, for three coals with different size distributions. Overlayed on the experimental data is the theoretical blackbody curve $R^b_v(T)$, corresponding to the temperature determined from the $CO_2$ tracer test, multiplied by a constant ($\epsilon_v / F^t_{6500}$) to give the best

## Table II.A.6-1.
### SAMPLE DATA FOR OPTICAL PROPERTIES MEASUREMENTS

| Coal Name | Rank | Particle Size Distribution ( $\mu$m) | %C (DAF) | %Ash (Dry Basis) | %Moisture | Source |
|---|---|---|---|---|---|---|
| Pocahontas #3 | LVB | 75-45 | 91 | 4.83 | 0.61 | AFR/BYU |
| Upper Freeport | MVB | 75-45 | 87 | 11.63 | 0.83 | AFR/BYU |
| Pittsburgh #8 | HVAB | 75-45 | 83 | 9.02 | 1.80 | AFR/BYU |
| Upper Kanawha | MVB | 75-45 | 81 | 26.44 | 2.60 | AFR/BYU |
| Utah Blind Canyon | HVCB | 75-45 | 79 | 4.68 | 4.71 | AFR/BYU |
| Illinois #6 | HCVB | 75-45 | 77 | 23.42 | 2.94 | AFR/BYU |
| Smith Roland | SUBC | 250-210 | 72.97 | 9.23 | 24.51 | PETC |
| Smith Roland | SUBC | 106-75 | 73.26 | 12.27 | 20.97 | PETC |
| Smith Roland | SUBC | 63-45 | 72.38 | 18.29 | 13.26 | PETC |
| Smith Roland | SUBC | 30-20 | 73.67 | 12.87 | 9.96 | PETC |
| Smith Roland | SUBC | 20-10 | 73.24 | 14.03 | 9.10 | PETC |
| Smith Roland | SUBC | -10 | 73.17 | 15.64 | 8.23 | PETC |
| Lower Kittaning | LVB | 106-75 | 88.65 | 19.31 | 0.62 | PETC |
| Lower Kittaning | LVB | 36-45 | 87.73 | 17.43 | 0.64 | PETC |
| Lower Kittaning | LVB | 30-20 | 90.53 | 9.17 | 0.83 | PETC |
| Lower Kittaning | LVB | 20-10 | 90.55 | 8.03 | 0.91 | PETC |
| Lower Kittaning | LVB | -10 | 89.82 | 7.68 | 0.93 | PETC |
| Beulah N.D. | Lignite | 250-210 | 69.48 | 8.86 | 28.49 | PETC |
| Beulah N.D. | Lignite | 106-750 | 69.82 | 15.23 | 22.63 | PETC |
| Beulah N.D. | Lignite | 63-45 | 71.25 | 32.81 | 13.41 | PETC |

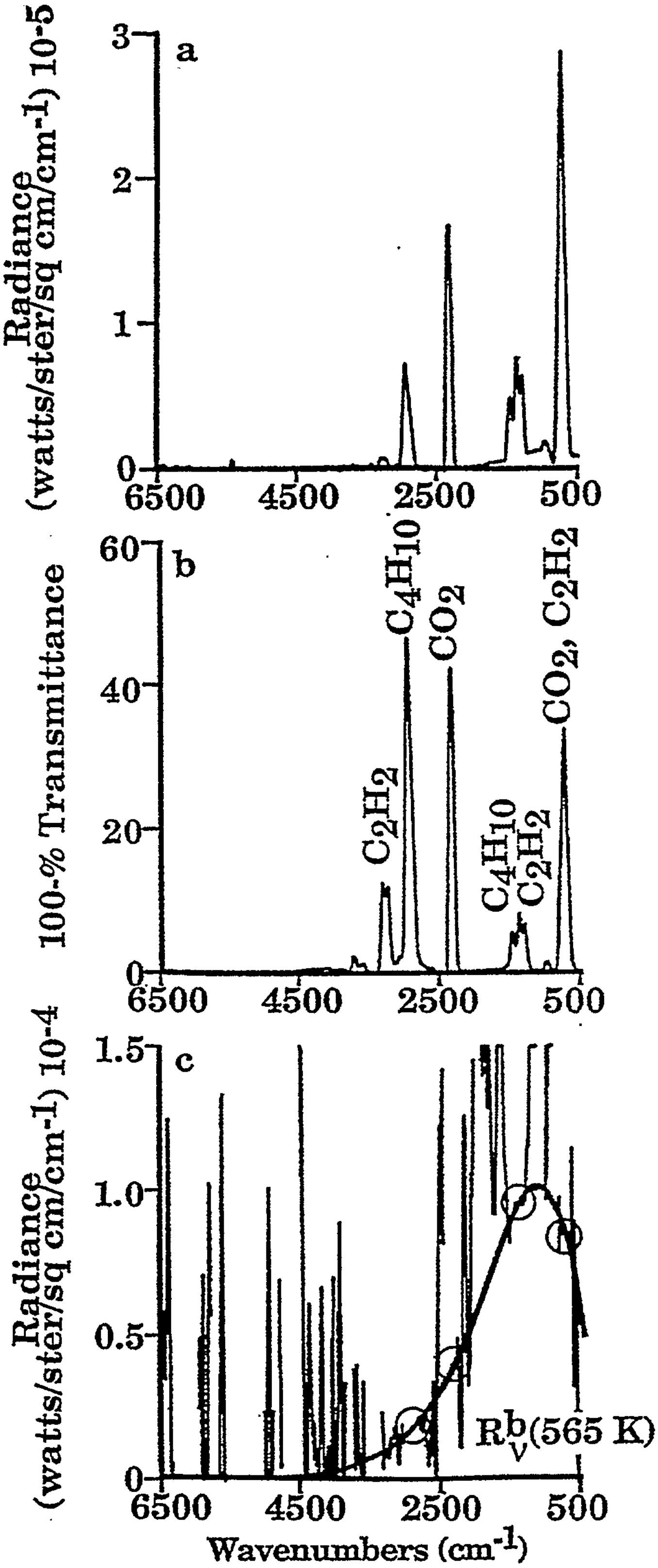

**Figure II.A.6-7.** FT-IR E/T Spectra for a Mixture of $CO_2$, $C_4H_{10}$, and $C_2H_2$ Exiting the HTR. a) Raw Radiance ($R_\nu$), b) 100%-Transmittance ($1-\tau_\nu$), and c) Normalized Radiance, $R_\nu^n = R_\nu/(1-\tau_\nu)$. $R_\nu^b$ (565K) Represents Theoretical Black Body Distribution Best Fit to Regions of Absorption/Emission for the Mixture (circled regions).

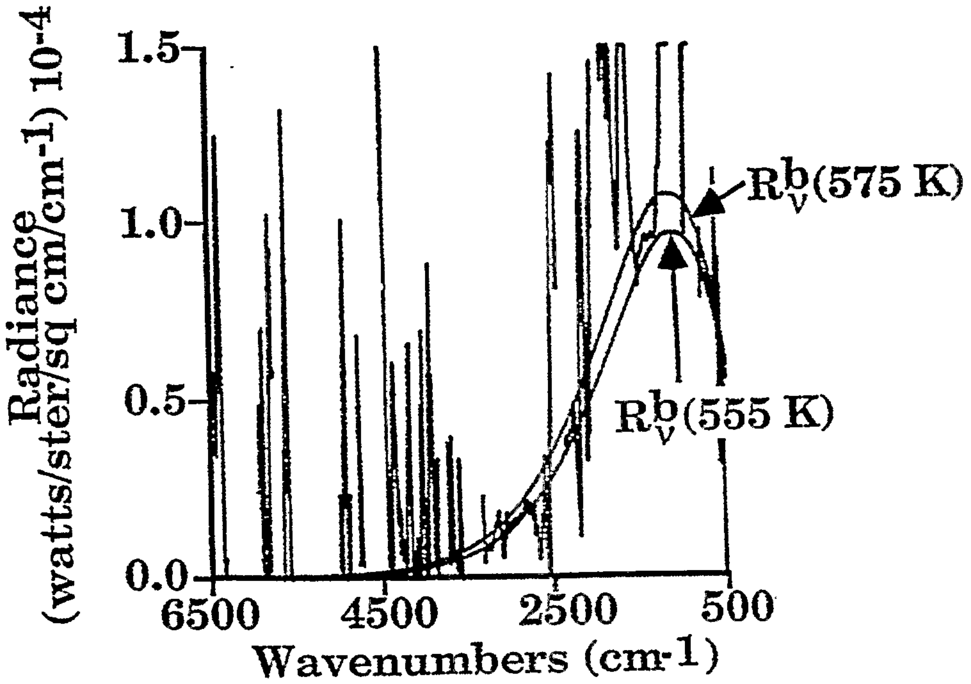

Figure II.A.6-8. Normalized Radiance Spectrum with ±10K Shift from the Best Fit $R^b_\nu(T)$.

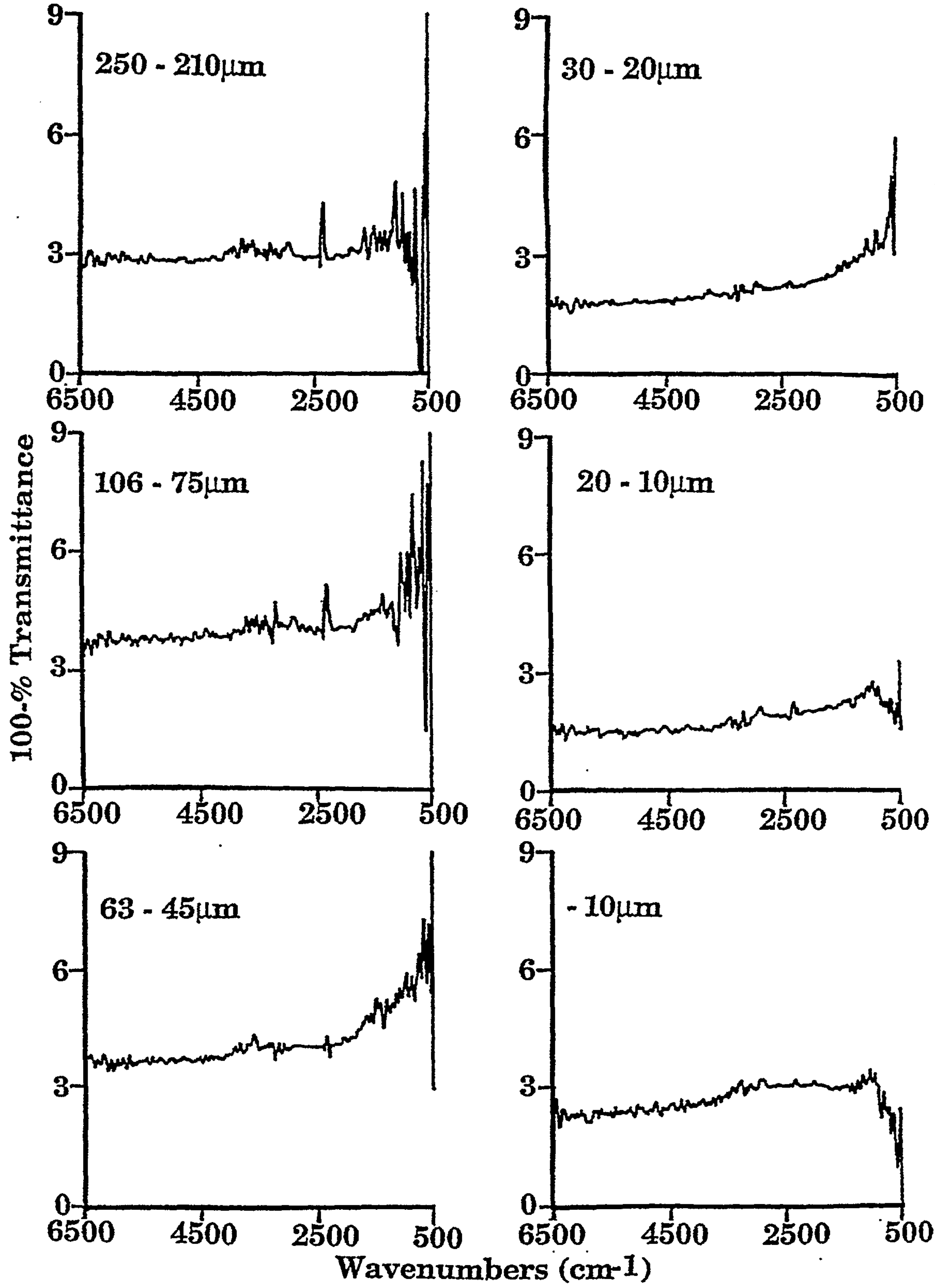

Figure II.A.6-9. 100-% Transmittance Spectra for Different Particle Size Distributions of Smith Roland Subbituminous Coal.

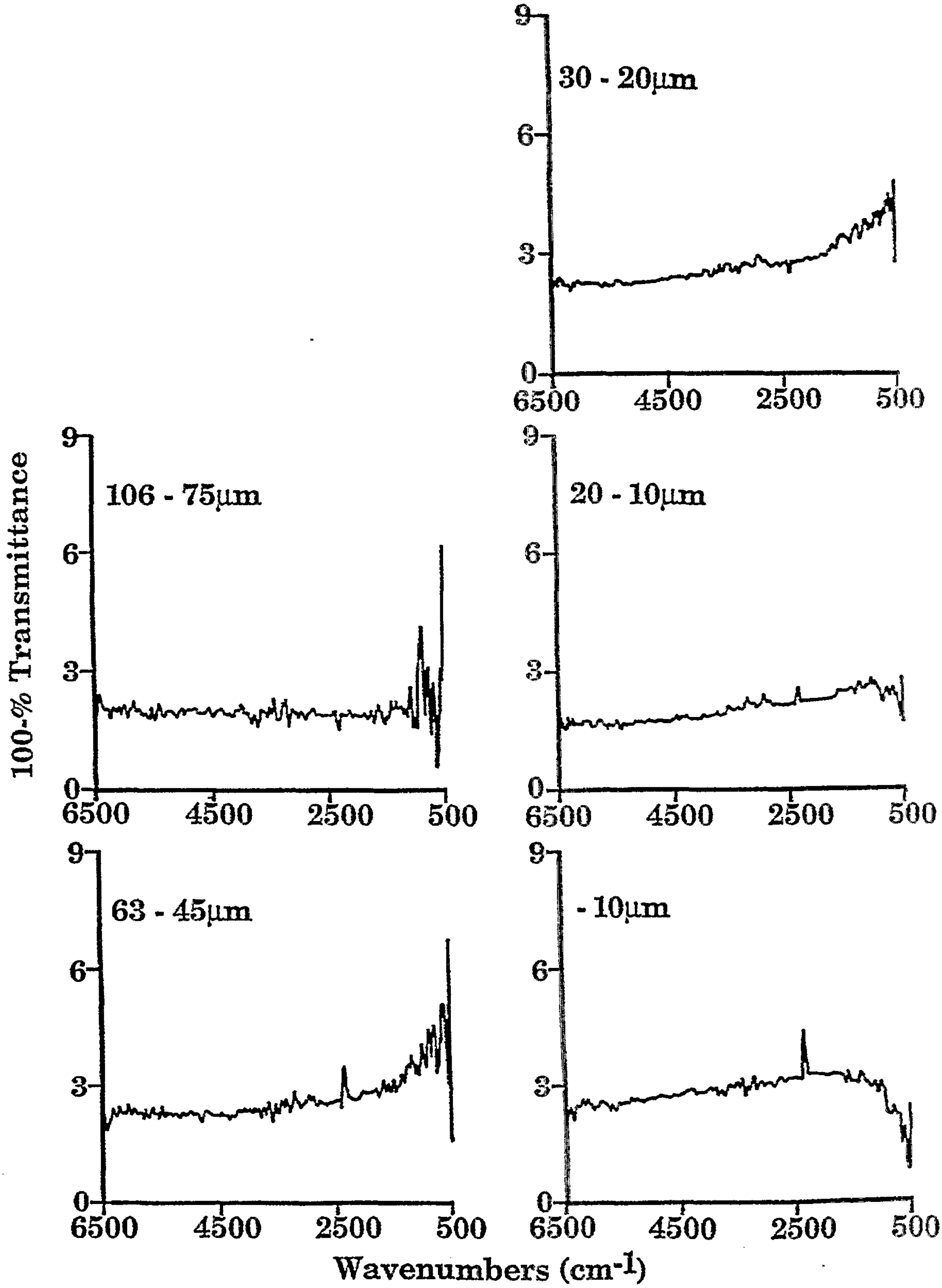

**Figure II.A.6-10.** 100-% Transmittance Spectra for Different Particle Size Distributions of Lower Kittaning Bituminous Coal.

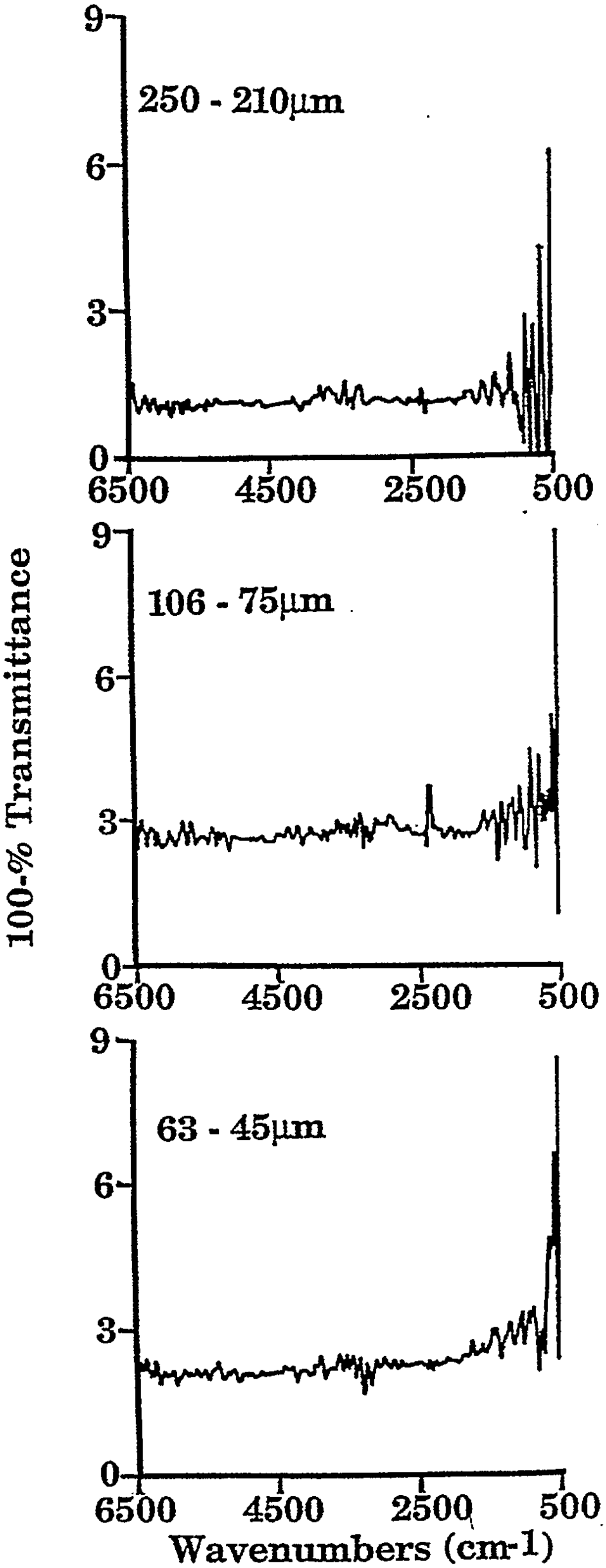

**Figure II.A.6-11.** 100-% Transmittance Spectra for Different Particle Size Distributions of Beulah North Dakota Lignite.

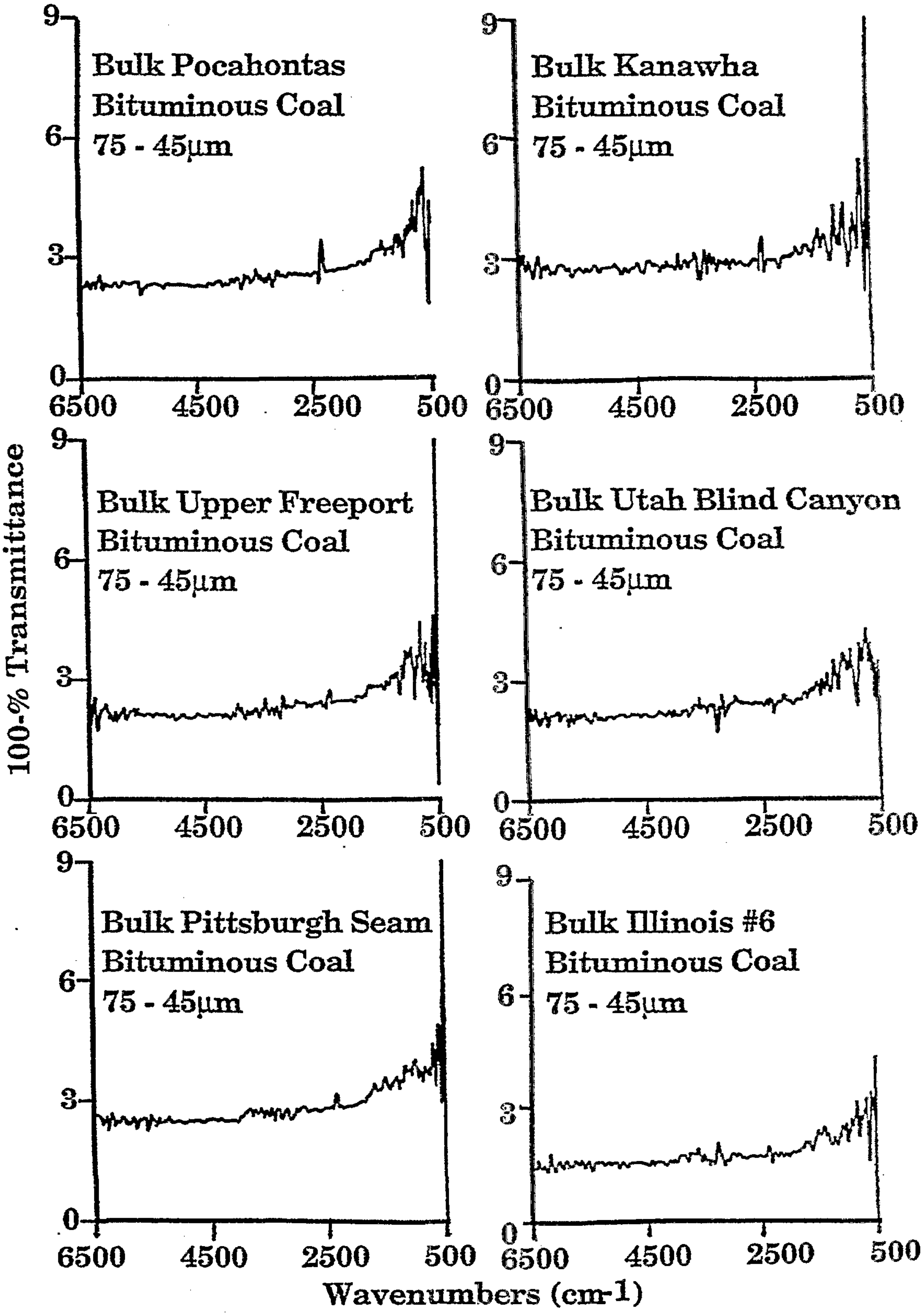

Figure II.A.6-12.100-% Transmittance Spectra for Bituminous Coals from the AFR/BYU Sample Bank (bank bulk samples).

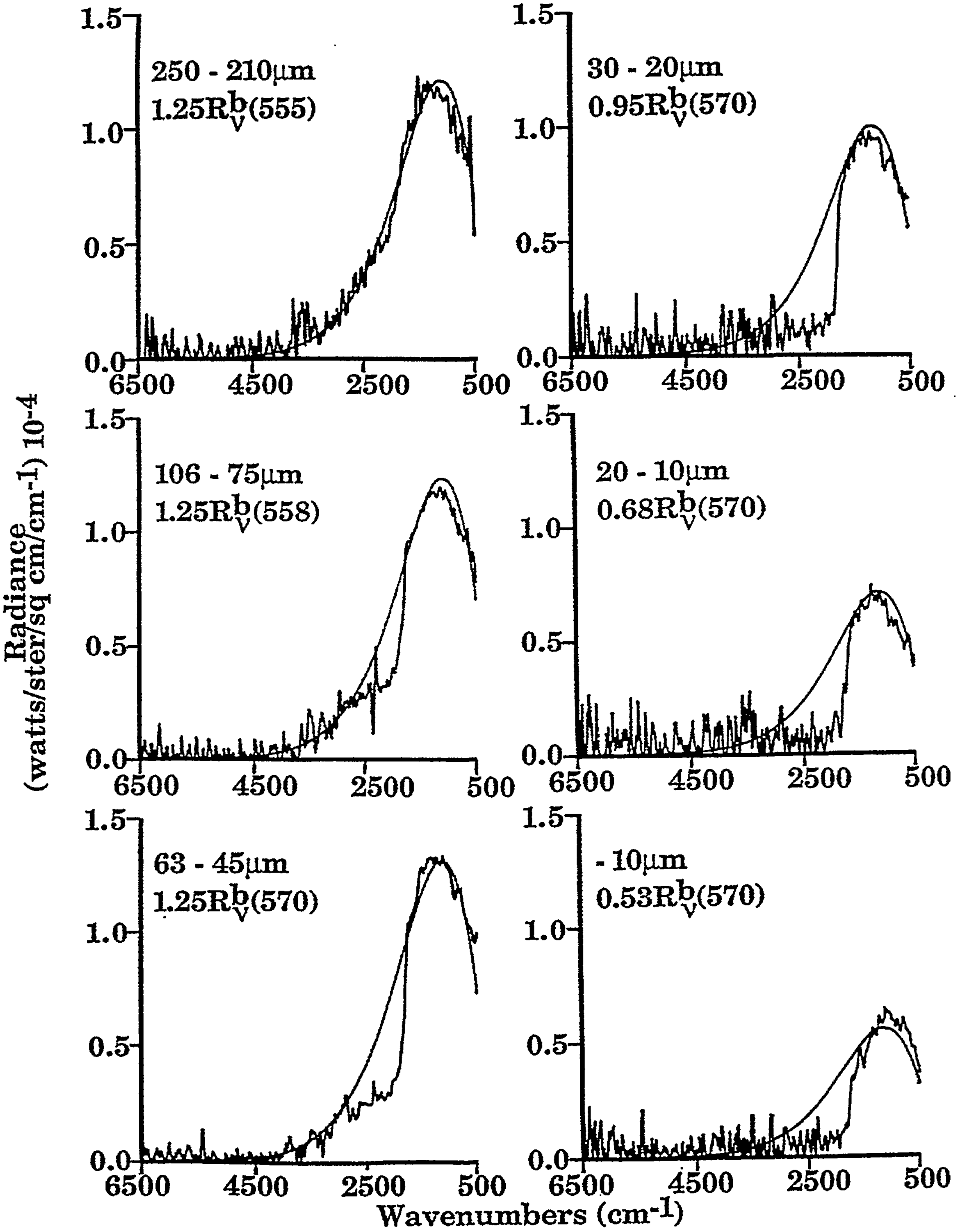

Figure II.A.6-13. Normalized Radiance Spectra for Different Particle Size Distributions of Smith Roland Subbituminous Coal. $R^b_\nu(T)$ is in Degrees Kelvin.

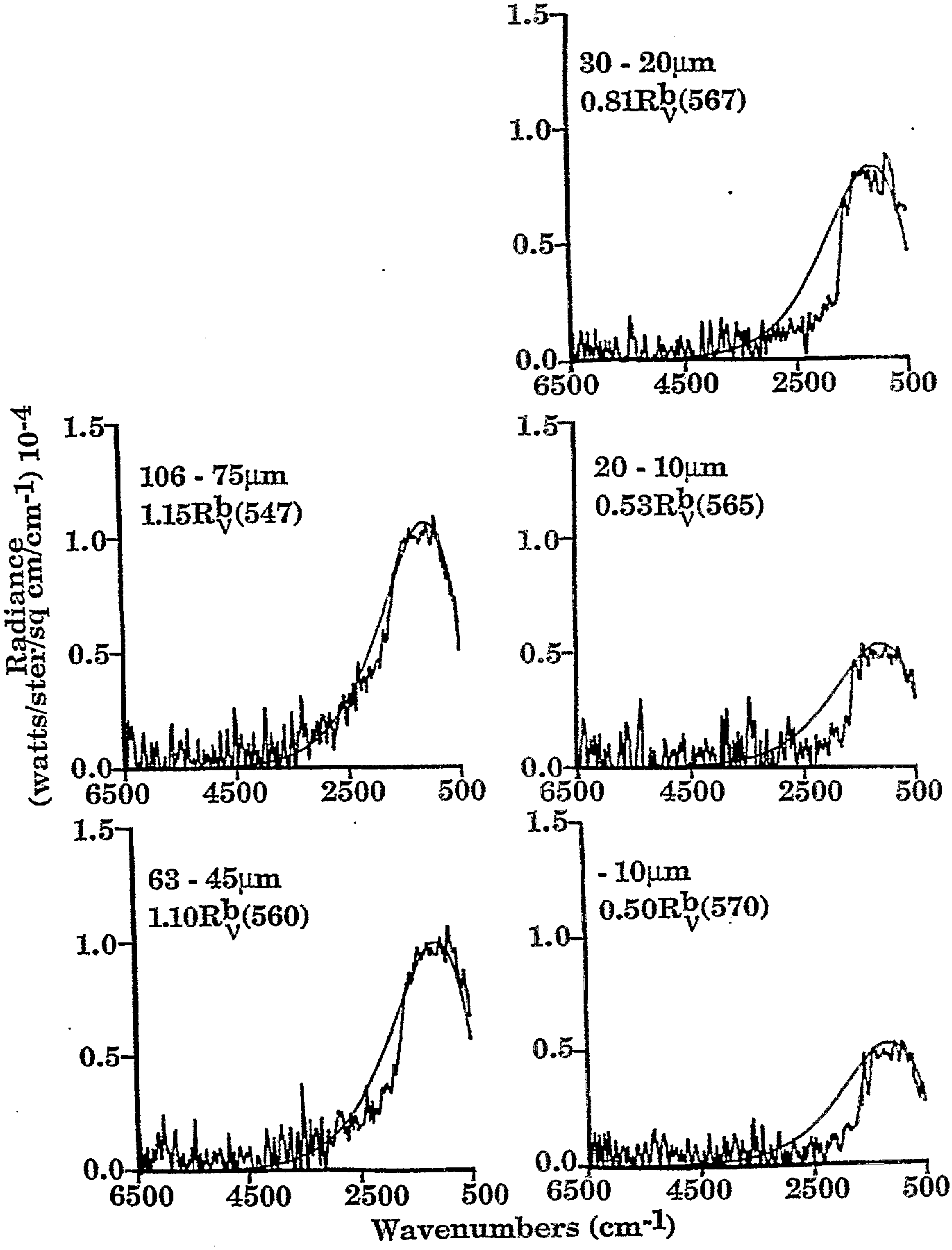

**Figure II.A.6-14.** Normalized Radiance Spectra for Different Particle Size Distributions of Lower Kittaning Bituminous Coal.

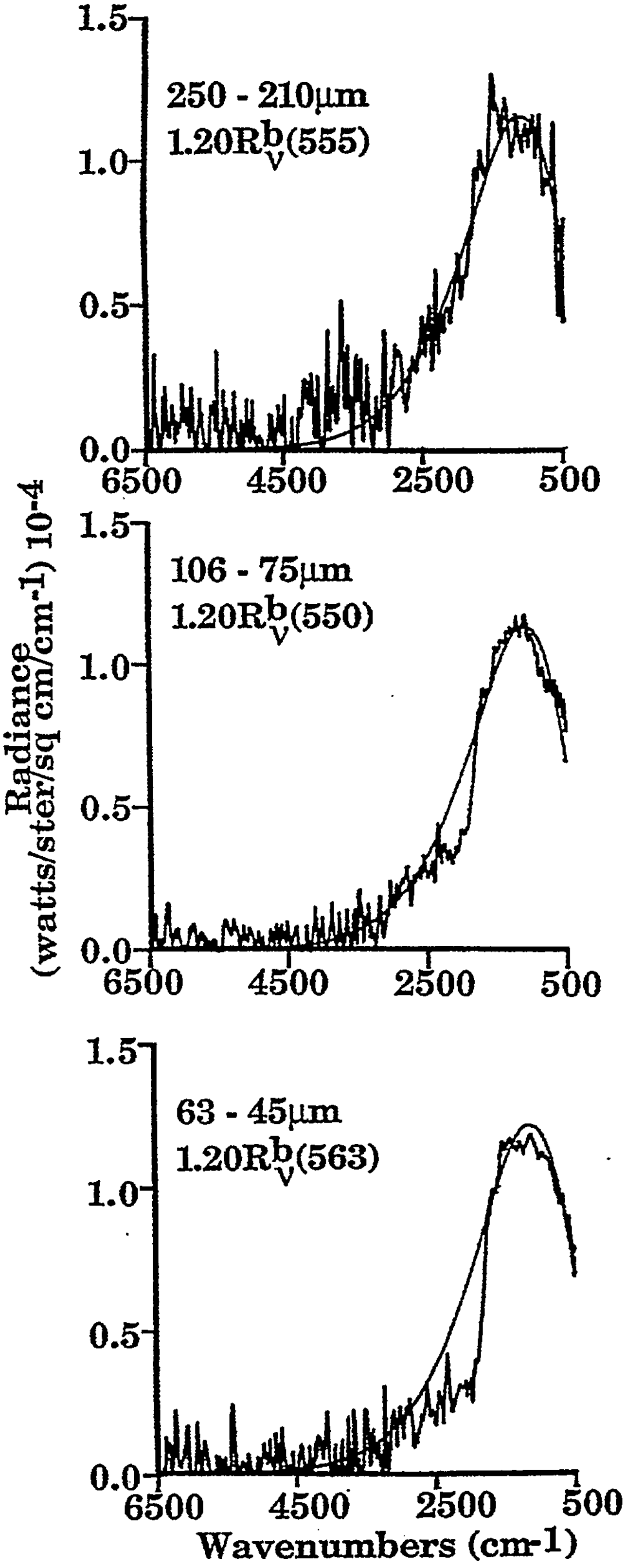

**Figure II.A.6-15.** Normalized Radiance Spectra for Different Particle Size Distributions of Beulah North Dakota Lignite.

fit to the coal spectrum in the strong absorption region ($\nu < 1700$ cm$^{-1}$) for coal.

The trend with particle size is consistent for all three coals. The largest particle size (250 to 210 $\mu$m) shows agreement close to the overall blackbody over all of the spectrum. The smaller particles sizes continue this agreement for $\nu < 1700$ cm$^{-1}$, but the emittance decreases for $\nu > 1700$ cm$^{-1}$. The smaller the particle size, the larger is the decrease. The trend with rank is that the lower rank Beulah lignite and Smith Roland subbituminous coals show a slightly larger decrease above 1700 cm$^{-1}$ than does the higher rank Lower Kittaning bituminous coal.

Figure II.A.6-16 compares six bituminous coals from the bulk AFR/BYU samples obtained for this program. For these similar size fractions (75 to 45 $\mu$m), again there is agreement with the overlayed blackbody curve below 1700 cm$^{-1}$. The decrease above 1700 cm$^{-1}$ does appear to become slightly more drastic with decreasing carbon content of the coals.

The spectral emissivity ($\epsilon_\nu$) for coal particles larger than 10 $\mu$m at wavelengths which coincide with strong infrared absorption bands should be approximately equal to 1. Therefore, $F^t_{6500}$ is changing with particle size and rank as indicated by the different multiplier values used to fit $R^b_\nu(T)$ to the observed normalized radiance spectra. An attempt was made to determine the surface area of the particle stream by using a light source with an incident radiation that is well out of the diffraction and absorption regime for coal particles ($F^t_\nu = 1$). A He-Ne laser, 0.633 $\mu$m radiation, ~ 16,000 cm$^{-1}$ was directed through the coal stream to a photo-sensitive resistor. The output of this visible light detector was checked for linearity by partially blocking the laser beam with several different area sized light choppers. The source was also modulated (chopped) when directed through the coal to avoid room light interferences. The coal should be opaque to the laser radiation.

A plot of percent FT-IR beam attenuation at 6500 cm$^{-1}$, vs percent He-Ne laser beam attenuation is presented in Fig. II.A.6-17 for the size fractions of Smith Roland subbituminous coal. For the three large size fractions, where $\epsilon_\nu / F^t_{6500} > 1$ in Fig. II.A.6-13, the laser indicates that a larger value of $(1 - \tau)$ 6500 cm$^{-1}$ should be used (i.e., the FT-IR is indicating a low amount of beam attenuation due to scattering of incident radiation back into the collection angle of our instrument, $F^t_{6500} < 1$). For the three smaller size fractions, where $\epsilon_\nu / F^t_{6500} < 1$ in Fig. II.A.6-13, the laser indicates that a smaller value of $(1-\tau)$ 6500 cm$^{-1}$ should be used (i.e., the FT-IR is indicating a high amount of beam attenuation due to a high efficiency of scattering incident radiation out of the collection angle of our instrument, $F^t_{6500} > 1$).

Although the He-Ne laser measurements begin to converge the spectral emittance for $\nu < 1700$ cm$^{-1}$ towards 1 for the different particle sizes, it was observed that the moving particles contributed their own modulated signal to the visible light detector. This contribution, along with laser power and detector drift, did not allow this laser beam attenuation technique to be as accurate as desired in determining the surface area of the particle stream. Work is in progress on an accurate optical geometry for this determination.

Trends in the spectral emittance ($R^n_\nu / R^b_\nu$) as a function of particle size and rank re plotted in Fig. II.A.6-18. The value at 2500 cm$^{-1}$ was calculated since it is out of the functional group emission region ($\nu < 1700$ cm$^{-1}$) but still within the broad band emission region for coal particles at 300°C. The trends with rank and particle size are clearly shown. Figure II.A.6-19 compares the spectral emittance for one particle size distribution for nine different coals. The emittance remains fairly constant (~ 0.55) until above 85% carbon (DAF), at which point an increase in emittance is observed.

## Conclusions

Although we can determine the trends in the spectral emissivity ($\epsilon_\nu$) for coal with varying particle size and rank, accurate values of $F^t_\nu$ (the total extinction efficiency for scattering out of the angular acceptance aperture of our instrument plus absorption) must be determined for particles and experimental geometry used before accurate $\epsilon_\nu$ can be determined. By choosing a light source (He-Ne laser) that

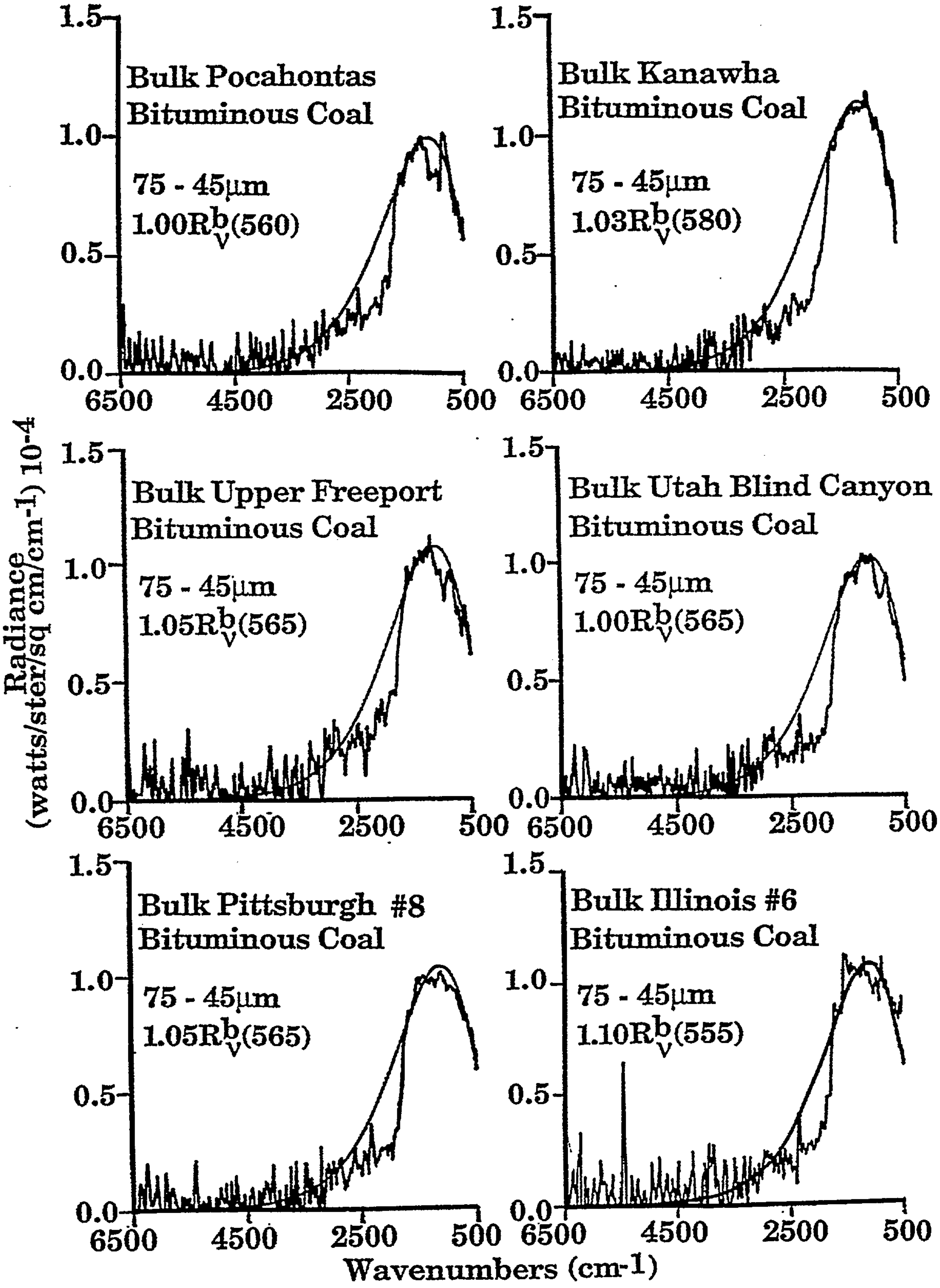

Figure II.A.6-16. Normalized Radiance Spectra for Bituminous Coals from the AFR/BYU Sample Babk (bulk samples). $R_V^b$(T) is in Degrees Kelvin.

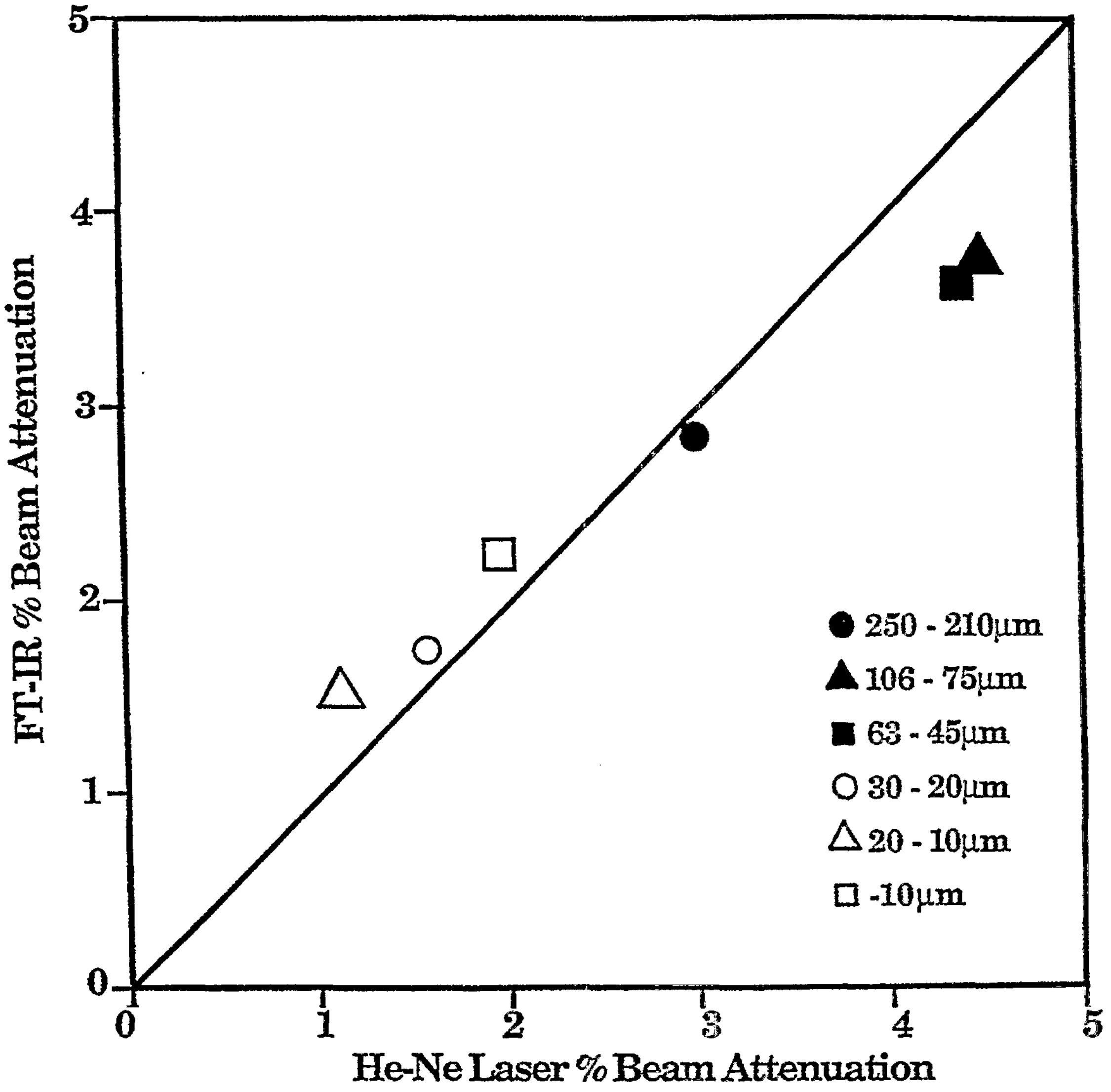

**Figure II.A.6-17.** FT-IR % Beam Attenuation at 6500 cm$^{-1}$ vs. He-Ne Laser % Beam Attenuation for Different Particle Size Distributions of Smith Roland Subbituminous Coal.

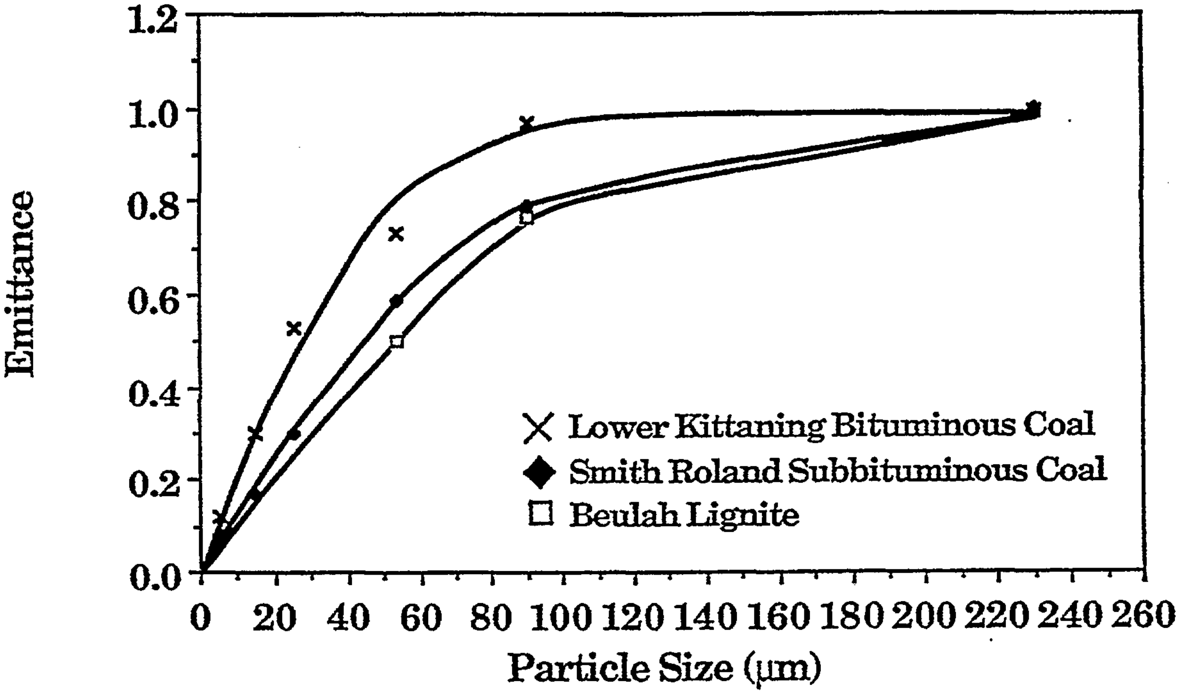

Figure II.A.6-18. Spectral Emittance $(R_\nu^n / R_\nu^b)$ Calculated at 2500 $cm^{-1}$ vs. Average Particle Size for Three Different Coal Samples.

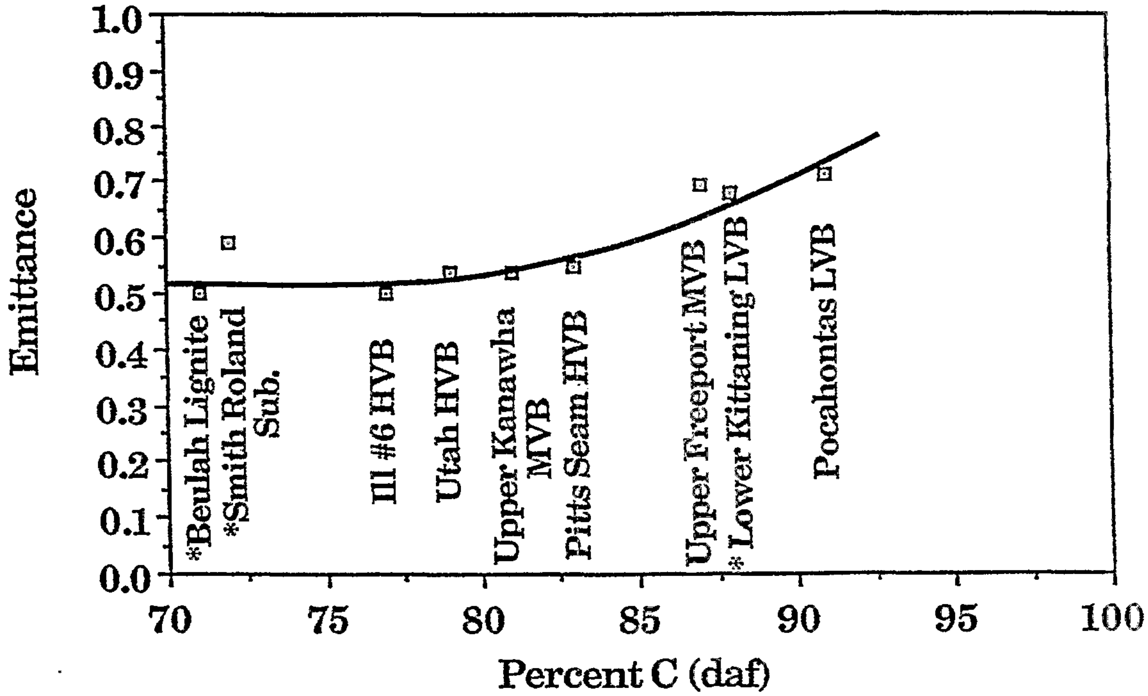

**Figure II.A.6-19.** Spectral Emittance ($R_\nu^n/R_\nu^b$) Calculated at 2500 cm$^{-1}$ vs. Percent Carbon (daf) for Nine Coal Samples of Similar Particle Size Distribution (45-75 μm or *45-63μm).

should be well out of the diffraction and absorption regime for the samples used here, the $\epsilon_v$ values in regions of strong infrared absorption bands for various particle sizes of the same material begin to converge. The laser attenuation values, however, are not as accurate as necessary for these determinations due to: 1) laser power drift, 2) detector response drift, and 3) signal contribution from extraneous modulation of the laser beam due to the traversing coal particles.

## Optical Properties Model

An outline of the proposed optical properties submodel is shown in Fig. II.A.6-20. In the case of the optical properties submodel, it is not clear yet how much impact this model will have on the predictions of PCGC-2. Consequently, a sensitivity analysis is now underway. The optical properties for different size particles of Zap lignite were calculated and sent to BYU for input into PCGC-2. The results from the study of BYU suggest that there is no need for a detailed submodel in PCGC-2 for coal optical properties.

## II.A.7. Polymethylenes

There is present in coals varying amounts (typically 0-9%, but in some cases as high as 18%) of long-chain aliphatics (polymethylenes). These have recently been reported in pyrolysis products by Nelson (1987) and by Calkins and coworkers (1984a,b,c,d) and references quoted therein. The chains appear alone and attached to aromatic nuclei. During devolatilization, the smaller molecules may be released without bond breaking and the heavier molecules with bond breaking to contribute to the tar. The presence of these polymethylenes makes the tar more aliphatic than the parent coal. Further cracking of this material under more severe devolatilization conditions produces ethylene, propylene, and butadiene from which the concentration of polymethylenes may be determined (Calkins, 1984d). Originally, the polymethylenes were included in the FG model as part of the aliphatic functional group pool, which is assumed to decompose to produce gas products, not tar. This led to an error in determining the H/C ratio in the tar which can be important for low rank coals (Freihaut, et al., 1988).

A literature review was done on the occurrence of polymethylenes in coals in order to help formulate a strategy to address the problem. This was included in Appendix B in the Eleventh Quarterly Report. This information can be summarized as follows:

1. Polymethylenes, $(CH_2)_n$, are present in coals at a level of 0 - 18 wt.% depending on rank.
2. Very high rank coals (anthracites) contain very little $(CH_2)_n$ while low rank coals (lignites) generally contain at least 10 wt.%. The amounts for coals of intermediate rank are highly variable and depend on geochemical factors.
3. Exinite macerals are high in polymethylenes, followed by vintrinite and then inertinite.
4. A significant fraction of the $(CH_2)_n$ are attached to aromatic structures in the coal and are not readily extractable.
5. The $(CH_2)_n$ are the precursors for the ethylene, propylene, and butadiene produced from high temperature pyrolysis of coal. They are not precursors for methane, benzene or other light aromatic compounds.
6. The $(CH_2)_n$ appear to play an important role in donating hydrogen to stabilize the reactive aromatic fragments.
7. The $(CH_2)_n$ appear to decompose by a free radical chain reaction which is different than that observed for pure $(CH_2)_n$ in the gas phase. They also decompose differently than the main coal structure.

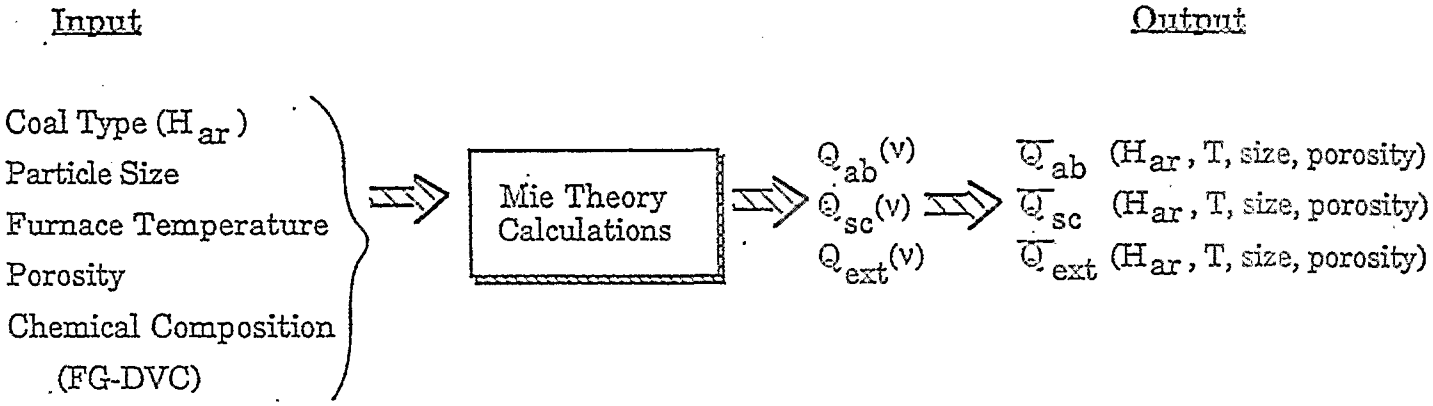

**Figure II.A.6-20.** Outline of Submodel for Optical Properties of Coals and Chars.

8. Some of the $(CH_2)_n$ are light enough to vaporize directly without bond breaking. The low temperature tars which evolve prior to the main decomposition peak and the low temperature extracts from coal are enriched in $(CH_2)_n$.

9. The vaporization laws which apply to $(CH_2)_n$ will be different than those which apply to the aromatic tars. For a given molecular weight, aliphatic compounds are more volatile than aromatic compounds.

10. The $(CH_2)_n$ will not participate in crosslinking reactions in the same way as the rest of the (aromatic) tar molecules.

All of these factors must be addressed to correctly deal with the occurrence of polymethylenes. However, some can be neglected in the first generation model.

If the amount of heavy polymethylenes is determined, these can be computed as a separate functional group pool with an appropriate release rate and added to the tar. However, strictly speaking, a certain fraction of the polymethylenes should also be included as a type of oligomer so that the smaller species can vaporize directly, without bondbreaking. This would also allow the polymethylenes to be included in the extractable species. The problem of vaporizing the small polymethylenes and including them in the extract yield are related. For most coals, there is a low temperature tar peak which is polymethylene-rich but also includes aromatic tars. Currently, the FG-DVC model uses an interactive procedure at the beginning of a simulation which adjusts the oligomer length to match the experimental pyridine extract yield with the molecular configuration in the computer. The model considers extract to be those molecules which are less than 3000 in molecular weight. However, this does not produce tar molecules which are light enough to vaporize at low temperatures.

The presence of these polymethylenes makes the tar more aliphatic than the parent coal. Also, for most coals, there is a low temperature tar peak which results from the vaporization of unattached small polymethylenes plus small aromatic ring clusters. This vaporization peak is illustrated in Fig. II.A.7-1. Polymethylene chains can also crack or be released into the second tar peak. Further cracking of this material under more severe devolatilization conditions produces ethylene, propylene, and butadiene from which the concentration of polymethylenes may be determined (Calkins et al., 1984d). Originally, the polymethylenes were included in the FG model as part of the aliphatic functional group pool, which is assumed to decompose to produce gas products, not tar. This leads to predicted H/C ratios in the tar for low rank coals which are lower than those measured by Freihaut et al. (1988).

Polymethylenes have now been added to the DVC part of the model as a second class of material whose molecular weight distribution and functional group composition are different from the main macromolecular network. The starting coal molecule now includes a distribution of oligomer sizes for polymethylenes and other guest molecules (with the chemical composition of the network). The vaporization of these molecules produces a peak which matches the early vaporization peak as shown in Fig. II.A.7-1. We also account for polymethylenes which are attached to the coal matrix and removed by bond breaking by including them as species in the FG model. Those polymethylenes are then added to the tar after vaporization.

The model requires a value for the total polymethylene content in the coal. Calkins determined that the yields of ethylene, butadiene, and propylene correlated well with the polymethylene content (1984d). It was decided that this is the most general and fruitful approach to take and we have used the coals which are in our set and Calkins' set to calibrate the method. As a first approximation, we arbitrarily chose to use polymethylene = 0.7 $(C_2H_4)$. This gave $-CH_2-$ contents slightly above Calkin's values, but within 15% of Calkin's. The model also assumes that 50% of the polymethylenes are small enough to vaporize and are included in the oligomer pool while the other 50% are not and are included in the FG pool.